Strongly-correlated Lattice Systems on a Finite Cylinder



Paolo Rosson

St Cross College

University of Oxford

A thesis submitted for the degree of

Doctor of Philosophy in Atomic and Laser Physics

Trinity Term 2019

Strongly-correlated Lattice Systems on a Finite Cylinder

Paolo Rosson

St Cross College
University of Oxford

A thesis submitted for the degree of
Doctor of Philosophy in Atomic and Laser Physics

Trinity Term 2019

Abstract

In this thesis, I present my research on the numerical simulation of finite-size strongly-correlated lattice systems using the density matrix renormalisation group (DMRG). Ultracold gases in optical lattices have become the experimental setup of choice to simulate models from condensed-matter physics, because of their high degree of tunability and control. Their inherently finite size and alternative implementation call for a more in-detail study of how to define and characterise the phases of the models that they simulate.

I use DMRG to implement lattice Hamiltonians of highly-correlated systems with long-range interactions and identify their ground states on a finite system geometry. I describe in detail the process of constructing long-range Hamiltonians for their use in DMRG. I then apply these numerical methods to two fundamental models. I study the ground state of a fractional quantum Hall system and identify it as the well-known Laughlin state in a still unexplored parameter regime, by calculating its topological entanglement entropy and by using a set of physical observables that are available in a finite cylindrical geometry. I then study a dipolar Bose-Hubbard model and perform a systematic study of the order parameters that can best be used to characterise its phases in an ultracold gas setting by comparing how different types of observables are sensitive to finite-size and boundary effects.

My results are meant to provide guidance for future experimental realisations of bosonic lattice models of small sizes.

Acknowledgements

I am extremely grateful to my supervisor, Dieter Jaksch, for his guidance during my D.Phil.

I want to thank all of the people in my group, especially Martin Kiffner, Michael Lubasch and Jordi Mur-Petit for helping me through my research projects.

Contents

1 Introduction **1**

1.1 Quantum Hall physics . . . 7
1.1.1 Introduction . . . 7
1.1.2 Classical Hall effect . . . 7
1.1.3 Quantum Hall effect . . . 10
1.1.3.1 Landau level physics . . . 12
1.1.4 Integer quantum Hall effect . . . 16
1.1.5 Fractional quantum Hall effect . . . 20
1.1.6 Topological order and topological entanglement entropy . . . 24
1.1.7 Bosonic quantum Hall states . . . 26
1.2 Quantum simulation with ultracold atoms . . . 27
1.2.1 Bose-Hubbard model . . . 28
1.2.1.1 Extended Bose-Hubbard model . . . 31
1.2.2 Dipolar Bose-Hubbard model . . . 34
1.2.3 Lattice quantum Hall systems . . . 36
1.2.3.1 Lattice fractional quantum Hall states . . . 39
1.3 Numerical methods . . . 40
1.3.1 Introduction . . . 41
1.3.2 Matrix product states . . . 41
1.3.3 MPS and entanglement . . . 46
1.3.4 Matrix product operators . . . 48
1.3.5 Pictorial representation . . . 49
1.3.6 Density matrix renormalisation group . . . 52

2 Development of 2D long-range interacting Hamiltonians for DMRG 56

2.1 2D density matrix renormalisation group . . . 57
2.1.1 Tensor network methods . . . 58
2.2 MPO construction . . . 59
2.2.1 Finite-state automata method . . . 61
2.2.1.1 Example: Heisenberg model . . . 62
2.3 Interacting Harper-Hofstadter model . . . 63
2.3.1 2D-to-1D mapping . . . 65
2.3.2 Periodicity of the MPO matrices . . . 66
2.3.3 Effect of the gauge field . . . 66
2.3.4 Effect of the 2D-to-1D mapping and boundary conditions . . . 68

2.3.4.1 Bottom terms . . . 70
2.3.4.2 Middle terms . . . 72
2.3.4.3 Top terms . . . 73
2.3.5 Additional consequences of the gauge field . . . 74
2.3.6 Explicit form of the MPO matrices . . . 75
2.3.7 Bosonic and fermionic models . . . 76
2.3.7.1 Bosonic case . . . 76
2.3.7.2 Fermionic case . . . 77
2.3.8 Extensions to long-range terms and other lattice geometries . . . 79
2.4 Dipolar Bose-Hubbard model . . . 80
2.4.1 Translational invariance . . . 82
2.4.1.1 Central term: $2 < y < L_y - 2$ . . . 82
2.4.1.2 Top term: $y = L_y$ . . . 84
2.4.1.3 Top term: $y = L_y - 1$ . . . 85
2.4.1.4 Bottom term: $y = 2$ . . . 85
2.4.1.5 Bottom term: $y = 1$ . . . 86
2.4.2 Dipolar interaction coefficients . . . 86
2.5 Testing, benchmarking and applications . . . 87

3 Bosonic fractional quantum Hall ground states on a finite cylinder 89
3.1 Bosonic Harper-Hofstadter model . . . 90
3.2 Topological entanglement entropy . . . 92
3.3 Quantum Hall signatures . . . 94
3.3.1 Particle density . . . 95
3.3.2 Edge currents . . . 97
3.3.3 Correlation functions . . . 99
3.4 Interaction-strength dependence . . . 101
3.4.1 Edge currents . . . 101
3.4.2 Correlation functions . . . 104
3.4.3 Additional quantities . . . 104
3.4.4 $\phi = 1/4$ . . . 106
3.5 Conclusion and outlook . . . 108

4 Dipolar Bose-Hubbard ground states on a finite lattice 111
4.1 Dipolar Bose-Hubbard model . . . 113
4.2 Half filling . . . 115
4.2.1 Solid order . . . 115
4.2.2 Superfluidity and off-diagonal long-range order . . . 119
4.2.3 Entanglement entropy . . . 123
4.2.4 Lattice size and boundary conditions . . . 125
4.2.4.1 Checkerboard solid with open boundary conditions . . . 126
4.3 Supersolidity triggered by one-particle doping . . . 128
4.4 Star solid . . . 134
4.5 Machine learning approach . . . 137
4.5.1 Principal component analysis . . . 138

4.5.2 Simulated measurement results of density configurations . . . 139
4.5.3 PCA of the Schmidt values 144
4.6 Conclusion and outlook 146

5 Conclusion and outlook **150**

Bibliography **153**

Chapter 1

Introduction

Characterising the phases of many-particle quantum systems is perhaps one of the most exciting and challenging aims of condensed-matter physics. The presence of interactions and strong correlations are believed to be the source of new exciting phenomena and phases, from fractional quantum Hall states [1] to high-temperature superconductors [2]. A complete understanding of strongly-correlated systems is significantly sought after not only for theoretical purposes but also for the potential technological applications, from high-temperature superconductivity [3] to quantum computation [4].

This thesis contributes to classical simulation techniques as well as guiding quantum simulation experiments. Regarding classical simulation, we expand density matrix renormalisation group (DMRG) [5] methods to study two-dimensional (2D) strongly-correlated quantum lattice systems. We also suggest relevant parameter regimes to consider in quantum simulation experiments with ultracold gases in optical lattices.

To achieve this, we focus on two compelling quantum lattice systems which prove to be computationally challenging to study and which provide exciting theoretical insights and future technological applications. First, we consider the fractional quan-

tum Hall physics of ultracold bosonic atoms in a 2D optical lattice. We ask whether fractional quantum Hall ground states can be realised on finite-size cylindrical lattices with a fixed number of particles, in the presence of a large magnetic flux through the lattice. Second, we consider a system of polar molecules in a 2D lattice interacting through a long-range static dipole-dipole interaction. We look for a set of order parameters that can be measured in current ultracold gas experiments to characterise the phase diagram of the system.

Let us start by motivating our development of the numerical methods. The interplay between a set of quantum objects brings about complex behaviours that cannot be strictly understood from the study of the single constituents of the system by themselves. Analytical methods are typically only tractable when the particles comprising the systems are free or weakly correlated. In this case, theoretical insight can be used to parametrise the ground state of the system with few parameters. These approaches break down when the interactions play a significant role, and different length and energy scales need to be simultaneously taken into account. The number of parameters necessary to exactly describe the full many-body state of the system typically grows exponentially with the number of particles. This causes the description of macroscopic properties of the system to be extremely challenging to obtain. Successful numerical techniques used to study many-particle systems still present limitations, such as exact diagonalisation [6] being limited to small system sizes, or quantum Monte Carlo [7, 8] being afflicted by the sign problem. It is therefore of great relevance to have access to a numerical method that can efficiently treat strongly-correlated many-particle systems, while being able to avoid these limitations.

The DMRG algorithm addresses explicitly this problem [5]. It uses matrix product states (MPS), which efficiently parametrise the relevant subset of the Hilbert space where the ground states live [9, 10], as a variational optimisation ansatz to find the ground state of a system [11]. It is of pivotal importance to be able to implement

the Hamiltonians of strongly-correlated systems having long-range interactions for 2D DMRG numerical simulations. This is what we set out to do in the first part of the thesis. In Chapter 2, we review the concept of a finite-state automaton to build the matrix product operator representing the Hamiltonian of the system. In particular, we describe how to implement the interacting bosonic Harper-Hofstadter Hamiltonian, characterised by the presence of complex hopping factors representing the artificial gauge field necessary to simulate quantum Hall physics. Additionally, we implement long-range interactions typical of a dipolar Bose-Hubbard model.

Let us now consider the common context surrounding the quantum simulation of the two physical systems we study. Ultracold gases in optical lattices are nowadays considered as one of the most tunable and controllable setups to explore many-body physics [12, 13, 14]. Such setups allow for the simulation of physical models originating from solid-state systems, are amenable to exploring their emergent behaviour, and give access to parameter regimes otherwise unattainable [15, 16, 17]. These systems can successfully implement the Bose-Hubbard model [18], which is the prototypical model exhibiting a quantum phase transition and which can be tuned to reach the strongly-correlated regime. The quantum simulation of the systems we consider is implemented using ultracold gases in optical lattices.

We now focus on the first physical system that we study: the ground states of a fractional quantum Hall model. Traditionally, phase transitions are underpinned by Landau's theory, based on the idea that spontaneous breaking of different symmetries allows different phases to be distinguished [19]. The discovery of the integer and fractional quantum Hall effects [20, 21] profoundly challenged this paradigm, by introducing phases that could no longer be identified through the measurement of a local order parameter [22], but are instead characterised by long-range entanglement features [23] and topological invariants such as the Chern number [24]. Most interestingly, fractional quantum Hall states present several unusual properties, such as ground-state

degeneracy that depends on the genus of the manifold the system is embedded in and which cannot be lifted by local perturbations [25], and quasiparticle excitations carrying fractional charge [26] and having fractional statistics, called anyons. Moreover, fractional quantum Hall states present an avenue for ground-breaking technological advancement, from quantum memories [27] to topological quantum computers [23], implemented through a subset of fractional quantum Hall states supporting non-Abelian anyons [4].

The ultracold gas toolbox can be used to simulate quantum Hall physics. The Alkali atoms used in optical lattice setups are neutral and are not affected by the Lorentz force of a charged particle in a magnetic field. Artificial gauge fields have been proposed to overcome this limitation [28, 29, 30, 31, 32] and have been experimentally realised in optical lattices [33]. The progress in this area resulted in the experimental implementation of the Harper-Hofstadter Hamiltonian [34, 35, 36, 37] and the measurement of topological quantities such as the Chern number of Hofstadter bands [24, 38]. The addition to the Hofstadter model of on-site interactions, which is fundamental for the implementation of quantum Hall physics, has also been realised in optical lattices [39]. All of the ingredients necessary to simulate quantum Hall physics in an optical lattice are therefore available for its realisation with ultracold atoms. The high level of control of such experiments also makes them as a potential setting for technological developments. Bosonic quantum Hall states that support non-Abelian anyons can be a means to realise topological quantum computation [4, 40].

It is of fundamental importance to predict the behaviour of quantum Hall systems on a lattice, to study the type of phases they support and compare them with those available in the continuum, where quantum Hall physics originates. Studies of small lattice systems [41, 42, 43, 44], allowing for exact diagonalisation, have shown the existence of fractional quantum Hall ground states and analysed them by comparing

their overlap with the Laughlin wavefunction [26]. They concluded that in the large magnetic flux regime, available to experiments, the overlap is small.

In Chapter 3, we use DMRG to calculate fractional quantum Hall ground states on a finite cylindrical lattice. We compute the topological entanglement entropy of the state as a sign of topological order. Additionally, we take advantage of the finite geometry, giving access to both bulk and edge properties of the state, to calculate a set of physical quantities showing that, in the large magnetic flux regime available in optical lattice experiments, the ground state of the system is compatible with the Laughlin ground state.

Let us now consider the context surrounding the second system of interest of this thesis, dipolar molecules in a 2D lattice. Quantum simulation of Bose-Hubbard models is implemented with Alkali atoms, for which the atom-atom interaction is short-ranged. The characteristic length of interatomic potentials is typically of the order of 10-100 Bohr radii, and hence much smaller than the optical-lattice spacing (100-1000 nm). However, new experimental setups have been developed and are currently subject to investigation, where the interactions between particles are long-ranged, such as atomic ions in Penning traps [45, 46] and systems with dipole-dipole interactions like Rydberg atoms [47, 48, 49], highly-magnetic atoms [50, 51, 52, 53, 54], or ultracold molecules [55, 56, 57]. For such systems, the interactions typically decay with the cube of the distance, and it is no longer sufficient to consider only on-site interactions. This leads to the open question of which new phases these long-range interacting systems can realise. Many theoretical and numerical calculations have approached this problem and have suggested the existence of exotic phases such as supersolid [58], spin-glass [59] and spin-ice [60] phases. We focus our study on lattice systems made from dipolar molecules. Ref. [58] studied the phase diagram of the dipolar Bose-Hubbard model using Quantum Monte Carlo methods in the grand-canonical ensemble and showed how this system supports novel phases. Solid

phases appear at fractional fillings, such as the checkerboard and star solid, and a supersolid phase, which is characterised by the simultaneous presence of solid order and superfluid order, appears when doping the system in the solid phase.

The motivation for our study of this system is determining whether such phases will occur in small lattices with a fixed number of particles, similarly to their experimental realisation. In Chapter 4, we obtain the phase diagram of a dipolar Bose-Hubbard model on a finite square lattice in the canonical ensemble. We consider several observables available in optical lattice setups and assess how well they perform as order parameters. We find that, in small systems, the appearance of a supersolid phase is very sensitive to boundary effects, potentially making its observation challenging. Additionally, we show how density measurements obtainable using quantum gas microscopes enable us to distinguish between solid and superfluid phases using unsupervised machine learning methods.

The remainder of this chapter introduces the main concepts used throughout this thesis and is structured as follows. Section 1.1 describes the main features of quantum Hall physics, from the classical Hall effect to the integer and fractional quantum Hall effects. Section 1.2 describes the Bose-Hubbard model and its extensions used in quantum simulation with ultracold gases in optical lattices. Finally, Section 1.3 covers the fundamentals of the numerical methods used throughout the thesis: matrix product states and the density matrix renormalisation group.

The results presented in this thesis in Chapter 3 have been published in Ref. [61] and the results in Chapter 4 have been published in Ref. [62].

1.1 Quantum Hall physics

1.1.1 Introduction

The quantum Hall effect is the collective class of phenomena that occur when electrons are constrained to move in two dimensions (2D) in the presence of a strong orthogonal magnetic field. Under these conditions, the system shows unusual properties. The most prominent is the Hall conductivity σ_{xy} taking on quantised values. The Hall conductivity is the off-diagonal component of the conductivity tensor σ that describes the current density $\boldsymbol{J}$ induced by an electric field $\boldsymbol{E}$: $\boldsymbol{J} = \sigma \boldsymbol{E}$. Fig. 1.1 shows a schematic representation of the system in a 2D geometry.

The Hall conductivity takes on the quantised values: $\sigma_{xy} \propto \nu$, where ν is the filling fraction, defined as the number of Landau levels filled by the electrons in the system. The filling fraction ν is related to the magnetic field B as: $B \propto \frac{n}{\nu}$, where n is the density of electrons.

Classically, the Hall conductivity is expected to show a linear relation with the inverse of the magnetic field. However, it is observed to take on quantised values. When ν is an integer, this phenomenon is called the integer quantum Hall effect, and when it is a rational number, it is called the fractional quantum Hall effect.

1.1.2 Classical Hall effect

The classical Hall effect, discovered by Edwin Hall in 1879 [63], is a consequence of the dynamics of charged particles in a magnetic field. The experimental setup comprises a two-dimensional metallic strip in the presence of an orthogonal magnetic field. A depiction of the setup is shown in Fig. 1.1. When a potential difference V is imposed on the system in the x direction, inducing the flow of a current I_x, a voltage V_H is observed in the y direction, orthogonal to both the magnetic field and the potential V. This voltage is proportional to the magnitude of the magnetic field.

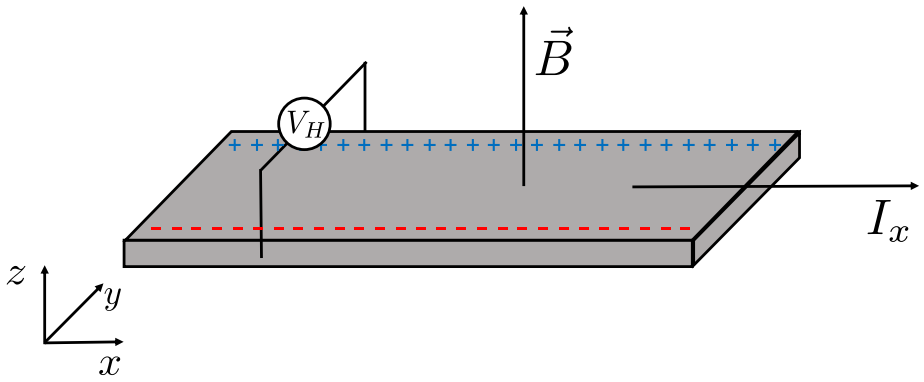


Figure 1.1: Schematic representation of the experimental setup used to observe the classical Hall effect.

This phenomenon is a consequence of the Lorentz force for a charged particle in a magnetic field

$$\boldsymbol{F} = q(\boldsymbol{E} + \boldsymbol{v} \times \boldsymbol{B}) \,, \tag{1.1}$$

where q is the charge of the particle, $\boldsymbol{E}$ is the electric field, $\boldsymbol{B}$ is the magnetic field and $\boldsymbol{v}$ is the velocity of the particle. In free space, the orthogonal magnetic field causes the particles to move along circular orbits, called cyclotron orbits, with angular frequency $\omega_B = \frac{qB}{m_p}$, where m_p is the mass of the particle. The Lorentz force causes the electrons moving through the sample to drift and accumulate at the edges. This displacement of charges induces the orthogonal potential difference V_H and a corresponding electric field that compensates for the Lorentz force.

The value of the Hall voltage V_H and conductivity σ_{xy} is classically calculated using the Drude model [64], the simplest model of charge transport that treats the electrons as if they were colliding elastically. The motion of the electrons is described by

$$m_p \frac{d\boldsymbol{v}}{dt} = q\boldsymbol{E} + q\boldsymbol{v} \times \boldsymbol{B} - \frac{m_p \boldsymbol{v}}{\tau} \,, \tag{1.2}$$

where the last term of the equation represents a friction term and τ is the scattering

time.

Solving Eq. (1.2) for its equilibrium state leads to the relation between the electric field $\boldsymbol{E}$ and the current density $\boldsymbol{J} = nq\boldsymbol{v}$, where n is the 2D particle density. This relation takes the form $\boldsymbol{J} = \sigma\boldsymbol{E}$, where σ is the conductivity tensor defined as

$$\sigma = \begin{pmatrix} \sigma_{xx} & \sigma_{xy} \\ -\sigma_{xy} & \sigma_{yy} \end{pmatrix} = \frac{\sigma_0}{1+\omega_B^2\tau^2} \begin{pmatrix} 1 & -\omega_B\tau \\ \omega_B\tau & 1 \end{pmatrix}, \tag{1.3}$$

where $\sigma_0 = \frac{nq^2\tau}{m_p}$ is the conductivity in the absence magnetic field. The Hall conductivity σ_{xy} is the off-diagonal term of the conductivity tensor.

Let us consider the resistivity, which is the inverse of the conductivity. In this case

$$\rho = \sigma^{-1} = \frac{1}{\sigma_0} \begin{pmatrix} 1 & \omega_B\tau \\ -\omega_B\tau & 1 \end{pmatrix}. \tag{1.4}$$

The off-diagonal term $\rho_{xy} = \frac{m_p\omega_B}{nq^2}$ is the Hall resistivity and is no longer dependent on the scattering time τ. This indicates that the Hall resistivity is a fundamental property of the system which is independent of the noise causing the scattering.

The resistance R, which is the quantity usually measured, is related to the resistivity by a geometric factor that depends on the dimensionality of the system [65]. In 2D, resistance and resistivity coincide because their relation reads $R \propto L^{2-d}\rho$. In the 2D geometry we have considered, the transverse resistance reads $R_{xy} = V_H/I_x$ and the resistivity reads $\rho_{xy} = \frac{E_y}{J_x}$. These two quantities are the same since $V_H = L_y E_y$ and $I_x = L_y J_x$, where L_x and L_y are the lengths of the metallic strip in the x and y direction respectively. This means that the resistance of the system is invariant of its scale.

An additional important quantity to consider is the Hall coefficient, defined as

$$R_H = \frac{E_y}{J_x B} = \frac{\rho_{xy}}{B} = \frac{1}{nq}. \tag{1.5}$$

The Hall coefficient depends on the density n and on the charge q of the particles, and its measurement is used to determine whether the charge carriers are electrons or holes. Despite this model being crude, it is able to give reasonable estimates of the experimental results [64].

1.1.3 Quantum Hall effect

When the temperature of the system is low, and the magnetic field is strong, the classical description introduced in the previous section is no longer sufficient to explain the behaviour of the system. Two different phenomena arise, which are the integer and fractional quantum Hall effect. They were first discovered experimentally and only later understood theoretically.

The first observation of the integer quantum Hall effect was achieved in 1980 [20]. It was observed that both the diagonal and off-diagonal components of the resistivity tensor showed a peculiar behaviour, as presented in Fig. 1.2. The Hall resistivity ρ_{xy}, instead of growing linearly with B as predicted in the classical regime, showed plateaus and jumps at specific values of the magnetic field. In particular, it was found that

$$\rho_{xy} = \frac{2\pi\hbar}{e^2}\frac{1}{\nu}\,, \tag{1.6}$$

where e is the charge of the electron, $\hbar$ the reduced Planck's constant, ν an integer and $2\pi\hbar/e^2$ is the quantum of resistivity. A striking quality of this formula is that ν takes on integer values with extreme precision, of the order of 10^{-8}. Such a degree of accuracy has led this measurement to become the standard measure of resistivity and was even introduced as a way to calculate the fine structure constant α through $\alpha^{-1} = \frac{h}{e^2}\frac{2}{\mu_0 c}$ [20], where c is the speed of light and μ_0 is the permeability of free space.

The plateaus in the off-diagonal part of the resistivity appear when the magnetic

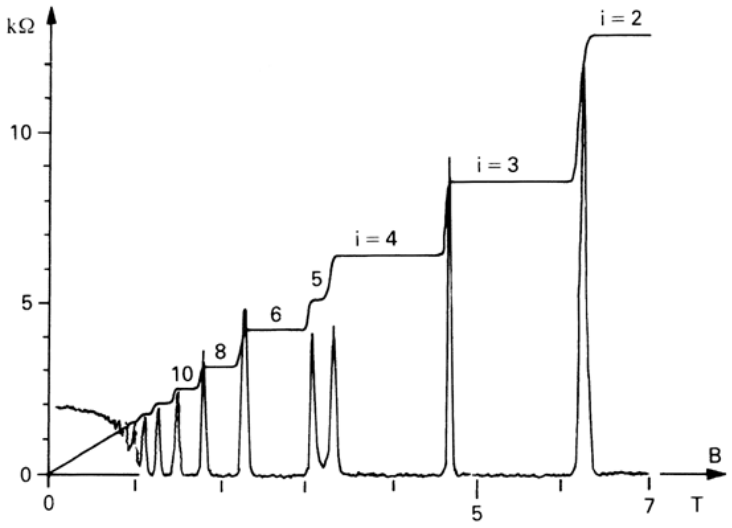


Figure 1.2: Integer quantum Hall resistivity measurements. The plot shows the measurements of the plateaus for the Hall resistivity ρ_{xy} and peaks for the longitudinal resistivity ρ_{xx} respectively, as a function of the magnetic field. The label $i = \nu$ is the number of occupied Landau levels. Figure from Ref. [67].

field is

$$B = \frac{n}{\nu}\frac{2\pi\hbar}{e} = \frac{n}{\nu}\Phi_0\,, \tag{1.7}$$

where $\Phi_0 = 2\pi\hbar/e$ is the flux quantum. The value of the magnetic field for which the resistivity has a jump corresponds to a change in the number of filled Landau levels in the system. However, along the plateaus, the value of the resistivity stays constant even when the magnetic field strength varies. The diagonal terms of the resistivity also show unexpected behaviour. Along a plateau of the ρ_{xy}, the diagonal component of the resistivity ρ_{xx} is zero. A key component necessary to explain this behaviour is the presence of disorder in the system [66].

When the disorder in the system is diminished, the diagonal resistivity peaks disappear, but other plateaus appear at fractional values. This is the fractional quantum Hall effect, first discovered in 1982 [21]. The Hall resistivity has the same value as for the integer quantum Hall effect, as in Eq. (1.6), but the values of ν are no longer integer but fractional, although only specific fractions are present.

A significant difference in the theoretical explanation of the integer and fractional quantum Hall effects is that the integer is understood through single-particle physics. For the fractional effect, single-particle physics is not able to predict plateaus of the conductivity at fractional values of the filling, therefore the interactions between the electrons need to be taken into account.

The experimental observation of these phenomena occurs when the movement of electrons is constrained to two dimensions. The first observation of the integer quantum Hall effect was performed in a Si metal-oxide-semiconductor-field-effect transistor (MOSFET) which is a system where electrons are trapped between an insulator and semiconductor layers. The integer quantum Hall has been observed in heterostructures [20, 21, 68, 69], graphene [70], surface of 3D topological insulators [71]. The fractional quantum Hall effect was observed in a $GaAs$-$GaAlAs$ heterostructure. Although much of the subsequent experiments have been carried out in $GaAs$ systems, both effects have been observed in other systems such as graphene [72].

1.1.3.1 Landau level physics

To get a better understanding of the integer and fractional quantum Hall effects, we introduce some results on the quantum mechanical behaviour of charged particles in a magnetic field. We will present only the necessary facts, not including the complete derivations for the sake of brevity, which can be found in Ref. [73].

Let us consider an electron in a magnetic field. When the magnetic field is sufficiently strong, we can consider the electron to be effectively spinless. In this case, assuming a non-zero g-factor, the Zeeman splitting is sufficiently large for the low energy spectrum of the system to consist of only one spin type.

The Hamiltonian of an electron in a magnetic field reads

$$H = \frac{1}{2m}(\boldsymbol{p} + e\boldsymbol{A})^2 \,, \tag{1.8}$$

where $\boldsymbol{p}$ is the canonical momentum operator and $\boldsymbol{A}$ is the vector potential such that $\boldsymbol{B} = \nabla \times \boldsymbol{A}$. The momentum and position operators obey the commutation relations $[x_i, p_j] = i\hbar\delta_{ij}$ and $[x_i, x_j] = [p_i, p_j] = 0$. The gauge symmetry of the systems is such that the solution of the Schrodinger's equation for the wavefunction ψ is invariant under the transformations

$$\boldsymbol{A} \to \boldsymbol{A} + \boldsymbol{\nabla}\chi \tag{1.9}$$

$$\psi \to e^{-\frac{ie}{\hbar}\chi}\psi\,, \tag{1.10}$$

where χ is a scalar field. We consider the electron to be constrained to move in the (x, y) plane and for $\boldsymbol{B}$ to be purely in the z direction: $\boldsymbol{B} = (0, 0, B)$. Because of the relation between $\boldsymbol{A}$ and $\boldsymbol{B}$, the choice of $\boldsymbol{A}$ is not unique. The two preferred choices of the gauge are the Landau gauge, where $\boldsymbol{A}_L = (0, Bx, 0)$ and the symmetric gauge where $\boldsymbol{A}_S = \frac{1}{2}(-By, Bx, 0)$.

We define the mechanical momentum: $\boldsymbol{\pi} = \boldsymbol{p} + e\boldsymbol{A} = m_e\dot{\boldsymbol{x}}$, where m_e is the electron mass, with commutation relations $[\pi_x, \pi_y] = -ie\hbar B$. This allows us to rewrite the Hamiltonian in the form of a harmonic oscillator as

$$H = \frac{1}{2m}\boldsymbol{\pi}\cdot\boldsymbol{\pi} = \hbar\omega_B\left(a^\dagger a + \frac{1}{2}\right)\,, \tag{1.11}$$

where $\omega_B = eB/m_e$ is the cyclotron frequency. The lowering and raising operators a and $a^\dagger$ are defined as

$$a = \frac{1}{\sqrt{2e\hbar B}}\left(\pi_x - i\pi_y\right) \quad \text{and} \quad a^\dagger = \frac{1}{\sqrt{2e\hbar B}}\left(\pi_x + i\pi_y\right)\,, \tag{1.12}$$

with commutation relations $[a, a^\dagger] = 1$. This is the familiar Hamiltonian of a harmonic oscillator, and we know its eigenstates and energies. Using the standard notation, the eigenstates read $|n\rangle$ with $a^\dagger|n\rangle = \sqrt{n+1}|n+1\rangle$ and $a|n\rangle = \sqrt{n}|n-1\rangle$ and

have energy $E_n = \hbar\omega_B\left(n+\frac{1}{2}\right)$. The eigenstates of the Hamiltonian are equally spaced with spacing proportional to the magnetic field. Each level is called a Landau level [74]. Unlike in the standard harmonic oscillator case, all of these levels are highly degenerate. To show this, let us introduce the operators $\tilde{\boldsymbol{\pi}} = \boldsymbol{p} - e\boldsymbol{A}$, with commutation relations $[\tilde{\pi}_x, \tilde{\pi}_y] = ie\hbar B$. Using the symmetric gauge $\boldsymbol{A}_S$, the operators $\boldsymbol{\pi}$ and $\tilde{\boldsymbol{\pi}}$ commute: $[\tilde{\pi}_i, \pi_j] = 0$ and can be simultaneously diagonalised. We can define a new set of rising and lowering operators b and $b^\dagger$

$$b = \frac{1}{\sqrt{2e\hbar B}}\left(\tilde{\pi}_x + i\tilde{\pi}_y\right) \quad \text{and} \quad b^\dagger = \frac{1}{\sqrt{2e\hbar B}}\left(\tilde{\pi}_x - i\tilde{\pi}_y\right) , \tag{1.13}$$

with commutation relations $[b, b^\dagger] = 1$. This set of lowering and raising operators explain the degeneracy for the Landau levels. We define the ground state as $|0,0\rangle$ with $a\,|0,0\rangle = b\,|0,0\rangle = 0$, so that the general state of the system reads

$$|n,l\rangle = \frac{a^{\dagger n} b^{\dagger l}}{\sqrt{n!l!}}\,|0,0\rangle \ . \tag{1.14}$$

The energy of the state only depends on n and not l.

Let us now find an explicit expression for the wavefunctions of the system and start with the Landau gauge $\boldsymbol{A}_L$. The Hamiltonian of the system reads

$$H = \frac{1}{2m}\left(p_x^2 + (p_y + eBx)^2\right) \ . \tag{1.15}$$

Since H has no explicit dependence on y, it commutes with p_y and they can be simultaneously diagonalised. The eigenstates of H are a product of plane waves in the y component with wave vector k, and they read

$$\psi_k(x,y) = e^{iky} f_k(x) \, . \tag{1.16}$$

Using this ansatz, we solve the eigenvalue problem for

$$H_k = \frac{1}{2m}p_x^2 + \frac{m_e\omega_B^2}{2}(x + kl_B^2)^2\,, \tag{1.17}$$

which is the Hamiltonian for a harmonic oscillator with a shift in x of magnitude kl_B^2, where l_B is the magnetic length: $l_B = \sqrt{\frac{\hbar}{eB}}$. The full eigenstates of the system take the form:

$$\psi_{n,k}(x,y) \sim e^{iky}H_n(x + kl_B^2)e^{-(x+kl_B^2)^2/2l_B^2}\,, \tag{1.18}$$

where $H_n(x)$ are Hermite polynomials, and the wavefunctions depend on two quantum numbers n and k. By looking at the form of $\psi_{n,k}(x,y)$ we see that they are localised in the x direction but extended in the y direction. Since the energy of the state solely depends on n, the eigenstates are degenerate. If the (x,y) plane is constrained to a square with sides L_x and L_y and area $A = L_xL_y$, the number of degenerate states is

$$N = \frac{L_y}{2\pi}\int_{-L_x/l_B^2}^{0} dk = \frac{L_xL_y}{2\pi l_B^2} = \frac{eBA}{2\pi\hbar} = \frac{AB}{\Phi_0}\,, \tag{1.19}$$

where $\Phi_0 = \frac{2\pi\hbar}{e}$ is the magnetic flux quantum. N particles can occupy each Landau level.

Let us consider the symmetric gauge $\boldsymbol{A}_S$. This choice of vector potential preserves the rotational symmetry of the uniform magnetic field. It is, therefore, possible to use the angular momentum as a quantum number and diagonalise the Hamiltonian simultaneously with the angular momentum operator $J = \hbar(x\frac{\partial}{\partial y} - y\frac{\partial}{\partial x})$. Let us directly present what the eigenstates of the system look like in this gauge, without the derivation steps. Introducing the modified complex coordinates: $z = x - iy$ and $\bar{z} = x + iy$, the lowest Landau level wavefunctions take the form

$$\psi_{LLL}(z,\bar{z}) = f(z)\,e^{-|z|^2/4l_B^2}\,, \tag{1.20}$$

where $f(z)$ is a holomorphic function. A basis for the lowest Landau level wavefunctions is obtained by selecting polynomials as the functions $f(z)$ to obtain

$$\psi_{LLL,l} \sim \left(\frac{z}{l_B}\right)^l e^{-|z|^2/4l_B^2}\,. \tag{1.21}$$

These functions are the eigenstates of the angular momentum operator with eigenvalue $\hbar l$. In contrast to the Landau gauge, in the symmetric gauge, the wavefunctions distribute in concentric circles, and their radius grows for larger values of the angular momentum eigenvalue. Such a difference in the structure of the wavefunctions is not unphysical because the form of the wavefunctions is gauge dependent.

1.1.4 Integer quantum Hall effect

The integer quantum Hall effect is characterised by a Hall resistivity that takes on discrete values and shows plateaus when plotted as a function of the magnetic field, as shown in Fig. 1.2. The Hall resistivity ρ_{xy} reads $\rho_{xy} = \frac{2\pi\hbar}{e^2}\frac{1}{\nu}$. From the Drude model, the Hall resistivity is $\rho_{xy} = \frac{B}{ne}$. The density corresponding to the plateau labelled by ν is $n = \frac{B\nu}{\Phi_0}$, which is the density needed to fill ν Landau levels. This suggests that a relationship exists between the position of the plateaus and the number of filled Landau levels. Moreover, when a Landau level is filled, the system is gapped. In the presence of an electric field, there are no other states accessible to electrons, which will not move, as if they were in an insulator. The scattering time becomes $\tau \to \infty$ which explains the zero value of the longitudinal resistivity from Eq. (1.4), when the temperature of the system is sufficiently small and the higher Landau levels are not occupied: $k_B T \ll \hbar\omega_B$.

This argument explaining the relation between the position of the resistivity plateaus and the number of filled Landau levels was based in part on the classical results from the Drude model. Let us calculate the conductivity and resistivity

taking into account the quantum nature of the system for a single free particle. The current of a particle is $\boldsymbol{I} = -e\dot{\boldsymbol{x}}$, where $\dot{\boldsymbol{x}}$ is the velocity operator $\dot{\boldsymbol{x}} = \boldsymbol{p} + e\boldsymbol{A}$ and $\boldsymbol{p}$ is the canonical momentum. The total current then reads

$$\boldsymbol{I} = -\frac{e}{m} \sum_{\text{filled states}} \langle\psi| - i\hbar\boldsymbol{\nabla} + e\boldsymbol{A}|\psi\rangle \,. \tag{1.22}$$

Using the Landau gauge $\boldsymbol{A}_L$, and adding an electric field $\boldsymbol{E} = (E, 0, 0)$ in the x direction the system Hamiltonian from Eq. (1.15) has an additional term $-eEx$ and the wavefunctions from Eq. (1.17) become $\psi_{n,k}(x, y) \to \psi_{n,k}(x - m_e E/eB^2, y)$. Considering ν filled Landau levels we find that

$$I_x = -\frac{e}{m} \sum_{n=1}^{\nu} \sum_{k} \langle\psi_{n,k}| - i\hbar \frac{\partial}{\partial x} |\psi_{n,k}\rangle = 0 \,, \tag{1.23}$$

and

$$I_y = -\frac{e}{m} \sum_{n=1}^{\nu} \sum_{k} \langle\psi_{n,k}| - i\hbar \frac{\partial}{\partial y} + exB|\psi_{n,k}\rangle = -\frac{e}{m} \sum_{n=1}^{\nu} \sum_{k} \langle\psi_{n,k}|\hbar k + eBx|\psi_{n,k}\rangle \,. \tag{1.24}$$

Using this gauge, the $|\psi_{n,k}\rangle$ are the product of a standing wave and a shifted harmonic oscillator eigenstates and we find that

$$I_y = -e\nu \sum_{k} \frac{E}{B} \,, \tag{1.25}$$

and the sum over k is the number of states which is equal to $N = AB/\Phi_0$. Using the current density $\boldsymbol{J} = \boldsymbol{I}/A$ we obtain

$$\boldsymbol{E} = \begin{pmatrix} E \\ 0 \end{pmatrix} \quad \Rightarrow \quad \boldsymbol{J} = \begin{pmatrix} 0 \\ -e\nu E/\Phi_0 \end{pmatrix} \,, \tag{1.26}$$

which gives as a result the conductivity and resistivity tensors

$$\sigma_{xx} = 0 \quad \text{and} \quad \sigma_{xy} = \frac{e}{\Phi_0}\nu \quad \Rightarrow \quad \rho_{xx} = 0 \quad \text{and} \quad \rho_{xy} = -\frac{\Phi_0}{e}\frac{1}{\nu} = -\frac{2\pi\hbar}{e^2}\frac{1}{\nu}\,. \quad (1.27)$$

These relations describe the position of the resistivity plateaus observed in the integer quantum Hall experiments as a function of the number of completely filled Landau levels.

A remarkable feature of quantum Hall systems is the presence of edge modes. The classical description of the system gives the intuition for their existence. Charged particles in a magnetic field will move along cyclotron orbits. In a finite system, the trajectories of the particles are modified in the proximity of the boundaries of the system. The particles are constrained to stay inside of the system and can no longer perform a circular motion. When they collide with the boundaries, they bounce back and keep moving in the same direction. This leads to a current close to the edge. On the opposite edge, the motion of the particles is in the opposite direction because of their circular trajectories. These particles will collide and bounce back, leading to an opposite current. Currents flowing in opposite directions are called chiral and are such that the total current in the system vanishes in the absence of an external field.

The quantisation of the Hall conductivity can be additionally explained through Laughlin's thought experiment [75]. Let us consider electrons constrained to move on the surface of a cylinder in the presence of a magnetic field orthogonal to its surface. Let us thread a magnetic flux Φ through the axis of the cylinder. Since the flux is inside of the cylinder, it does not directly affect the electrons that lie on its surface. However, the corresponding vector potential becomes non-zero on the surface of the cylinder. By slowly adding one flux quantum through the cylinder, from 0 to Φ_0, an electric field is induced around the cylinder, which affects the motion of the electrons. Laughlin showed that when ν Landau levels are filled, then exactly ν electrons will

be transferred between the two edges of the cylinder, leading to the Hall conductivity $\sigma_{xy} = \frac{e^2}{2\pi\hbar}\nu$.

When a Landau level is completely filled, the calculation of the conductivity resulting in Eq. (1.27) explains the position of the peaks and plateaus for the conductivity and the resistivity. It does not, however, explain why the plateaus extend through a range of values of the magnetic field, for which the occupation of a Landau level is only partial. In order to understand this, the role of disorder needs to be taken into account. Any experimental sample is not perfect and presents impurities. The impurities are modelled in the Hamiltonian through an external potential V. Let us assume that this potential is sufficiently small such that $V \ll \hbar\omega_B$. From perturbation theory, the effect of the potential, which will be random because it represents the presence of impurities, is that of breaking the degeneracy of the Landau levels. The spectrum of the Landau levels will not only be peaked at the values $E_n = \hbar\omega_B(n + 1/2)$ but will spread around these values. Secondly, the effect of the potential is that of turning some of the states from extended to localised. By localised, we mean that the state occupies a finite region of the sample, whereas an extended state spreads throughout the sample. We can intuitively understand this behaviour using a classical argument assuming that the potential varies on a scale greater than the magnetic length. When this is the case, the cyclotron orbit of the electrons will occur in a region of space where the potential is essentially constant, and the orbit of its guiding centre will drift along equipotential lines. Because of the randomness of the sample, some of the equipotential lines will be localised; however, there will be equipotential lines that extend throughout the borders of the sample close to its edges. States at the edges of the band, which are constrained to move along the higher or lower equipotentials of V, will be localised and the ones in the centre of the band will be extended. Only the extended states can transfer charge between the edges of the system and contribute to the conductivity [76]. We can, therefore, explain the existence of the plateaus,

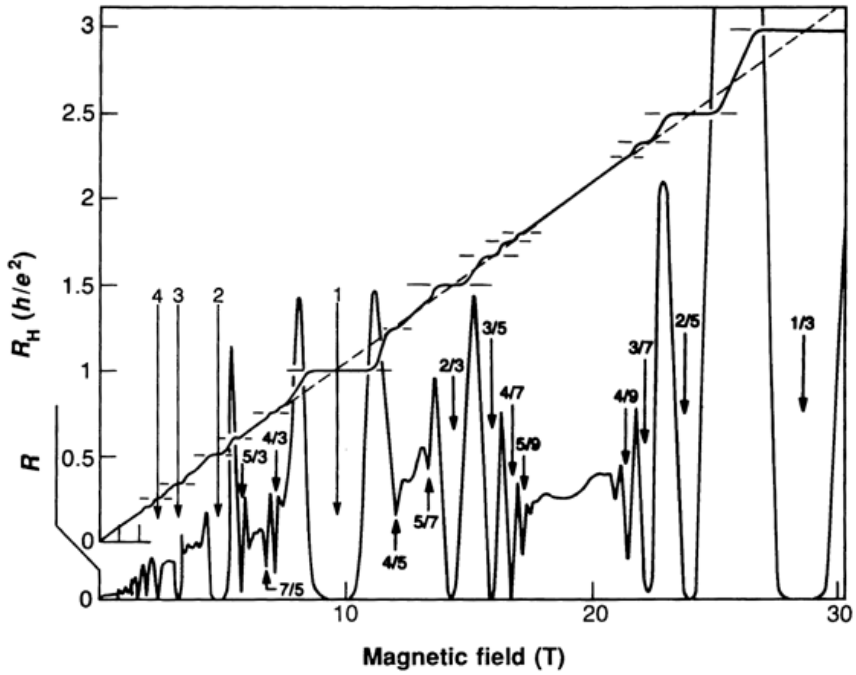


Figure 1.3: Fractional quantum Hall resistivity measurements from Ref. [77]. The plot shows the measurements of the plateaus and peaks for the Hall resistivity ρ_{xy} (R_{H} in the plot) and resistivity ρ_{xx} (R in the plot) respectively as a function of the magnetic field.

noticing that when the magnetic field changes, only localised states of a higher band will be first occupied. These states will not affect the conductivity of the system since they are localised.

1.1.5 Fractional quantum Hall effect

Single-particle physics is no longer sufficient to explain the presence of resistivity plateaus for fractional values of ν [21, 77] as shown in Fig. 1.3. It becomes necessary to take the interactions between the electrons into account. The Hamiltonian for a system of N_e interacting electrons in a magnetic field reads

$$H = \sum_{j=1}^{N_e} \frac{1}{2m_2}(\boldsymbol{p}_j + e\boldsymbol{A}_j)^2 + \sum_{j<k}^{N_e} \frac{e^2}{4\pi\epsilon|\boldsymbol{r}_j - \boldsymbol{r}_i|}\,, \tag{1.28}$$

where ϵ is the electric permittivity.

When a Landau level is only partially filled, the ground state of the system is highly degenerate because the Landau orbitals can be filled in a large number of ways. This makes the system hard to treat perturbatively, and other methods become necessary. The problem is simplified, assuming that the interaction is weak compared to the gap between Landau levels. Under this assumption, the kinetic part of the Hamiltonian can be neglected, and it is assumed that all of the electrons occupy the lowest Landau level.

Laughlin first introduced a wavefunction that explains the physics of the fractional quantum Hall effect for filling fractions $\nu = 1/m$, for m an odd integer [26]. Laughlin's wavefunction reads

$$\psi(z_1, \ldots, z_{N_e}) = \prod_{i<j}^{N_e} (z_i - z_j)^m e^{-\sum_{i=1}^{N_e} |z_i|^2/4l_B^2}\,, \tag{1.29}$$

where $z_j = x_j - iy_j$ are the complex coordinates of the electrons and l_B is the magnetic length. For m odd, the wavefunction is anti-symmetric for the exchange of any two particles, as it should be for fermions. The factor multiplying the exponential is such that the wavefunction has zero value whenever two particles are in the same position. This is a consequence of the particles interacting through Coulomb interaction, which energetically favours electrons being far apart. At the same time, the exponential factor becomes small when particles are far away from the origin, as a consequence of the particles being in the lowest Landau level as per Eq. (1.20); so the wavefunction describes the competition between these two terms. The Laughlin wavefunction is an educated guess for the ground state of the system. It has been numerically shown that, for a small number of particles, the overlap of the Laughlin wavefunction with the exact ground state of the system is greater than 99%, for $\nu = 1/3$ and $\nu = 1/5$ [78, 79]. Although this wavefunction is accurate for a small number of particles,

it is appropriate to think of it as being in the same universality class of the actual ground state and to be able to describe many of its properties. When m is even, the Laughlin wavefunction has bosonic symmetry properties and describes the bosonic version of the fractional quantum Hall effect which could be obtained with ultracold atoms [42].

By setting $m = 1$, the wavefunction describes the $\nu = 1$ integer quantum Hall state where a single Landau level is completely filled. As mentioned in the previous section, the integer quantum Hall effect is explained through single-particle physics. Therefore, its many-particle wavefunction will be a Slater determinant of single-particle wavefunctions in the lowest Landau level. The form of the LLL wavefunctions with increasing angular momentum is

$$\psi_l(z) \sim z^{l-1} e^{-|z|^2/4l_B^2}\,, \tag{1.30}$$

where l goes from 1 to N_e. The result of the Slater determinant becomes

$$\psi(z_1, \ldots, z_{N_e}) = \prod_{i<j}^{N_e} (z_i - z_j) e^{-\sum_{i=1}^{N_e} |z_i|^2/4l_B^2}\,, \tag{1.31}$$

and corresponds to the Laughlin wavefunction for $m = 1$ indicating that it also accurately describes the ground state of the $\nu = 1$ integer quantum Hall state. The term $\prod_{i<j}^{N_e}(z_i - z_j)$ is the so-called Vandemonde determinant.

When $m > 7$, the Laughlin state is no longer the energetically preferred configuration for the electrons. In that case, they will position themselves into a 2D triangular lattice called Wigner crystal [80].

The Laughlin wavefunction is shown to be the exact ground state of a different Hamiltonian [81, 82]

$$H = \sum_{l=1}^{\infty} \sum_{i<j} v_l \mathcal{P}_l(ij)\,, \tag{1.32}$$

where $\mathcal{P}_l(ij)$ is an operator that projects the wavefunction onto the state where particles i and j have relative angular momentum l. By choosing the values of v_l such that $v_l = 1$ when $l < m$ and zero otherwise, the Laughlin wavefunction becomes the exact ground state of the Hamiltonian when a confining potential is added. The Laughlin wavefunction is, in fact, the ground-state wavefunction with the smallest spatial extension.

A staggering property of the Laughlin state is that it supports exotic excitations, which carry a fractional charge. Quasi-holes for a Laughlin state at filling $\nu = 1/m$ carry charge $q = e/m$, and quasiparticle excitations have charge $q = -e/m$. This property is remarkable but does not defy any physical law. In fact, despite the excitations having fractional charge, the complete system still has a total charge which is an integer multiple of the electron charge. When a new particle is added to a Laughlin function, it will split into m independent quasiparticles, each carrying a fractional amount of charge. This phenomenon has been experimentally observed [83].

Probably the most striking property of these excitations is that they have fractional statistics [84]. Particles are either bosons or fermions in three dimensions, but this distinction no longer holds in two dimensions. Particles in two dimensions can have any intermediate statistics and are called anyons [85]. The quasiparticle excitations of a $\nu = 1/m$ Laughlin state have statistics $1/m$. A 2-quasiparticle wavefunction acquires a complex phase $i2\pi/m$ when the two quasiparticles are interchanged. This behaviour is neither fermionic nor bosonic.

The Laughlin state also supports another type of excitation, which is neutral. This excitation is similar to the phonon excitation of a superfluid, but it is gapped. The energy dispersion relation of the excitation shows a minimum at a fixed momentum k, which is called a magneto-roton [73].

The Laughlin state also reproduces the correct value of the Hall conductivity. Repeating Laughlin's thought experiment [75, 76] it is shown that threading a flux

$\Phi = m\Phi_0$ through the cylinder, one electron charge is transferred between the two edges. This leads to a fractional Hall conductivity: $\sigma_{xy} = \frac{e^2}{2\pi\hbar}\frac{1}{m}$.

The experimental results for the Hall conductivity and resistivity show the existence of several other values of the filling fraction, apart from $\nu = 1/m$, exhibiting conductivity plateaus which are not described by the Laughlin function. A set of these plateaus is explained by the so-called *hierarchical states* [81, 86, 87]. The intuition behind these states is that of considering a modified density of particles compared to a Laughlin state to account for the different filling fraction. These configurations are thought of as a Laughlin state with the addition of a fixed number of quasiparticle excitations. The quasiparticles configure themselves in a quantum Hall state as if they were electrons. These states explain plateaus at filling fractions $\nu = \frac{1}{m\pm\frac{1}{2p}}$ for m and p integers. This procedure can be repeated again leading to filling fractions: $\nu = \frac{1}{m\pm\frac{1}{2p_1\pm\frac{1}{2p_2\pm\cdots}}}$. This set of states can also be interpreted using the concept of composite fermions [88]. The general idea is that of defining a composite fermion as an electron with an even number of magnetic flux quanta attached to it. Because of this, they experience a modified magnetic field B' and a modified filling fraction ν'. A remarkable result of this approach is that the fractional quantum Hall effect can be interpreted as an integer Hall effect for composite fermions.

1.1.6 Topological order and topological entanglement entropy

Fractional quantum Hall ground states are a prime example of topologically ordered phases.

The topological entanglement entropy is used as a means of characterising the topological order of a system [89]. Let us consider a system divided into two subsystems, named A and B, and calculate the bipartite entanglement entropy between them in the ground state $|\Psi\rangle$. By tracing out the degrees of freedom of B from the density matrix of the system $\rho = |\Psi\rangle\langle\Psi|$, we obtain the reduced density matrix

$\rho_A = Tr_B |\Psi\rangle \langle\Psi|$. The entanglement entropy $\mathcal{S}_A$ is defined as the von Neumann entropy of ρ_A: $\mathcal{S}_A = -Tr_A[\rho_A \ln \rho_A]$ [90]. For systems in d dimensions with a finite correlation length l, the entanglement entropy satisfies the area law [91, 92]: $\mathcal{S}_A \simeq \alpha \mathcal{L}^{d-1}$, where $\mathcal{L} \gg l$ is the length that defines the scale of the boundary of A and α is a non-universal constant [93]. The physical meaning of this statement is that the entanglement between A and B lies at the boundary between the two parts.

For topological phases in two dimensions, a correction term exists to the area law expression [89] $\mathcal{S}_A = \alpha\mathcal{L} - \gamma + ...$, where the ellipses represent terms that vanish for $\mathcal{L} \to \infty$ and γ is the *topological entanglement entropy*. It is a universal additive constant that characterises a global entanglement feature of the ground state, as opposed to the area law term that arises from the correlations close to the boundaries between the two parts.

The topological entanglement entropy can then be used as a way to characterise the topological order of a phase, but it does not uniquely determine it. The advantage of this quantity is that it reduces the information contained in the reduced density matrix to a single number. Therefore, to see if the system is in a topological phase, it is sufficient to calculate the topological entanglement entropy. If it is non-zero, then the system shows topological properties.

Additional information about the entanglement properties of the ground state is obtained from the *entanglement spectrum*, which also carries information about the excitations of the system [94]. Let $|\Psi\rangle$ be a quantum state which is decomposed in the basis $|\lambda\rangle$, and let us assume that this basis can be written as the tensor product of two orthonormal bases $|\lambda\rangle_A$ and $|\lambda\rangle_B$ with $|\lambda\rangle = |\lambda\rangle_A \otimes |\lambda\rangle_B$. This gives a natural bipartition of the system into part A and B. The state $|\Psi\rangle$ is written as

$$|\Psi\rangle = \sum_{\lambda_A, \lambda_B} c_{\lambda_A, \lambda_B} |\lambda\rangle_A \otimes |\lambda\rangle_B \ . \tag{1.33}$$

The coefficients c_{λ_A,λ_B} are thought of as the elements of a matrix C, which has dimensions equal to those of the subsystems A and B. Performing a singular value decomposition of this matrix we get: $C = USV^\dagger$, where $U^\dagger U = 1$ and $VV^\dagger = 1$, which means that U and V have orthonormalised columns and rows respectively. S is a diagonal matrix whose entries are all non-negative and can be written as $e^{-\xi_i/2}$. The singular value decomposition is used to get the Schmidt decomposition of $|\Psi\rangle$:

$$|\Psi\rangle = \sum_i e^{-\xi_i/2} |A : i\rangle \otimes |B : i\rangle \ , \tag{1.34}$$

where $|A : i\rangle = \sum_{\lambda_A} U^\dagger_{i,\lambda_A} |\lambda_A\rangle$ and $|B : i\rangle = \sum_{\lambda_B} V^\dagger_{i,\lambda_B} |\lambda_B\rangle$. This way of writing the wavefunction is particularly appropriate to calculate the spectrum of the reduced density matrix. Taking $\rho = |\Psi\rangle \langle\Psi|$ and tracing out B to get ρ_A, the spectrum of ρ_A is given by the square of the Schmidt coefficients $e^{-\xi_i}$. It is worth pointing out that both ρ_A and ρ_B have the same spectrum. The *entanglement spectrum* is defined as the set $\{\xi_i\}$.

1.1.7 Bosonic quantum Hall states

As introduced in Section 1.1.5, the Laughlin wavefunction at filling fraction $\nu = 1/m$, with m even, describes a fractional quantum Hall state for bosonic particles. One motivation of this thesis is to guide future experiments, mainly using ultracold atoms in optical lattices. Because experimental capabilities with regard to bosonic particles have been longer developed than the corresponding capabilities with fermions, and there exists a more extensive literature with bosons, this thesis will consider the study of bosonic gases. The high degree of tunability and control of ultracold gas experiments makes them an ideal alternative to condensed matter systems, where impurities are present. This makes them a promising setting for the development of topological quantum computing utilising non-Abelian anyons, which are argued to

be present as excitations for the bosonic quantum Hall states with filling $\nu = 1$ and $\nu = 3/2$ [4, 29]. Moreover, through the use of artificial gauge fields, optical lattice setups allow for the achievement of parameter regimes unattainable in solid-state settings. In particular, because of the small size of the crystal lattice in solids, high values of the magnetic flux density require huge magnetic fields. The large magnetic flux regime is however reachable with artificial gauge fields.

Because of this, we will focus our analysis on studying fractional quantum Hall states made with bosonic particles.

In the next section, we will introduce the Bose-Hubbard model and two of its extensions, which are at the basis of the experimental realisation of the systems we consider.

1.2 Quantum simulation with ultracold atoms

Optical lattices populated with ultracold atoms can be used as quantum simulators to study Hamiltonians characteristic of condensed matter systems in a way that can outperform other numerical means computation [15, 95]. Quantum simulation is naturally able to deal with the exponential increase in the size of the Hilbert space [96]. The ultracold atom setting is highly and reliably tunable and gives access to regimes not available in condensed matter systems.

A significant amount of progress has been made recently on the quantum simulation of several models using ultracold atoms in optical lattices. The superfluid-to-Mott insulator transition in the Bose-Hubbard model was achieved in 2002 [97], and a Mott insulator state of the Fermi-Hubbard model was realised in 2008 [98]. The development of quantum gas microscopes both for bosons and fermions [99, 100] has enabled the detection of single atoms and made ultracold atoms an even more versatile toolbox.

In the next sections, we will introduce the Bose-Hubbard model, which is the archetypal model describing ultracold atoms in optical lattices, and two of its extensions. Firstly, we will consider the dipolar Bose-Hubbard model, in which the bosons interact with a long-range dipolar interaction, appropriate to describe interacting polar molecules. Secondly, we will consider the bosonic Harper-Hofstadter model in the presence of local interactions, which can be thought of as a Bose-Hubbard model with the addition of an artificial gauge field. This model describes quantum Hall physics in an optical lattice.

1.2.1 Bose-Hubbard model

We now introduce the Bose-Hubbard (BH) model [101] and describe its main properties. For a more comprehensive review of the topic, we refer to [13].

The BH model describes bosons hopping on a lattice and interacting via on-site interactions. The BH model allows for the study of strongly-correlated particle systems and provides the basic framework necessary to understand the models that we will study in this thesis.

Let us consider a gas made of N interacting spinless bosons, in the presence of an optical lattice described by the external potential V_{ext}. The Hamiltonian of the system in second quantisation reads

$$\begin{aligned}\hat{H}(t) = &\int d\boldsymbol{r}\, \hat{\Psi}^\dagger(\boldsymbol{r},t)\left[-\frac{\hbar^2}{2m}\boldsymbol{\nabla}^2 + V_{ext}\right]\hat{\Psi}(\boldsymbol{r},t) + \\ &+\frac{1}{2}\int d\boldsymbol{r}\, d\boldsymbol{r}' \hat{\Psi}^\dagger(\boldsymbol{r},t)\hat{\Psi}^\dagger(\boldsymbol{r}',t)V(\boldsymbol{r}-\boldsymbol{r}')\hat{\Psi}(\boldsymbol{r},t)\hat{\Psi}(\boldsymbol{r}',t)\,, \end{aligned} \tag{1.35}$$

where $\hat{\Psi}^\dagger(\boldsymbol{r},t)$ and $\hat{\Psi}(\boldsymbol{r},t)$ are the bosonic creation and annihilation field operators obeying bosonic commutation relations $[\hat{\Psi}(\boldsymbol{r},t), \hat{\Psi}^\dagger(\boldsymbol{r}',t')] = \delta(\boldsymbol{r}-\boldsymbol{r}')\delta(t-t')$, m is the mass of the bosons and $\hbar$ is the reduced Planck's constant. The particles interact

through a contact potential

$$V(\boldsymbol{r}-\boldsymbol{r}') = g\delta(\boldsymbol{r}-\boldsymbol{r}')\,, \tag{1.36}$$

where $g = 4\pi\hbar^2 a_s/m$ and a_s is the s-wave scattering length that describes the interaction at low energies between neutral atoms. The actual interaction potential can be described through the contact term when the de Broglie wavelength of the particles is much larger than its range. The scattering length is positive for a repulsive interaction and negative when it is attractive.

Let us consider the three-dimensional potential V_{ext} that defines the lattice structure

$$V_{ext} = \sum_{i=x,y,z} V_i \sin^2(\pi i/a_i)\,. \tag{1.37}$$

The lattice potential is generated by a set of counter-propagating lasers beams with same phase and polarisation and with wavelength λ_i, which generates a standing wave. The lattice constant is $a_i = \lambda_i/2$ in the i direction and V_i is the amplitude of the potential in each direction which is proportional to the intensity of the laser.

When the potential is sufficiently deep and the temperature sufficiently low, only the lowest Bloch band of the potential needs to be considered. The field operators $\hat{\Psi}$ can be expanded into the basis of Wannier states [102, 103]. The Wannier states are superpositions of the wavefunctions of the lowest band, which are highly localised and centred at the lattice sites. They have the form $w_i(\boldsymbol{r}) = w(\boldsymbol{r}-\boldsymbol{R}_i)$, where $\boldsymbol{R}_i$ is the position vector of a minimum of the lattice potential. The expansion of the field operators, covering the lowest band, in this basis reads [18]

$$\hat{\Psi}(\boldsymbol{r}) = \sum_i w_i(\boldsymbol{r})\hat{b}_i\,. \tag{1.38}$$

This is the so-called tight-binding approximation. The operators $\hat{b}_i$ and $\hat{b}_i^\dagger$ are the

annihilation and creation operators of bosons localised at site i and obey the bosonic commutation relations $[\hat{b}_i, \hat{b}_j^\dagger] = \delta_{ij}$. Using this expansion for the field operators, we obtain a new form of the Hamiltonian which reads

$$\hat{H} = -\sum_{\langle i,j \rangle} J_{ij} \hat{b}_i^\dagger \hat{b}_j + \frac{U}{2} \sum_i \hat{n}_i(\hat{n}_i - 1) - \mu \sum_i \hat{n}_i \,, \tag{1.39}$$

where $\langle \ldots \rangle$ denotes a sum over nearest-neighbour sites, $\hat{n}_i = \hat{b}_i^\dagger \hat{b}_i$ is the number operator at site i and μ is the chemical potential. The first term in Eq. (1.39) represents the hopping of bosons between nearest-neighbour sites, the second term represents the on-site interaction and the third term controls the number of particles in the system. This is the Bose-Hubbard Hamiltonian.

As a consequence of the highly localised form of the Wannier functions, the tunnelling between sites which are more than one site apart is neglected. The tunnelling amplitude between neighbouring lattice sites J_{ij} reads

$$J_{ij} = -\int d\boldsymbol{r}\; w_i^*(\boldsymbol{r}) \left[-\frac{\hbar^2}{2m} \boldsymbol{\nabla}^2 + V_{\text{ext}} \right] w_j(\boldsymbol{r}) \,, \tag{1.40}$$

and the contact potential interaction term becomes

$$U = g \int d\boldsymbol{r}\;\; |w_i(\boldsymbol{r})|^4 \,. \tag{1.41}$$

In the presence of an external trapping potential V_{trap}, which has the purpose of confining the particles, another term is added to the Hamiltonian: $\hat{H}_{\text{trap}} = \sum_i \epsilon_i \hat{n}_i$. The term

$$\epsilon_i = \int d\boldsymbol{r}\, V_{trap}(\boldsymbol{r})\, |w_i(\boldsymbol{r})|^2 \approx V_{trap}(\boldsymbol{R}_i) \,, \tag{1.42}$$

is an energy offset at each site and can be included in the previous Hamiltonian by introducing a site-dependent chemical potential as $\mu_i = \mu + \epsilon_i$.

To obtain a two-dimensional geometry on the (x, y) plane, we consider a lattice potential in the x and y directions combined with a tight harmonic trapping potential in the z direction. The overall external potential reads

$$V_{ext}(\boldsymbol{r}) = V_0 \left[\sin^2(\pi x/a_x) + \sin^2(\pi y/a_y)\right] + \frac{1}{2} m\Omega_z^2 z^2 \,, \tag{1.43}$$

where Ω_z is the frequency a tight harmonic trapping potential.

The Bose-Hubbard model described by the Hamiltonian in Eq. (1.39) in the grand-canonical ensemble, is characterised by three parameters: the hopping amplitude J (assuming $J_{ij} = J$ for all i, j), the on-site interaction strength U and the chemical potential μ. The phase diagram of the system is usually expressed as a function of J/U and μ/U. In the small interaction limit, when $J/U \gg 1$, the ground state of the system is superfluid, it has gapless excitations, on-site density fluctuations and the bosons are delocalised throughout the lattice. In the large interaction limit, $J/U \ll 1$, and for integer filling of the lattice, the ground state is the so-called Mott insulator, in which there are no on-site fluctuations, and each site is occupied by an integer number of bosons. In this case, the system is gapped and incompressible because there is a finite energy cost for adding an extra particle. The integer filling with n_b bosons per site occurs when the chemical potential is $n_b - 1 \leq \mu/U \leq n_b$. The regions in the $(\mu/U, J/U)$ phase diagram where the ground state is a Mott insulator are called Mott lobes, and the critical values $(J/U)_c$ depend on the dimensionality of the system as well as on its geometry. When the filling is non-integer, the ground state is always superfluid.

1.2.1.1 Extended Bose-Hubbard model

Let us consider an extension of the BH model where the interaction between the bosons in Eq. (1.35) is no longer just a contact interaction but is long-ranged. Such

an interaction can be realised through static dipole-dipole interactions. When all of the dipoles are polarised in the same direction, the interaction potential takes the form

$$V_{\rm dd}(\boldsymbol{r}-\boldsymbol{r}') = g\delta(\boldsymbol{r}-\boldsymbol{r}') + D^2\frac{(1-3\cos^2\theta)}{|\boldsymbol{r}-\boldsymbol{r}'|^3}\,, \tag{1.44}$$

where D is the dipole moment of the bosons and θ is the angle between the direction of the polarisation and the vector $\boldsymbol{r}-\boldsymbol{r}'$. The interaction potential $V_{dd}(\boldsymbol{r}-\boldsymbol{r}')$ is composed of a contact term and a long-range term which is anisotropic. Using the expansion in the Wannier functions, the dipolar interaction term of the Hamiltonian reads

$$\hat{H}_{\rm dd} = \sum_{ijkl}\frac{U_{ijkl}}{2}\,\hat{b}_i\hat{b}_j^\dagger\hat{b}_k^\dagger\hat{b}_l\,, \tag{1.45}$$

with matrix elements U_{ijkl} given by

$$U_{ijkl} = \int d\boldsymbol{r}_1 d\boldsymbol{r}_2\; w_i^*(\boldsymbol{r}_1)w_j^*(\boldsymbol{r}_2)V_{\rm dd}(\boldsymbol{r}_1-\boldsymbol{r}_2)w_k(\boldsymbol{r}_2)w_l(\boldsymbol{r}_1)\,. \tag{1.46}$$

Assuming that the lattice potential is sufficiently deep that the spread of the Wannier functions is much shorter than the inter-lattice spacing, then the Wannier functions $w_i(\boldsymbol{r})$ will be significantly large only in proximity of the lattice sites $\boldsymbol{R}_i$. Therefore, only some of the terms U_{ijkl} will be non-negligible. These terms are the off-site terms U_{ijij} for $k=i\neq j=l$, and the on-site terms U_{iiii}. The off-site contribution reads

$$U_{ijij} \simeq V_{\rm dd}(\boldsymbol{R}_i-\boldsymbol{R}_j)\int d\boldsymbol{r}_1|w_i(\boldsymbol{r}_1)|^2\int d\boldsymbol{r}_2|w_j(\boldsymbol{r}_2)|^2\,, \tag{1.47}$$

where the $V_{dd}(\boldsymbol{r}_1-\boldsymbol{r}_2)$ have been substituted with $V_{dd}(\boldsymbol{R}_1-\boldsymbol{R}_2)$ under the assumption that it changes slowly over distances larger than the spread of the Wannier functions. The Hamiltonian for the off-site part of the dipolar interaction then reads

$$\hat{H}_{dd}^{\text{off-site}} = \frac{1}{2}\sum_{i\neq j}\frac{V_{ij}}{|i-j|^3}\,\hat{n}_i\hat{n}_j\,, \tag{1.48}$$

where $V_{\rm dd}(\boldsymbol{R}_i - \boldsymbol{R}_j) = V_{ij}/|i-j|^3$.

The on-site contribution reads

$$U_{iiii} = \int d\boldsymbol{r}_1 d\boldsymbol{r}_2 n(\boldsymbol{r}_1) V_{\rm dd}(\boldsymbol{r}_1 - \boldsymbol{r}_2) n(\boldsymbol{r}_2)\,, \tag{1.49}$$

where $n(\boldsymbol{r}) = |w(\boldsymbol{r})|^2$. The Hamiltonian for the on-site part of the dipolar interaction then reads

$$\hat{H}_{\rm dd}^{\text{on-site}} = \frac{U_d}{2} \sum_i \hat{n}_i(\hat{n}_i - 1)\,, \tag{1.50}$$

where $U_d = U_{iiii}$. The dipolar part of the interaction then reads

$$\hat{H}_{\rm dd} = \hat{H}_{\rm dd}^{\text{off-site}} + \hat{H}_{\rm dd}^{\text{on-site}} = \frac{1}{2} \sum_{i \neq j} \frac{V_{ij}}{|i-j|^3}\, \hat{n}_i \hat{n}_j + \frac{U_d}{2} \sum_i \hat{n}_i(\hat{n}_i - 1). \tag{1.51}$$

The on-site term of the dipolar interaction can be merged with the on-site term from the contact interaction of the BH model into a single term called U. When the dipoles are all polarised perpendicular to the lattice, then the angle θ in Eq. (1.44) becomes $\theta = \pi/2$. This causes the dipolar interaction to be isotropic and we set $V_{ij} = V$.

If we limit the interaction terms to be nearest neighbour (NN) only, we obtain the *extended* Bose-Hubbard model that reads

$$\hat{H}_{\rm eBH} = -J \sum_{\langle i,j \rangle} \hat{b}_i^\dagger \hat{b}_j + \frac{U}{2} \sum_i \hat{n}_i(\hat{n}_i - 1) + \frac{V}{2} \sum_{\langle i,j \rangle} \hat{n}_i\, \hat{n}_j - \sum_i \mu_i \hat{n}_i\,. \tag{1.52}$$

The presence of the NN interactions affects the phase diagram of the system. For integer fillings, the NN interaction induces the existence of a crystalline phase that shows density modulations and diagonal order named charge density wave or Mott solid. Another phase called bosonic Haldane insulator appears which presents non-local string correlations, is gapped and does not break translational symmetry [104]. When the filling is non-integer, two possible states emerge [105]: one is the super-

solid phase characterised by non-zero structure factor and diagonal long-range order together with a non-zero superfluid density. The other one is a phase-separated state which is characterised by a jump in the density as a function of the chemical potential. The system is mechanically unstable and phase separates, i.e., it splits in real space into domains where distinct phases are well defined. For smaller interaction strengths, the phase separation regions disappear in favour of the supersolid for filling larger than 1/2 [106].

1.2.2 Dipolar Bose-Hubbard model

Let us consider the full long-range character of the dipolar interaction, without imposing a cutoff at the nearest neighbours. The Hamiltonian of the system on a 2D square lattice, when the dipoles are all polarised orthogonally to the lattice plane, reads

$$\hat{H} = -J \sum_{\langle i,j \rangle} b_i^\dagger b_j + \frac{U}{2} \sum_i \hat{n}_i(\hat{n}_i - 1) + \frac{1}{2} \sum_{i \neq j} \frac{V}{|i-j|^3} \hat{n}_i \hat{n}_j - \sum_i \mu_i \hat{n}_i \,. \tag{1.53}$$

Let us consider the low filling case in the hard-core limit of $U/J \to \infty$, where double occupations of a single site are suppressed and the local Hilbert space at each site is limited to have either zero or one boson. The Hamiltonian becomes

$$\hat{H} = -J \sum_{\langle i,j \rangle} \hat{b}_i^\dagger \hat{b}_j + \frac{1}{2} \sum_{i \neq j} \frac{V}{|i-j|^3} \hat{n}_i \hat{n}_j - \sum_i \mu_i \hat{n}_i \,. \tag{1.54}$$

The phase diagram of this system was explored in [58] using Quantum Monte Carlo calculations and is shown in Fig. (1.4). We will now summarise the main features of the ground-state phase diagram, which is richer than the standard Bose-Hubbard model. The quantum phases which are observed are the superfluid, the solid, which is an insulating phase with a modulated density, and the supersolid phase which

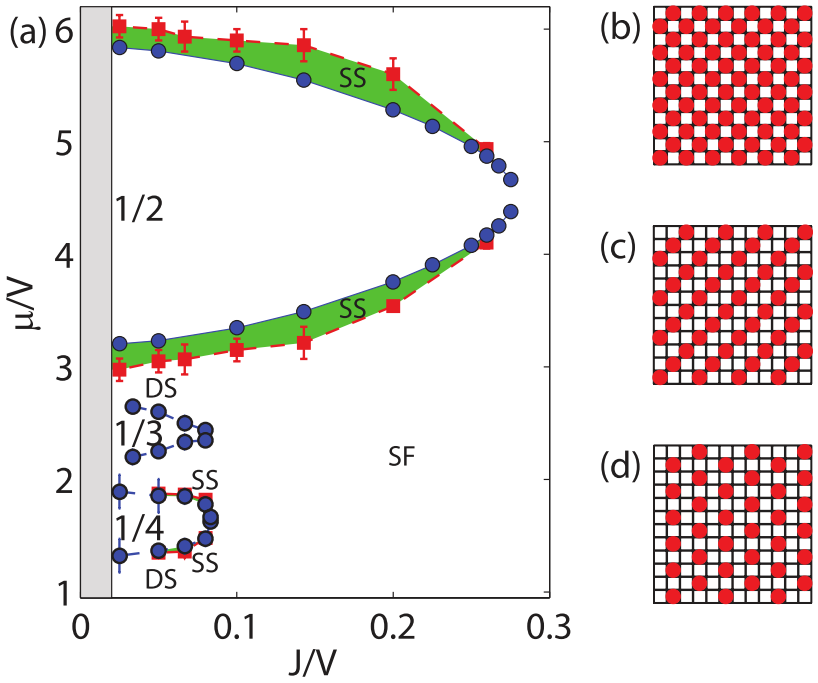


Figure 1.4: (a) Phase diagram of the dipolar BH model in the hard-core limit. Solid density patterns at filling $\nu = 1/2$ (b), $\nu = 1/3$ (c), $\nu = 1/4$ (d). The figure is from Ref. [58].

presents superfluidity at the same time as a density modulation which is different from the lattice [107, 108, 109]. Unlike in the Bose-Hubbard model, insulating phases can also be obtained at fractional fillings.

For finite values of J/V the phase diagram shows the existence of three Mott lobes characterised by a density $\nu = 1/2, 1/3$ and $1/4$. These are solid phases named checkerboard, stripe and star, respectively, and their ground-state density pattern is shown in Fig. 1.4 (b-d). These phases also survive in the presence of a confining potential and at finite temperature.

In the limit of small hopping amplitude $J/V \ll 0.1$, the ground-state phase is incompressible, with $\partial\rho/\partial\mu = 0$ for most values of μ and this is the analogue to the classical *devil's staircase*. A series of incompressible ground states which are dense between $\rho = 0$ and $\rho = 1$ is present. These states have a structure which is commensurate with that of the lattice for all rational fillings. There are no such states

in the short-range interaction case [110, 111].

For large values of J/V, the ground state of the system is a superfluid for all values of μ. For small values of J/V, the system has many metastable states resembling a glassy system which makes Quantum Monte Carlo calculations impractical. This is why the region is greyed out in Fig. 1.4 (a).

For a region of values of J/V and μ/V, a supersolid phase is found. Such a phase shows superfluid and solid order simultaneously. The choice of parameters in the system is such that the density of particles corresponds to a doped (by either adding or removing particles) Mott solid. This doping is necessary for the supersolid state to be present. The supersolid phase appears as a mid-step between the superfluid to solid transition. The supersolid phase appears both in the presence of doping and vacancies.

The long-range interactions stabilise the supersolid phase over a larger range of parameters. In the extended BH model, where the interaction is only nearest-neighbour, the supersolid phase was observed only in the presence of doping and not vacancies, although with the difference that soft-core bosons were considered [105].

In Chapter 4, we will ask which phases are supported in a finite-size dipolar BH model, and how they can be characterised using quantities available in ultracold gas experiments.

1.2.3 Lattice quantum Hall systems

The appearance of quantum Hall physics is typically induced by the presence of a magnetic field. Ultracold gases used in optical lattice experiments are neutral and therefore are immune to the Lorenz force of a charged particle in a magnetic field. This impediment has been resolved by the engineering of artificial gauge fields, created using rotating systems [31] or using light-atom interaction [30, 32, 112, 113]. The goal of these methods is that of simulating the action of a magnetic field on a charged

particle and therefore creating the analogue of an Aharonov-Bohm phase. When a particle moves in a closed loop around a lattice plaquette, it picks up the same complex phase it would if a uniform magnetic flux was flowing through the lattice.

The simplest way of modelling quantum Hall physics in this setting is that of using the Harper-Hofstadter (HH) model [34, 35, 114] with the addition of local interactions. The bosonic and fermionic versions of the HH model describe spinless particles in a two-dimensional square lattice moving with nearest-neighbour hopping in the presence of a magnetic field. The Harper-Hofstadter Hamiltonian reads

$$\hat{H} = -J \sum_{\langle i,j \rangle} \left(e^{-i\phi_{ij}} \hat{c}_i^\dagger \hat{c}_j \right) + \text{H.c.}\,, \tag{1.55}$$

where $\hat{c}_i$ and $\hat{c}_i^\dagger$ are fermionic or bosonic annihilation and creation operators. The complex phases $i\phi_{ij}$ are chosen such that a particle hopping around a plaquette of the square lattice acquires a total phase $e^{\frac{2\pi i}{\Phi_0} \oint \boldsymbol{A} \cdot d\boldsymbol{l}}$, where $\Phi_0 = h/2e$ is the magnetic flux quantum, and $\boldsymbol{A}$ is the vector potential of the magnetic field. The gauge freedom allows for different choices of the complex phases $i\phi_{ij}$ leading to the same equivalent magnetic field. We consider the ϕ_{ij} for the Landau gauge, which makes the hopping complex in the y direction and real in the x direction, leading to the Hamiltonian

$$\hat{H} = -J \sum_{x,y} \left(\hat{c}_{x,y}^\dagger \hat{c}_{x+1,y} + e^{i2\pi\alpha x} \hat{c}_{x,y}^\dagger \hat{c}_{x,y+1} \right) + \text{H.c.}\,, \tag{1.56}$$

where the x and y coordinates of the lattice have been used explicitly to label the lattice sites.

This Hamiltonian has the remarkable property that its one-particle spectrum has a fractal structure as a function of α, known as Hofstadter's butterfly. When α is an integer, there is a single energy band. When $\alpha = p/q$ is rational, the band splits into q sub-bands. When α is irrational, the band splits into an infinite number of

sub-bands. This leads to the fractal structure of the Hofstadter's butterfly.

Laser-induced tunnelling in superlattices was one of the first methods proposed to generate artificial gauge fields [30]. It works by considering atoms in an optical lattice which can be in two internal hyperfine states $|0\rangle$ and $|1\rangle$. The potential traps the two states in every other row of the lattice, at even and odd values of the y coordinate respectively. Additionally, the lattice is tilted in the y direction, introducing an energy shift Δ between neighbouring rows of the lattice. There is tunnelling in x due to kinetic energy, whereas the tunnelling in y is suppressed by the energy shift, assuming that Δ is larger than the hopping amplitude. The tunnelling in the y direction is laser-assisted through two pairs of lasers that induce a Raman transition between the states $|0\rangle$ and $|1\rangle$ between sites with y coordinate n and $n\pm1$. The energy offset for these transitions is $\pm\Delta$ and the detunings of the lasers are chosen to cancel the effect of the lattice tilting in the rotating frame. The lasers generate running waves in the x direction so that the tunnelling amplitudes in the y direction gain a local phase $e^{\pm ikx}$, where k is the running-wave wave vector. Such tunnelling term induces an Aharonov-Bohm phase on a neutral particle in the same way a charged particle in a magnetic field would be affected.

The HH model, with the addition of local interactions, has all of the ingredients we would find in a quantum Hall system, and can support quantum Hall states for appropriate filling fractions $\nu = n_b/n_\phi$, with n_ϕ the density of magnetic fluxes per plaquette and n_b the density of particles. This filling fraction has the same role as the filling fraction previously introduced for a two-dimensional electron gas. The Hamiltonian for the bosonic HH model reads

$$\hat{H} = -J \sum_{\langle i,j \rangle} \left(e^{i\phi_{ij}} \hat{b}_i^\dagger \hat{b}_j + \text{H.c.} \right) + U \sum_i \hat{n}_i (\hat{n}_i - 1) \,, \tag{1.57}$$

where $\hat{b}_i$ and $\hat{b}_i^\dagger$ are bosonic annihilation and creation operators at site i respectively,

and the on-site interaction term has been added.

1.2.3.1 Lattice fractional quantum Hall states

The bosonic HH model can also be thought of as a Bose-Hubbard model in the presence of a magnetic field. This presents an additional parameter, the density of magnetic fluxes per plaquette n_ϕ, on top of the density of bosons n_b and the interaction strength U/J, that govern the Mott insulator to superfluid transition.

This system supports quantum Hall states for appropriate filling fractions $\nu = n_b/n_\phi$ [20, 26, 115]. In the continuum limit, where $U \approx n_\phi \ll 1$, it has been established that quantum Hall states appear [31, 40, 116, 117]. In the large flux limit available in experiments, and where the physics of the system is no longer well described by the continuum limit [43, 116, 118, 119, 120], the phase diagram of the system has not yet been entirely explored. For values of $\nu = 1/q$, where q is an even integer, exact diagonalisation (ED) calculations of small system sizes with fully periodic boundary conditions [41, 42, 43, 44, 121, 122] have shown that the ground state is compatible with the lattice version of the Laughlin state. This was achieved by calculating the overlap of the ground state with the Laughlin wavefunction. The overlap has been shown to decay quickly for $n_\phi > 0.2$. Calculation of the Chern number of the system, as a measure of the topological nature of the state, and of the entanglement spectrum give values compatible with the Laughlin state for $n_\phi < 0.4$ [42, 44]. The gap in the hard-core limit is found to be of the range of $0.25J$ when $n_\phi \approx 0.1$.

The small overlap of the ground-state wavefunctions for values of $n_\phi > 0.2$ is due to two separate factors. First, the Laughlin wavefunction used to calculate the overlap is not adapted for the lattice system. Second, for large values of n_ϕ, the effect of the lattice plays a significant role [42] and differs most from the continuum limit where the Laughlin function originates.

The previous works using ED [42, 44] has also explored the relevance of the inter-

action in inducing the Laughlin state. For small flux densities $n_\phi < 0.2$, the Laughlin state is induced for any interaction strength, whereas for larger values of n_ϕ it is induced for $U/J > n_\phi$. Studies concerning the bosonic HH model on a square lattice [123, 124, 125] and on ladders have also shown the resemblance of their ground states to fractional quantum Hall states [126, 127, 128].

Studying larger sized systems becomes unfeasible using ED, and other numerical methods are needed. Cluster mean-field [129, 130] has been used as well as tensor network methods [131, 132, 133, 134, 135, 136, 123, 124, 137, 138].

In the high magnetic flux limit available to experiments, the phase diagram of the system is not yet completely explored, and direct experimental evidence of fractional quantum Hall states is still lacking [123].

In Chapter 3, we use DMRG to calculate the ground states of the system in the large flux regime. Unlike in previous works utilising tensor networks, we will consider a finite cylinder geometry, which gives us access to both bulk and edge properties of the ground state.

1.3 Numerical methods

In this section, we will introduce the basic notions underlying the numerical methods used throughout the thesis. We will describe the concepts of matrix product states (MPS), matrix product operators (MPO) and the density matrix renormalisation group (DMRG). This section is not meant to be a thorough exposition of the topic (a complete review can be found in Ref. [11]), but rather an introduction to the concepts needed to understand the numerical methods developed in Chapter 2.

1.3.1 Introduction

The DMRG algorithm has become a powerful technique for studying one-dimensional quantum lattice systems and can be formulated as a variational method that uses MPS as a variational ansatz. Since the dimension of the Hilbert space of a many-particle system grows exponentially with the system size, finding its ground state using exact diagonalisation quickly becomes computationally prohibitive, so other methods are necessary. The DMRG algorithm [5] is one such method, based on the MPS formulation of the wavefunction of the system. MPS are used to represent many-body wavefunctions of one-dimensional gapped systems efficiently, and their accuracy is controlled by a parameter χ called the *bond dimension*.

1.3.2 Matrix product states

Let us consider a 1D lattice made of N sites and a local Hilbert space of size d on each site. The local basis at site j reads $\{|i_j\rangle\}$, where $j = 1, \dots N$ labels the site and i labels the d basis states at each site. A general many-body quantum state $|\psi\rangle$, defined on this system, has wavefunction

$$|\psi\rangle = \sum_{i_1,\dots,i_N=0}^{d} c_{i_1,\dots,i_N} |i_1, \dots, i_N\rangle \ , \tag{1.58}$$

where $c_{i_1,\dots,i_N}$ is a set coefficients that completely describes the quantum state. The number of coefficients necessary to completely define the state scales exponentially with the system size. In fact, $c_{i_1,\dots,i_N}$ has d^N elements.

Using the MPS formalism, we write the wavefunction of a many-body quantum state $|\psi\rangle$ as

$$|\psi\rangle = \sum_{i_1,\dots,i_N=0}^{d} A^{[1]i_1} A^{[2]i_2} \dots A^{[N]i_N} |i_1, \dots, i_N\rangle \, . \tag{1.59}$$

In this representation of the state, $A^{[n]i_n}$ is one of d matrices, labelled by i_n, each with

site-dependent dimension $\chi_{n-1} \times \chi_n$ and elements $A^{[n]i_n}_{j_{n-1}j_n}$. $A^{[n]}$ is a rank-3 tensor, where i_n is called the physical index and j_{n-1} and j_n are called virtual indices. The superscript between square brackets indicates that, for a general state, the tensors on different lattice sites can be different. The set of coefficients $c_{i_1,\ldots,i_N}$ can be thought of as a rank-N tensor, which, in the MPS formulation, is re-written as a product of N rank-3 tensors. The dimensions of the $A^{[n]i_n}$ matrices for a fixed physical index i_n are called *bond dimensions* and are usually represented with the letter χ.

The advantage of the MPS representation lies in the fact that by setting a maximum value χ to the bond dimensions of each matrix in Eq. (1.59) ($\chi_n \leq \chi$), the number of parameters required to describe the quantum state is bound by $Nd\chi^2$, which grows linearly with the system size compared to exponentially for the full state representation of Eq. (1.58). Assuming that the wavefunction can be represented by MPS with a small χ, it becomes possible to overcome the exponential growth of the Hilbert space. This is the case for the ground states of gapped, local and one-dimensional Hamiltonians [139, 140]. For such systems, the problem of finding ground states is highly simplified. The search for the ground state is no longer performed in the full Hilbert space, but in the subspace parametrised by MPS with a fixed bond dimension.

The MPS form of a state $|\psi\rangle$ can be formally obtained from its full expression in Eq. (1.58) by using a series of singular value decompositions (SVD). Let us briefly recall the main properties of the SVD. Any $N_1 \times N_2$ matrix M can be decomposed as

$$M = USV^\dagger\,, \tag{1.60}$$

where U is a $N_1 \times \min(N_1, N_2)$ unitary matrix such that $UU^\dagger = U^\dagger U = I$, V is a $\min(N_1, N_2) \times N_2$ unitary matrix such that $VV^\dagger = V^\dagger V = I$ and S is a square $\min(N_1, N_2) \times \min(N_1, N_2)$ diagonal matrix with non-negative entries $S_{ii} = s_i$. The

set of s_i are called the *singular values* and the number n of non-zero entries is called the *Schmidt rank* of the matrix M.

We derive the MPS form of the wavefunction starting from Eq. (1.58) by using a series of SVDs. Let us start by reshaping the coefficients of the state as

$$c_{i_1,\ldots,i_N} = C_{i_1,(i_2,\ldots,i_N)}\,, \tag{1.61}$$

with dimension $d \times d^{N-1}$, and perform an SVD to obtain

$$C_{i_1,(i_2,\ldots,i_N)} = \sum_{j_1} U_{i_1,j_1} S_{j_1} V^{\dagger}_{j_1,(i_2,\ldots,i_N)}\,, \tag{1.62}$$

where U has dimension $d \times d$. We repeat the same procedure by first multiplying and reshaping $S_{j_1} V^{\dagger}_{j_1,(i_2,\ldots,i_N)}$ as $C_{(j_1,i_2),(i_3,\ldots,i_N)}$ with dimension $d^2 \times d^{N-2}$ and applying another SVD to obtain

$$C_{(j_1,i_2),(i_3,\ldots,i_N)} = \sum_{j_2} U_{(j_1,i_2),j_2} S_{j_2} V^{\dagger}_{j_2,(i_3,\ldots,i_N)}\,, \tag{1.63}$$

where U has dimension $d^2 \times d^2$. This procedure is repeated until all of the lattice indices are used to write the state as

$$|\psi\rangle = \sum_{i_1,\ldots,i_N} \sum_{j_1,\ldots,j_{N-1}} C_{i_1,j_1} C_{(j_1,i_2),j_2} \ldots C_{(j_{N-2},i_{N-1}),(j_{N-1})} C_{(j_{N-1},i_N),1} \, |i_1,\ldots,i_N\rangle\ . \tag{1.64}$$

It is convenient to rewrite this expression in a more manageable form by introducing a set of d matrices $A^{[n]i_n}$ for each site n, such that $A^{[n]i_n}_{j_{n-1},j_n} = C_{(j_{n-1},i_n),j_n}$. By representing the sum over the indices j_n through matrix multiplication, we obtain the MPS form of the state as in Eq. (1.59).

The MPS representation of the wavefunction is not unique. Inserting the identity $\mathcal{I} = TT^{-1}$ between any two $A^{[n]i_n}$, we obtain a new set of matrices $A'^{[n]i_n} = A^{[n]i_n} T$

and $A'^{[n+1]i_{n+1}} = T^{-1}A^{[n+1]i_{n+1}}$, for some invertible matrix T. The freedom in representing the MPS state is used to obtain the *canonical form* of the MPS [141, 142]. The *left-canonical* form of the MPS reads

$$|\psi\rangle = \sum_{i_1,\ldots,i_N} L^{[1]i_1} L^{[2]i_2} \ldots L^{[N]i_N} |i_1, \ldots, i_N\rangle \,, \tag{1.65}$$

where the matrices $L^{[n]i_n}$ are left-normalised, meaning that $\sum_{i_n} L^{[n]i_n\dagger} L^{[n]i_n} = \mathcal{I}$. The *right-canonical* version reads

$$|\psi\rangle = \sum_{i_1,\ldots,i_N} R^{[1]i_1} R^{[2]i_2} \ldots R^{[N]i_N} |i_1, \ldots, i_N\rangle \,, \tag{1.66}$$

where the matrices $R^{[n]i_n}$ are right-normalised: $\sum_{i_n} R^{[n]i_n} R^{[n]i_n\dagger} = \mathcal{I}$. Lastly, the *mixed-canonical* version of the MPS reads

$$|\psi\rangle = \sum_{i_1,\ldots,i_N} L^{[1]i_1} L^{[2]i_2} \ldots L^{[n]i_n} \Lambda^{[n]} R^{[n+1]i_{n+1}} \ldots R^{[N]i_N} |i_1, \ldots, i_N\rangle \,, \tag{1.67}$$

where Λ is a diagonal matrix with elements $\{s_1, s_2, \ldots\}$, and the L and R matrices are left and right-normalised respectively. The left and right-canonical versions of the MPS are obtained by iteratively applying SVDs to the A matrices and using the orthonormality properties of the U and V matrices at each step. The mixed-canonical form of the MPS gives the Schmidt decomposition [143] of the state as

$$|\psi\rangle = \sum_{u_n} \Lambda^{[n]}_{u_n} |u_n\rangle_L |u_n\rangle_R \,, \tag{1.68}$$

where

$$|u_n\rangle_L = \sum_{i_1,\ldots,i_n} L^{[1]i_1} \ldots L^{[n]i_n} |i_1, \ldots, i_n\rangle \,, \tag{1.69}$$

$$|u_n\rangle_R = \sum_{i_{n+1},\ldots,i_N} R^{[n+1]i_{n+1}} \ldots R^{[N]i_N} |i_{n+1}, \ldots, i_N\rangle \,. \tag{1.70}$$

Let us again consider the general MPS formulation of the state as in Eq. (1.59). The set of N matrices $A^{[n]i_n}$ that we have obtained have dimensions $1 \times d$, $d \times d^2$, ..., $d^{N/2-1} \times d^{N/2}$, $d^{N/2} \times d^{N/2-1}$,...,$d^2 \times d$, $d \times 1$ respectively. The size of the representation of the state still scales exponentially in the system size because the bond dimension of the A matrices grows up to $d^{N/2-1} \times d^{N/2}$. This MPS representation, although exact, does not bring any computational advantage compared to the exact representation of Eq. (1.58). This problem is solved through the *compression* of the MPS which is performed by limiting the bond dimension of the A matrices to a fixed value χ. The compression of MPS is based on the properties of the SVD. The optimal approximation of a matrix M of Schmidt rank k with a matrix $\tilde{M}$ of Schmidt rank $\tilde{k}$, with respect to the Frobenius norm $||M||^2 = \sum_{ij} |M_{ij}|^2$, is given by

$$\tilde{M} = U\tilde{S}V^\dagger \quad \text{with} \quad \tilde{S} = diag(s_1, s_2, \ldots, s_{\tilde{k}}, 0, \ldots, 0) \,. \tag{1.71}$$

The optimal approximation is obtained by taking the $\tilde{k}$ largest singular values of M and setting the other ones to zero [11]. We approximate a state $|\psi\rangle$ written as MPS having bond dimension χ with a new state $|\psi'\rangle$ with maximal bond dimension χ' through an iterative procedure. Let us consider a state $|\psi\rangle$ written in the mixed-canonical form of Eq. (1.67), where $\Lambda^{[n]}$ is diagonal with χ elements and has Schmidt decomposition as in Eq. (1.68). The best approximation of $|\psi\rangle$ is obtained by keeping only the χ' largest elements of $\Lambda^{[n]}$. This step compresses the matrix size at only one site. However, it can be iteratively performed at each site, starting from a

completely left or right-normalised state by consecutively applying a set of SVDs and appropriately truncating them. This procedure is not optimal because it depends on the order in which the compression is performed, and on the fact that each step is affected by the previous one. An optimal compression procedure exists, and consists of variationally minimising the norm $||\psi\rangle - |\psi'\rangle|$ with respect to the A matrices that make up $|\psi'\rangle$. This is, however, a complex optimisation problem and computationally expensive, so the iterative SVD application and truncation is usually preferred.

So far, we have described how to obtain the MPS form of a quantum state and how to approximate it using MPS with a fixed bond dimension. In the next section, we will explain why MPS are useful as a representation of ground-state wavefunctions.

1.3.3 MPS and entanglement

The concept of entanglement is closely related to the MPS formulation. MPS are an appropriate ansatz for the variational algorithm DMRG because ground states of 1D gapped local Hamiltonians are efficiently approximated with MPS. The bond dimension needed to represent their ground state to an arbitrary precision is finite even in the thermodynamic limit. This is a consequence of the *area law* [92, 139] in 1D, which states that, for one-dimensional gapped local Hamiltonians, the entanglement entropy of a bipartite system grows linearly with the size of the boundary between the two subsystems. For a 1D system, the boundary size is fixed and does not grow with the system size.

Knowing that a system obeys the area law significantly simplifies the problem of finding its ground state. We do not need to search the whole Hilbert space of the system, but only the subspace in which the entanglement entropy grows according to the area law. This corner of the Hilbert space is parametrised efficiently by matrix product states [11].

Let us describe the relation between the entanglement entropy of a bipartite sys-

tem and the amount captured by MPS. A state $|\psi\rangle$ defined on a system composed of two subsystems A and B is written as

$$|\psi\rangle = \sum_{ij} \Psi_{ij} \, |i\rangle_A \, |j\rangle_B \ , \tag{1.72}$$

where $|i\rangle_A$ and $|j\rangle_B$ are orthonormal bases on A and B respectively. The corresponding density matrices for the two subsystems read

$$\rho_A = \Psi\Psi^\dagger \quad \text{and} \quad \rho_B = \Psi^\dagger\Psi \, . \tag{1.73}$$

By performing an SVD on Ψ we write $|\psi\rangle$ as

$$|\psi\rangle = \sum_{u=1}^{n} s_u \, |u\rangle_A \, |u\rangle_B \ , \tag{1.74}$$

where $|u\rangle_A$ and $|u\rangle_B$ are orthonormal bases on A and B respectively and u runs over the n non-zero singular values of Ψ. For $n = 1$ the state is a product state and for $n > 1$ it is entangled. Using the results of the SVD, the reduced density matrices for the two subsystems take on a convenient form

$$\rho_A = \sum_{u=1}^{n} s_u^2 \, |u\rangle_A \, \langle u|_A \quad \text{and} \quad \rho_B = \sum_{u=1}^{n} s_u^2 \, |u\rangle_B \, \langle u|_B \ . \tag{1.75}$$

The reduced density matrices share the same eigenvalues, equal to the square of the singular values. From this expression of the density matrices, the von Neumann entanglement entropy reads

$$S(|\psi\rangle) = -\mathrm{Tr}\left[\rho_A \log \rho_A\right] = -\sum_{u=1}^{n} s_u^2 \log s_u^2 \, . \tag{1.76}$$

This expression shows that $S(|\psi\rangle)$ is upper-bounded. It reaches its maximum value

when all of the s_u^2 are equal and the entanglement entropy is bounded by

$$S(|\psi\rangle) \leq -\sum_{u=1}^{n} \frac{1}{n} \log \frac{1}{n} = \log n \,. \tag{1.77}$$

The upper bound of the entanglement entropy grows logarithmically with the Schmidt rank n of the density matrix. In a MPS with bond dimension χ, the maximum number of non-zero singular values of the density matrix is χ. Therefore, such an MPS captures, at most, an amount of entanglement entropy $S = \log \chi$. This could appear as a limitation of MPS because they capture a finite amount of entanglement. However, it was shown that MPS are the correct description for ground states of local gapped Hamiltonians in 1D that obey the area law [139, 144].

1.3.4 Matrix product operators

Matrix product operators (MPO) are the extension of the MPS formulation of wavefunctions to operators. A general operator O that acts on a 1D lattice with N sites is written as

$$\hat{O} = \sum_{\substack{i_1,\ldots,i_N=0 \\ i'_1,\ldots,i'_N=0}}^{d} c_{i_1,\ldots,i_N,i'_1,\ldots,i'_N} \left|i_1,\ldots,i_N\right\rangle \left\langle i'_1,\ldots,i'_N\right| \,, \tag{1.78}$$

where $c_{i_1,\ldots,i_N,i'_1,\ldots,i'_N}$ is a set of d^{2N} coefficients and $|i_n\rangle$ are the local states at site n. Analogously to the MPS procedure, the set of coefficients $c_{i_1,\ldots,i_N,i'_1,\ldots,i'_N}$ can be formally turned into a product of matrices by a set of consecutive SVDs to obtain the operator in the MPO form as

$$\hat{O} = \sum_{\substack{i_1,\ldots,i_N \\ i'_1,\ldots,i'_N}} v_L M^{[1]i_1 i'_1} M^{[2]i_2 i'_2} \ldots M^{[N]i_N i'_N} v_R \left|i_1,\ldots,i_N\right\rangle \left\langle i'_1,\ldots,i'_N\right| \,, \tag{1.79}$$

where $M^{[n]i_n i'_n}$ is one of d^2 matrices, labelled by $i_n i'_n$, having dimensions $D \times D$ and v_L and v_R are $1 \times D$ and $D \times 1$ vectors respectively. We use D as the bond dimension

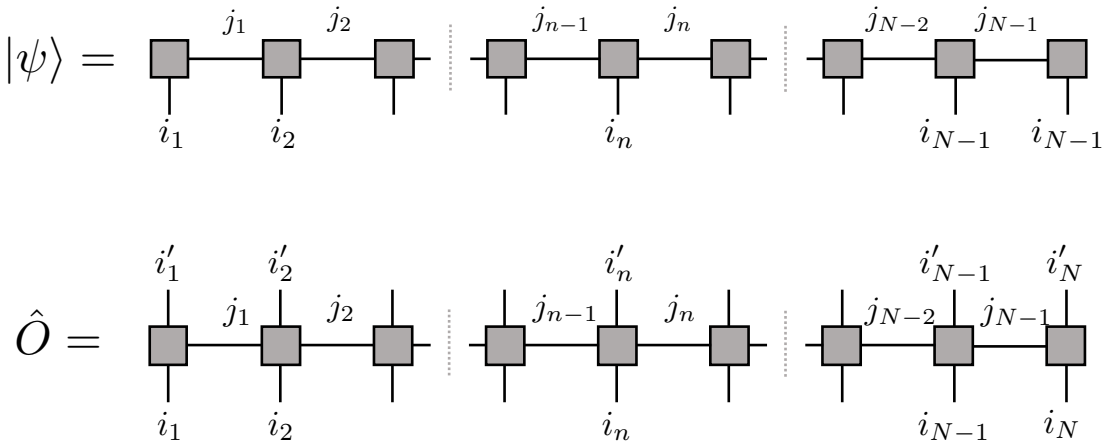


Figure 1.5: Pictorial representation for the MPS $|\psi\rangle$ and for the MPO $\hat{O}$.

for an MPO.

A comprehensive description of MPO and how to construct them, without resorting to the explicit use of consecutive SVDs, which can be computationally unwieldy, will be given in Chapter 2.

1.3.5 Pictorial representation

MPS and MPO are conveniently represented in a pictorial way, which makes operations involving them intuitive by avoiding explicit matrix multiplications.

A tensor of rank n is represented as a square with n outgoing legs, and connecting legs between squares represent tensor contractions. MPS are composed of a set of tensors which are represented as a chain of squares with three outgoing legs each: the two horizontal legs represent the virtual indices used for matrix multiplication, whereas the vertical one represents the physical index corresponding to the local Hilbert space. Fig. 1.5 shows the pictorial representation for the MPS of a state $|\psi\rangle$. The tensors that constitute an MPO are represented as squares with four outgoing legs. The two horizontal legs are the matrix multiplication indices, and the two

vertical legs represent the indices of the local Hilbert space. Fig. 1.5 shows the MPO pictorial representation of an operator $\hat{O}$.

Let us describe the main operations between MPS and MPO using the pictorial representation. The overlap $\langle\phi|\,\psi\rangle$ of two wavefunctions $|\psi\rangle$ and $|\phi\rangle$ is obtained by contracting the open legs of both MPS. The corresponding pictorial representation is shown in Fig. 1.6 (we use the convention where upward-pointing legs of an MPS matrix represent the Hermitian conjugate of the tensors). The absence of open legs in the final contracted object implies that the result is a tensor of rank 0 and therefore a scalar, as expected for the overlap of two wavefunctions. The overlap of two MPS $\langle\phi|\,\psi\rangle$ is written explicitly as

$$\langle\phi|\,\psi\rangle = \sum_{i_1,\ldots,i_N} B^{[1]i_1 *} B^{[2]i_2 *} \ldots B^{[N]i_N *} A^{[1]i_1} A^{[2]i_2} \ldots A^{[N]i_N}\,, \tag{1.80}$$

where $|\psi\rangle$ consists of the set of matrices A^n and $\langle\phi|$ consists of the set of matrices B^{n*}. The application of an MPO $\hat{O}$ to an MPS $|\psi\rangle$ leads to another MPS: $|\psi'\rangle = \hat{O}\,|\psi\rangle$. This is seen by contracting the physical indices of the corresponding MPO and MPS. The result is a tensor with a single physical leg per site which is therefore an MPS. Using the matrix notation, $\hat{O}\,|\psi\rangle$ is written as

$$\hat{O}\,|\psi\rangle = \sum_{\substack{i_1,\ldots,i_N \\ i'_1,\ldots,i'_N}} \left(M^{[1]i_1 i'_1} M^{[2]i_2 i'_2} \ldots M^{[N]i_N i'_N}\right) \left(A^{[1]i'_1} A^{[2]i'_2} \ldots A^{[N]i'_N}\right) |i_1,\ldots,i_N\rangle\,, \tag{1.81}$$

writing the matrix multiplication explicitly

$$= \sum_{\substack{i_1,\ldots,i_N \\ i'_1,\ldots,i'_N}} \sum_{\substack{j_1,\ldots,j_N \\ k_1,\ldots,k_N}} \left(M^{[1]i_1 i'_1}_{1,k_1} M^{[2]i_2 i'_2}_{k_1,k_2} \ldots M^{[N]i_N i'_N}_{k_{N-1},k_N}\right) \left(A^{[1]i'_1}_{1,j_1} A^{[2]i'_2}_{j_1,j_2} \ldots A^{[N]i'_N}_{j_{N-1},j_N}\right) |i_1,\ldots,i_N\rangle\,, \tag{1.82}$$

pairing matrices associated with the same site index

$$= \sum_{\substack{i_1,\ldots,i_N \\ i'_1,\ldots,i'_N}} \sum_{\substack{j_1,\ldots,j_N \\ k_1,\ldots,k_N}} \left(M^{[1]i_1 i'_1}_{1,k_1} A^{[1]i'_1}_{1,j_1} \right) \left(M^{[2]i_2 i'_2}_{k_1,k_2} A^{[2]i'_2}_{j_1,j_2} \right) \ldots \left(M^{[N]i_N i'_N}_{k_{N-1},k_N} A^{[N]i'_N}_{j_{N-1},j_N} \right) |i_1, \ldots, i_N\rangle \,, \tag{1.83}$$

renaming the terms in parenthesis

$$= \sum_{\substack{i_1,\ldots,i_N \\ i'_1,\ldots,i'_N}} \sum_{\substack{j_1,\ldots,j_N \\ k_1,\ldots,k_N}} B^{[1]i_1}_{(1,1),(k_1,j_1)} B^{[2]i_2}_{(k_1,j_1),(k_2,j_2)} \ldots B^{[N]i_N}_{(k_{N-1},j_{N-1}),(k_N,j_N)} |i_1, \ldots, i_N\rangle \,, \tag{1.84}$$

using matrix multiplication implicitly

$$= \sum_{i_1,\ldots,i_N} B^{[1]i_1} B^{[2]i_2} \ldots B^{[N]i_N} |i_1, \ldots, i_N\rangle \,, \tag{1.85}$$

where

$$B^{[n]i_n}_{(k_{n-1},j_{n-1}),(k_n,j_n)} = \sum_{i'_1,\ldots,i'_N} M^{[n]i_n i'_n}_{k_{n-1},k_n} A^{[n]i'_n}_{j_{n-1},j_n} \,. \tag{1.86}$$

The result is an MPS that consists of matrices whose bond dimensions are the product of the dimensions of those of the original MPS and MPO. Thus, the application of an MPO to an MPS leads to a new MPS with a larger bond dimension but retaining the same MPS structure. The pictorial representation of this calculation is shown in Fig. 1.6. This example shows how the pictorial notation simplifies the tedious explicit tensor contraction procedure.

Lastly, we consider the calculation for the expectation value of an operator $\hat{O}$ with respect to the wavefunction $|\psi\rangle$. We do not perform the calculation in matrix notation as it is obtained by consecutively applying the previous two steps. The result of this operation is the scalar $\langle\psi| \hat{O} |\psi\rangle$. This result is understood from the contraction of both sets of physical indices of the MPO with those of the MPS and its Hermitian conjugate, and is shown in Fig. 1.6.

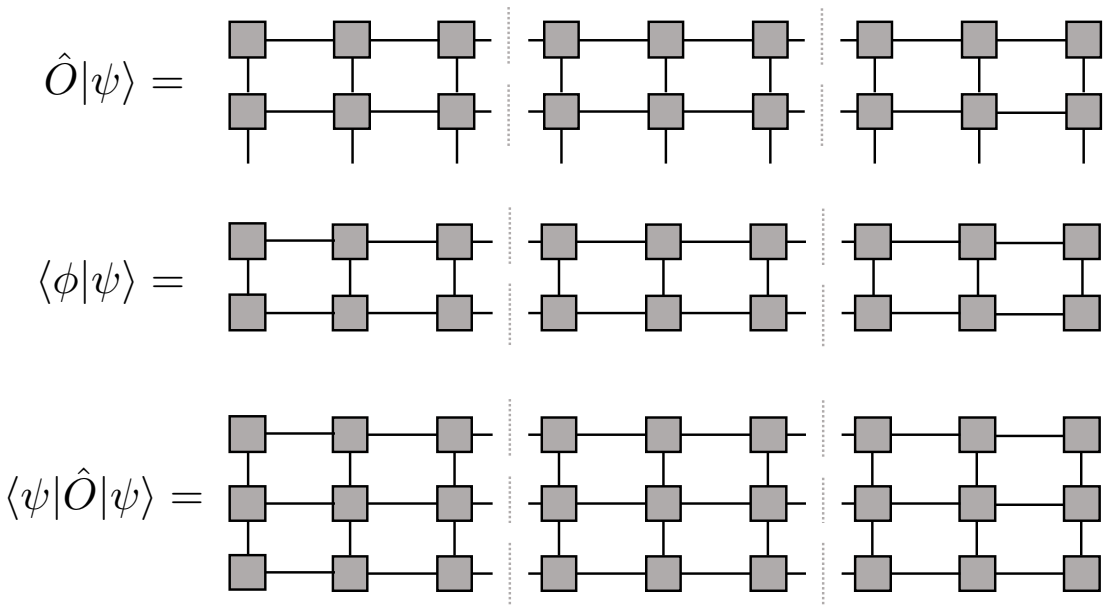


Figure 1.6: Pictorial representation for the multiplication of an MPO with an MPS: $\hat{O}\,|\psi\rangle$, for the overlap of two MPS: $\langle\phi|\,\psi\rangle$, and the expectation value of an MPO with reference to an MPS: $\langle\psi|\,\hat{O}\,|\psi\rangle$. The dotted lines indicate an arbitrary number of additional squares in between the ones shown.

1.3.6 Density matrix renormalisation group

In this section, we describe how the DMRG algorithm works and how it is implemented using the MPS and MPO formalism. DMRG is the numerical method that we will use throughout this thesis to calculate ground states.

The DMRG algorithm is a variational optimisation method used to find the ground state of a Hamiltonian H in the space of MPS with bond dimension χ. Although DMRG was originally conceived in terms of the reduced density operators of the system [5], it can be equivalently cast in the MPS language [11].

The goal of the algorithm is finding the ground state $|\psi\rangle$ of the system with Hamiltonian $\hat{H}$ by minimising its energy

$$E = \frac{\langle\psi|\,\hat{H}\,|\psi\rangle}{\langle\psi|\,\psi\rangle}\,. \tag{1.87}$$

This minimisation problem can be written using a Lagrange multiplier γ to consider the normalisation condition for the wavefunction and is equivalent to minimising

$$L = \langle\psi|\,\hat{H}\,|\psi\rangle - \gamma(\langle\psi|\,\psi\rangle - 1)\,. \tag{1.88}$$

When writing $|\psi\rangle$ in the MPS formalism, the minimisation of Eq. (1.87) becomes a highly nonlinear problem in the matrix elements of the MPS $A^{[n]i_n}_{j_{n-1},j_n}$. The DMRG algorithm turns this problem into a set of linear problems that can be numerically tackled. The idea behind the algorithm is to start with a guess for the initial MPS state, select a site in the lattice and the corresponding MPS tensor, and optimise this single tensor while keeping all of the other tensors of the MPS fixed. This is possible because, under these conditions, the minimisation problem becomes quadratic and can be solved. The outcome of this minimisation step leads to a new state with lower energy, although not the optimal one since only a single tensor was updated. Repeating this procedure throughout the whole lattice leads to a state with increasingly lower energy until the algorithm converges.

Let us evaluate the Lagrange multiplier problem of Eq. (1.88) in the MPS form. We consider a mixed canonical form of the MPS for $|\psi\rangle$, centred at site n as in Eq. (1.67). We will optimise the matrix at this site while keeping all of the other ones fixed. The overlap term $\langle\psi|\,\psi\rangle$ reads

$$\langle\psi|\,\psi\rangle = \sum_{i_n} F^{[n]i_n *} F^{[n]i_n}\,, \tag{1.89}$$

where $F^{[n]i_n} = L^{[n]i_n}\Lambda^{[n]}$. Calculating the minimum for the energy expectation value with respect to $F^{[n]i_n}$ and taking into account the Lagrange multiplier leads to the equation

$$\sum_{i'_1,\ldots,i'_N} E^{[n]}_L M^{[n]i_n,i'_n} E^{[n]}_R F^{[n]i'_n} - \lambda F^{[n]i'_n} = 0\,, \tag{1.90}$$

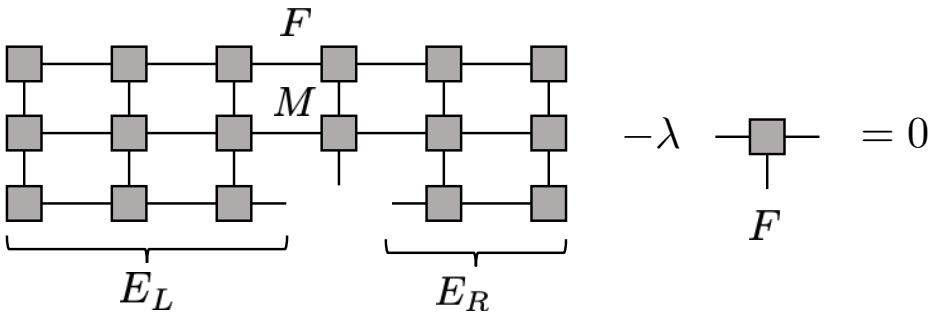


Figure 1.7: Pictorial representation of the eigenvalue problem in Eq. (1.90).

where $E_L^{[n]}$ and $E_R^{[n]}$ are the environments obtained by contracting all of the tensors to the left and right of those at site n respectively, as shown in Fig. 1.7. By defining $\tilde{H} = E_L M E_R$ and $x = F$ at site n, where the matrix F has been reshaped as a vector, Eq. (1.90) is written as the eigenvalue problem

$$\tilde{H}x = \lambda x \,, \tag{1.91}$$

where $\tilde{H}$ has dimensions $d\chi^2 \times d\chi^2$. A pictorial representation of the eigenvalue problem is shown in Fig. 1.7. In general, the size of the $\tilde{H}$ matrix is prohibitive to fully diagonalise. However, only the smallest eigenvalue is required, so it is sufficient to use an iterative eigenvalue solver such as the Lanczos method. The version of DMRG here described is the so-called single-site DMRG. Although it is easier to describe, it is prone to get stuck in local minima of the energy when searching for the ground-state MPS. Throughout the thesis, we will use an improvement to the algorithm, called two-site DMRG, in which two matrices of the MPS are optimised at the same time and which is better suited to finding the global minimum of the energy.

We have presented all of the ingredients necessary to describe the steps of the DMRG algorithm. We start by choosing an initial wavefunction, either at random or with an appropriate guess, written in the MPS form. Through a set of SVDs, we turn

it into the left-canonical form. We take the MPS in this form, the MPO representing the Hamiltonian and the Hermitian conjugate of the MPS and calculate all of the environments $E_R^{[n]}$ for each site. Next, we turn the MPS into a mixed-canonical form with centre at site 1 and solve the corresponding eigenvalue problem as in Eq. (1.91). After this, we calculate the left environment $E_L^{[1]}$ and move the centre of the mixed-canonical form to $n = 2$. This set of steps is repeated until the end of the lattice is reached. At this point, the same procedure is performed again but in the opposite direction, going from right to left. These are the so-called DMRG *sweeps*. We keep performing a sequence of left and right sweeps until the energy converges to a chosen accuracy. Given the variational nature of each step, the energy of the system is ensured to decrease at each sweep.

At this point, we have introduced all of the concepts underlying the numerical methods that we will develop and use in the following chapters. In Chapter 2, we will describe the development of the MPO that we have used to study 2D lattice systems in full detail.

Chapter 2

Development of 2D long-range interacting Hamiltonians for DMRG

A significant part of our efforts was devoted to the development of a general code aimed at performing calculations for 2D lattice systems with long-range interactions using the matrix product state (MPS) formalism, which we introduced in the previous chapter. The implementation of these numerical methods was realised using the TNT library [145], which provides highly optimised code for operating on tensors. At the time, however, the available routines in the library were limited to studying 1D lattices. Therefore, we have worked to overcome this limitation by creating a general matrix product operator (MPO) that can be used to simulate several 2D lattice systems. The library has since been updated to include projected entangled pair states (PEPS), which are a generalisation of MPS methods which naturally extend their formalism to study 2D models [146, 147].

This chapter comprehensively describes the steps we took to build the MPOs and is structured as follows. Section 2.1 describes the application of the density matrix renormalisation group (DMRG) algorithm to 2D systems. Section 2.2 describes how MPOs are built and introduces the concept of a finite-state automaton. Sections 2.3

and 2.4 explain in detail the process of building the MPO for the interacting Harper-Hofstadter model and the dipolar Bose-Hubbard model respectively.

2.1 2D density matrix renormalisation group

The physics of 2D systems is particularly exciting and significantly more diverse than 1D. However, it presents a challenge when treating the systems numerically, because the systems present strong quantum fluctuations and mean-field calculations are, in general, not effective. Moreover, due to the exponential growth of the Hilbert space with the system size, using exact diagonalisation (ED) quickly becomes prohibitive [6]. Quantum Monte Carlo simulations have proven to be a powerful method to study 2D systems [148, 149], however, they suffer from the sign problem for fermions and frustrated systems [150, 151].

Let us consider the use of DMRG to study 2D lattice systems. As a consequence of the area law in 1D, ground states of a local gapped Hamiltonian can be accurately described by an MPS with a fixed bond dimension [139]. This is because a subsystem is entangled with its environment only through its boundary. Local gapped phases in 2D also obey the area law, but in this case, the boundary size scales linearly with the system width and so will the entanglement entropy of the subsystem. As a consequence, the complexity of 2D DMRG calculations grows exponentially with the width of the system [152]. This appears to be a severe drawback. However, it is a definite improvement over ED. In ED, the complexity grows exponentially with the number of sites in the system, which is the product of both dimensions. Additionally, DMRG is not subject to the sign problem, and gives access to the full MPS form of the ground state. DMRG is, therefore, a promising method to treat 2D lattice systems.

2D lattice systems are studied with DMRG by mapping a 2D lattice to 1D. A 2D

lattice with L_x sites in the x direction and L_y sites in the y direction is converted into a 1D lattice with $L_x \times L_y$ sites. This comes at the cost of introducing long-range terms, which have as range the width of the system L_y, even when the original Hamiltonian had exclusively local terms. This gives a sense for where the complexity of the 2D DMRG calculations originates.

The boundary conditions imposed on the system play a significant role in determining the bond dimension χ necessary for the computations to converge to a specified accuracy. It is preferable to use open boundary conditions (OBC) or cylindrical boundary conditions. Fully periodic boundary conditions (PBC) in both dimensions, which translate to using a torus geometry, require a bond dimension χ^2 to obtain the same accuracy as the OBC case [11]. This can be intuitively understood as a consequence of the 2D-to-1D mapping. Whereas the distance between two neighbouring sites in 2D is at most L_y after the 2D-to-1D mapping with OBC, for fully PBC it can become $L_x \times L_y$. Therefore, it is computationally more expensive for DMRG to retain the same amount of entanglement between neighbouring sites when using PBC.

2.1.1 Tensor network methods

A set of generalisations of the MPS variational wavefunctions have been proposed to overcome the exponential scaling of the bond dimension necessary to treat 2D problems. These wavefunctions are called tensor network states [153] and can be divided into two main classes: projected entangled pair states (PEPS) [146, 147] and multi-scale entanglement renormalisation ansatz (MERA) [154, 155, 156, 157].

In 2D, PEPS are a network made of rank-5 tensors. They have the advantage of capturing the amount of entanglement needed by the area law in 2D, but they present two main drawbacks. Their optimisation algorithm to minimise the system energy scales very fast with their bond dimension and heavily depends on the algorithm chosen. For example, the 'full update' method scales with D^{10}, where D is the bond

dimension of the PEPS, and the 'simple update' method scales with D^5 [158]. Moreover, the exact computation of observables cannot be performed efficiently, therefore introducing approximations. However, they require much smaller bond dimensions to represent a 2D wavefunction as compared to MPS [159]. PEPS are also suited to work directly in the thermodynamic limit through the iPEPS method [160].

MERA are an extension of MPS where the tensors that make up the network have a layered structure. Every layer represents a coarser length scale for the normalisation group method [161, 162]. The optimisation method for MERA has an even higher optimisation cost as compared to PEPS but observables can be computed without approximation.

The very demanding scaling of the optimisation algorithms for PEPS and MERA are such that, for small 2D systems, DMRG is still competitive with them [163].

2.2 MPO construction

In the previous chapter, in Eq. (1.79) we introduced how an operator $\hat{O}$ is written in the MPO formalism

$$\hat{O} = \sum_{\substack{i_1,\ldots,i_N \\ i'_1,\ldots,i'_N}} v_L M^{[1]i_1 i'_1} M^{[2]i_2 i'_2} \ldots M^{[N]i_N i'_N} v_R \left|i_1,\ldots,i_N\right\rangle \left\langle i'_1,\ldots,i'_N\right| \ . \tag{2.1}$$

It is convenient to introduce a more compact notation to write the operator in the MPO form. Instead of explicitly separating the operator part of the MPO, represented by the ket-bra term in Eq. (2.1), from the coefficient term represented by the product of the M^i matrices, we consider the set of matrices M^i to have one-particle operators as matrix elements. Using this notation, the MPO is written as

$$\hat{O} = \sum_{j_0,\ldots,j_N} v_L M^1_{j_0 j_1} M^2_{j_1 j_2} \ldots M^N_{j_{N-1} j_N} v_R \ , \tag{2.2}$$

where the M^i are $D \times D$ matrices whose elements are one-particle operators acting on site i and the matrix multiplication has been written explicitly. From this point forward, will be using this notation.

Let us consider the problem of writing matrices M^i that make up the MPO form of an operator $\hat{O}$, without resorting to using a series of SVDs, which, for a general operator, can be computationally demanding. The MPO representation of local Hamiltonians with short-range terms has a small bond dimension D and is straightforward to obtain. As an example, let us consider the MPO matrices M^i for the homogeneous Heisenberg model in the presence of a uniform field on a 1D lattice. The Hamiltonian of the system reads

$$\hat{H} = \sum_i \left(J_x S_i^x S_{i+1}^x + J_y S_i^y S_{i+1}^y + J_z S_i^z S_{i+1}^z + \Delta S_i^z \right) , \tag{2.3}$$

where S_i^k for $k = x, y, z$ are the Pauli spin operators at site i. Since the system is translationally invariant, the M^i matrices of the MPO are not dependent on the lattice site i and read

$$M^i = \begin{pmatrix} 1 & J_x S^x & J_y S^y & J_z S^z & \Delta S^z \\ 0 & 0 & 0 & 0 & S^x \\ 0 & 0 & 0 & 0 & S^y \\ 0 & 0 & 0 & 0 & S^z \\ 0 & 0 & 0 & 0 & 1 \end{pmatrix} , \tag{2.4}$$

with

$$v_L = \begin{pmatrix} 1, & 0, & 0, & 0, & 0 \end{pmatrix} , \quad v_R = \begin{pmatrix} 0, & 0, & 0, & 0, & 1 \end{pmatrix}^T . \tag{2.5}$$

By explicitly multiplying the M^i matrices for each site i, all of the terms in the Hamiltonian in Eq. (2.3) are created. This Hamiltonian contains only on-site and nearest-neighbour terms and is represented exactly with an MPO having matrices

M^i with bond dimension $D = 5$.

As we have seen from this example, the MPO formulation is particularly efficient when representing Hamiltonians with only nearest-neighbour terms. However, it can also be used to describe more complex Hamiltonians. When only short-range terms are present, the bond dimension of the MPO is small, and the elements of the corresponding matrices are simple to derive. Long-range terms can still be represented by the MPO at the cost of increasing its bond dimension. However, depending on the type of Hamiltonian, it may no longer be straightforward to obtain the explicit form of the MPO matrices M^i. A more general method is necessary to solve this problem, and we will present it in the next section.

2.2.1 Finite-state automata method

Let us consider the MPO formulation of an operator presented in Eq. (2.2). We are interested in a technique that allows us to derive the elements of the matrices M^i starting from the Hamiltonian of the system. The transformation of the Hamiltonian to an MPO can be performed using the *finite-state automata* method [164].

A finite-state automaton can be thought of as a graph made of nodes and links between the nodes. A node is associated to each index a of the matrix element M^i_{ab}. Any two nodes, a and b, will have a link between them if the corresponding matrix element M^i_{ab} is non-zero. This matrix element represents the weight of the transition between nodes a and b. The set of all non-zero matrix elements creates a path between the starting and finishing nodes in the graph. This automaton is non-deterministic, meaning that each node can be connected with more than one other node, and that all of the different paths need to be taken in superposition. All of the terms of the Hamiltonian will be obtained by starting at the first node and, after i steps, placing the operator M^i_{ab} on site i. The whole Hamiltonian is built by following all of the paths that connect the starting node to the finishing node.

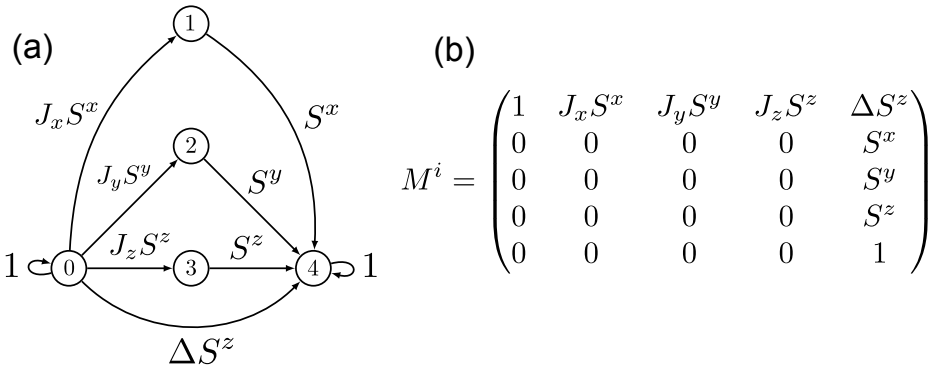


Figure 2.1: (a) Finite-state automaton for the homogeneous Heisenberg model and (b) the corresponding MPO matrix M^i.

2.2.1.1 Example: Heisenberg model

As an introduction to the method, let us consider as a textbook example the homogeneous Heisenberg Hamiltonian in Eq. (2.3), and derive its MPO formulation using a finite-state automaton. Fig. 2.1 shows the automaton and the corresponding MPO matrix M^i. The starting node is labelled with 0 and the finishing node with 4. The number of nodes in the automaton is equal to the bond dimension D of the MPO. Wherever two nodes are connected by a link, the corresponding matrix element of the MPO matrix M^i has a non-zero entry equal to the operator written on the link multiplied by the corresponding coefficient, e.g. $M_{01} = J_xS^x$. Going from the starting node 0 to the finishing node 4 through all possible paths generates all of the terms in the Hamiltonian. The matrix elements derived in this fashion are the ones written in the matrix M^i, as shown in Fig. 2.1 (b).

In the remaining part of the chapter, we will apply the finite-state automata method to build the MPO for the interacting Harper-Hofstadter model and the dipolar Bose-Hubbard model.

2.3 Interacting Harper-Hofstadter model

In the previous sections, we introduced the concept of a finite-state automaton and explained how it can be used to build the MPO form of a Hamiltonian. In this section, we will illustrate our application of this methodology to build the MPO for the Hamiltonian of the interacting Harper-Hofstadter (HH) model [135].

The system we consider is made of spinless particles on a square lattice with cylindrical boundary conditions. The particles hop through the lattice with nearest-neighbour (NN) hopping, interact with NN density-density interactions, on-site interactions, and are subject to a gauge field which represents an external magnetic field. We have constructed the MPO for both bosonic and fermionic particles so, for the sake of completeness, we will consider both in our explanation. However, the physical systems we will study throughout this thesis are composed of bosons. We will start our description for general spinless particles, and later in the chapter specialise it to both fermions and bosons. The main differences between the two types of system are their commutation relations and the type of interactions involved. For fermions, we consider only NN interactions since the Pauli exclusion principle suppresses multiple occupations of the same site. For bosons, we will consider only on-site interactions. The bosonic version of the model is appropriate to study the quantum Hall physics of ultracold atoms in optical lattices and we will use it in Chapter 3 to study bosonic quantum Hall ground states on a cylindrical lattice.

The Hamiltonian describing the system reads

$$H = -J \sum_{\langle i,j \rangle} \left(e^{i\phi_{ij}} c_i^\dagger c_j + \text{H.c.} \right) + V \sum_{\langle i,j \rangle} n_i n_j + U \sum_i n_i (n_i - 1) \,, \tag{2.6}$$

where c_i and $c_i^\dagger$ are the annihilation and creation operators for a particle at site i. J is the hopping amplitude, V is the NN interaction strength, U is the on-site interaction strength, $n_i = c_i^\dagger c_i$ is the number operator at site i, ϕ_{ij} is the phase acquired by a

particle hopping from site i to j due to the gauge field, and $\langle \ldots \rangle$ denotes NN pairs of sites. We have dropped the hat symbol to indicate operators since, from now on, we will be considering only operators in our description of MPOs. We will be considering 2D lattices with either open or cylindrical boundary conditions. Using a cylindrical geometry which has physical edges, gives us the possibility to study both bulk and edge properties of the system. This will be especially relevant for studying quantum Hall physics.

The system Hamiltonian in Eq. (2.6) is written using the indices i, which label the sites of the 2D lattice. To stress the two-dimensional nature of the system, it is more convenient to use a pair of indices (x, y) representing the x and y coordinates of the site with index i. We consider a square lattice with L_x sites in the x direction and L_y sites in the y direction, and PBC along y (for the cylinder geometry). H is written as the sum of a single-particle contribution H_0 and an interacting part H_1. The single-particle part of the Hamiltonian in Eq. (2.6), H_0 reads

$$H_0 = -J \left(\sum_{x=1}^{L_x-1} \sum_{y=1}^{L_y} c^\dagger_{x,y} c_{x+1,y} + \sum_{x=1}^{L_x} \sum_{y=1}^{L_y-1} e^{i2\pi\phi x} c^\dagger_{x,y} c_{x,y+1} + \sum_{x=1}^{L_x} e^{i2\pi\phi x} c^\dagger_{x,L_y} c_{x,1} \right) + \text{H.c.}\,, \tag{2.7}$$

where the complex phases have been written explicitly in the Landau gauge for a flux density per plaquette $n_\phi = \phi$. The interacting part of the Hamiltonian in Eq. (2.6), H_1 reads

$$\begin{aligned} H_1 =& V \left(\sum_{x=1}^{L_x-1} \sum_{y=1}^{L_y} n_{x,y} n_{x+1,y} + \sum_{x=1}^{L_x} \sum_{y=1}^{L_y-1} n_{x,y} n_{x,y+1} + \sum_{x=1}^{L_x} n_{x,L_y} n_{x,1} \right) \\ &+ U \sum_{x=1}^{L_x} \sum_{y=1}^{L_y} n_{x,y}(n_{x,y} - 1)\,. \end{aligned} \tag{2.8}$$

The Hamiltonians H_0 and H_1 present several types of terms, which need to be implemented in the MPO representation. In particular, there are site-dependent complex

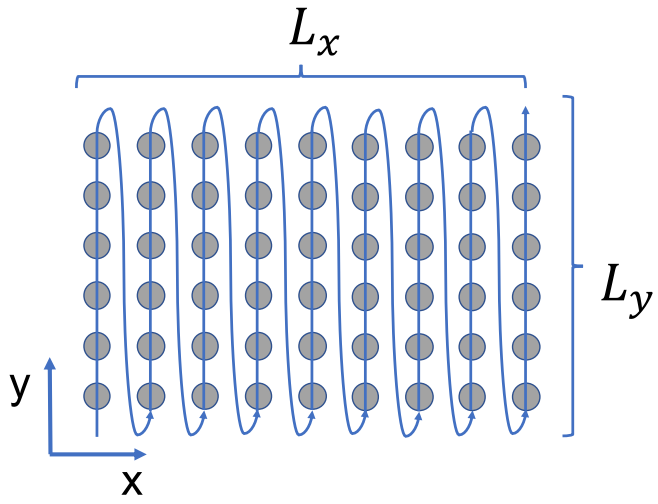


Figure 2.2: Mapping of the 2D lattice to 1D. The lattice has PBC in the y direction and a site with 2D coordinates (x, y) is mapped to 1D coordinate $(x-1)L_y + y$.

hoppings, NN interactions and terms that represent the periodic boundary conditions. All of these terms need specific attention when deriving the MPO matrices and we will consider them in the following sections.

2.3.1 2D-to-1D mapping

To obtain the MPO formulation of the Hamiltonian, we start by explicitly mapping the 2D lattice model to 1D. This is achieved by converting the pair of indices (x, y), representing the coordinates in the 2D lattice, to a new single index $(x-1)L_y+y$ representing the corresponding 1D lattice site. Fig. 2.2 shows how the 2D-to-1D mapping is performed. As a consequence of this mapping, short-range terms in 2D, such as the NN hopping and NN density-density interaction, become long-ranged in 1D, with range up to L_y. This is because neighbouring sites in 2D become L_y sites apart after the mapping to 1D. Throughout this chapter, we will need to simultaneously consider both the 2D nature of the physical system and the 1D structure of its mapping.

We will examine how all of the terms in the Hamiltonian and the geometry of the lattice affect the construction of the MPO matrices. We need to pay attention

to the effects of the gauge field, the 2D-to-1D mapping, and the cylindrical boundary conditions. All of these factors are connected and affect the structure of the MPO matrices.

2.3.2 Periodicity of the MPO matrices

The MPO form of the Hamiltonian on a 1D lattice with N sites, shown in Eq. (2.2), is made of N matrices M^i, one for each lattice site. However, depending on the Hamiltonian, these matrices need not all be different. For example, in a 1D translationally invariant system, like the homogeneous Heisenberg model described in Section 2.2.1.1, only one matrix M^i is sufficient to build the whole MPO. The number of different matrices necessary to represent the MPO over the entire lattice depends on the translational invariance properties of the Hamiltonian after the 2D-to-1D mapping. Although the Hamiltonian has specific translational invariance properties in 2D, they will be modified after the mapping to 1D.

For the interacting HH model that we are considering, a set of different matrices M^i is necessary to construct the MPO. Three sources break the translational invariance of the 1D-mapped system. The first source is the presence of the gauge field. The second source is the 2D-to-1D mapping, and the third is the presence of cylindrical boundary conditions.

We will consider how all of these factors affect the construction of the MPO, starting from the gauge field.

2.3.3 Effect of the gauge field

Even in the presence of a uniform magnetic field orthogonal to the lattice, the corresponding vector potential, which affects the Hamiltonian, is not uniform and modifies the translational invariance properties of the system. The complex phases that multiply the hopping terms in the Hamiltonian of Eq. (2.6) are a consequence of using the

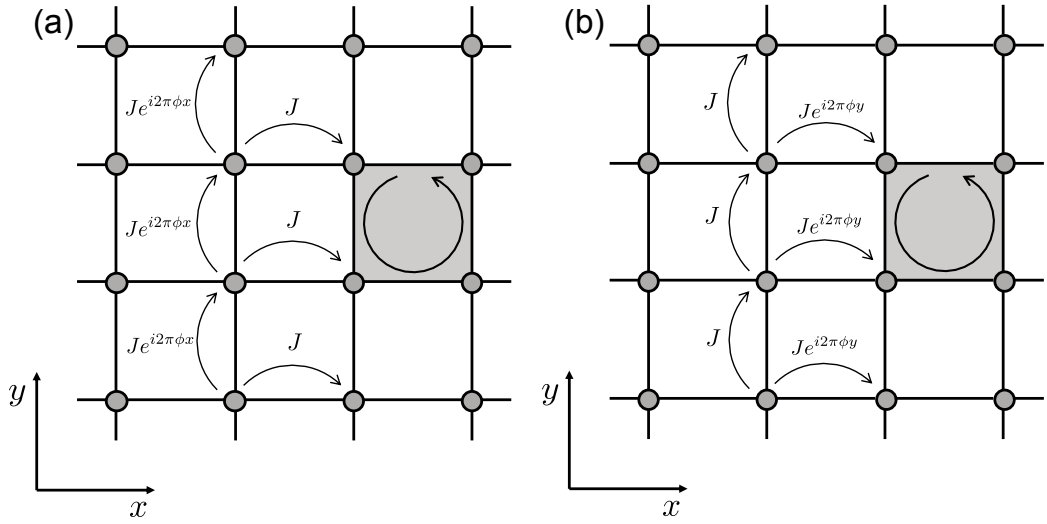


Figure 2.3: Two different versions of Landau gauge $\boldsymbol{A}_{\uparrow}$ (a) and $\boldsymbol{A}_{\rightarrow}$ (b) for a uniform magnetic field B and their effect on the complex hopping coefficients.

Peierls substitution when writing the Hamiltonian for a charged particle in a magnetic field $\mathbf{B} = \nabla \times \mathbf{A}$, where $\mathbf{A}$ is the vector potential. The complex phases are such that a particle moving around the lattice in a closed loop acquires a total phase equivalent to the Aharonov-Bohm phase which a charged particle would acquire in a magnetic field. Because of the gauge freedom in choosing the vector potential $\boldsymbol{A}$, the phases ϕ_{ij}, in Eq. (2.6) are not uniquely defined. In a square lattice geometry, it is convenient to use the Landau gauge, where both $\boldsymbol{A}$ and the phases ϕ_{ij} are non-zero only in one direction for a magnetic field $\boldsymbol{B} = (0, 0, B)$. The two choices of the Landau gauge for the vector potential $\boldsymbol{A}$ in 2D read

$$\boldsymbol{A}_{\uparrow} = (0, Bx, 0) \quad \text{and} \quad \boldsymbol{A}_{\rightarrow} = (-By, 0, 0)\,. \tag{2.9}$$

Fig. 2.3 shows how the choice of gauge affects the phases ϕ_{ij}. Choosing the Landau gauge $\boldsymbol{A}_{\uparrow}$, the hopping in the x direction is constant and real and reads J while the hopping in the y direction is x-dependent and reads $Je^{i2\pi\phi x}$. Choosing the Landau gauge $\boldsymbol{A}_{\rightarrow}$, the hopping in the x direction is y-dependent and reads $Je^{i2\pi y\phi}$ while the hopping in the y direction is constant and real and reads J. Both choices of gauge

are equivalent to having a magnetic flux density $n_\phi = \phi$ through each plaquette of the lattice in units of the magnetic flux quantum $\Phi_0 = h/2e$. The choice of either one of these gauges affects the x and y dimensions of the unit cell of the system and therefore modifies its translational invariance properties. For the gauge $\boldsymbol{A}_\uparrow$ the ϕ_{ij} are non-zero only in the y direction and when $\phi = p/q$, with p, q mutually prime integers, the 2D system has a q-site period along x and a 1-site period along y. For the gauge $\boldsymbol{A}_\rightarrow$, where the ϕ_{ij} are non-zero only in the x direction, the system has a 1-site period along x and a q-site period along y.

An additional consequence of the $\boldsymbol{A}_\rightarrow$ gauge is that the circumference L_y of the cylinder needs to be a multiple of q. This is necessary for the complex hopping to be compatible with the periodic boundary conditions.

Since the choice of gauge does not impact the expectation value of any observable, we can choose which gauge to use according to our needs. In our case, it is essential to recall that the complexity of DMRG calculations in 2D scales exponentially with the width of the system L_y. Thus, it is most convenient to use the $\boldsymbol{A}_\uparrow$ gauge as it does not impose any constraints on the values of L_y.

2.3.4 Effect of the 2D-to-1D mapping and boundary conditions

Let us consider the effect of the 2D-to-1D mapping and the use of the periodic boundary conditions along the y direction. It is useful to recall the intuitive meaning of the elements of the MPO matrices coming from the finite-state automata picture. The one-particle operator, which is the element M^i_{ab} of the tensor M^i at site i, needs to be inserted at the site i, depending on the appropriate set of operators that have been inserted before, in order to complete the terms appearing in the lattice Hamiltonian. The elements of M^i must depend on the position of site i relative to the sites coming before it in the 1D ordering. Because of the 2D-to-1D mapping, the set of L_y MPO

matrices M^i at a fixed x coordinate are not all equivalent and we can divide them into three groups according to their y coordinate. The *bottom* sites have $y = 1$, the *middle* sites have $1 < y < L_y$ and the *top* sites have $y = L_y$.

We need to be aware of this grouping to understand how to build the matrices of the MPO. The HH Hamiltonian involves four sets of terms. The first two are the NN hopping term and its Hermitian conjugate, the third one is the NN density-density interaction, and the fourth one is the on-site interaction. The first three involve NN terms while the last one is purely an on-site term.

Let us write these two different types of terms as the explicit tensor product of local operators acting at each lattice site i. The on-site interaction term at site i reads

$$n_i(n_i - 1) = 1_1 \otimes 1_2 \otimes \ldots \otimes 1_{i-1} \otimes n_i(n_i - 1) \otimes 1_{i+1} \otimes \ldots \otimes 1_{N-1} \otimes 1_N \,. \qquad (2.10)$$

The matrix elements M^i_{ab} are one-particle operators that need to be inserted at site i to generate all of the terms of the Hamiltonian through their consecutive multiplication. For the on-site interaction term, the one-particle operator needed is either the identity 1_i or the operator $n_i(n_i - 1)$. To create all of the terms of this type appearing in the Hamiltonian, a string of identity operators will be inserted until site i is reached. At that point, one interaction operator $n_i(n_i - 1)$ is added. Finally, another string of identities is inserted until the end of the lattice is reached. Because this type of operator is on-site, all of the sites in the lattice are equivalent and are treated in the same way.

Using the NN hopping as an example, the NN terms in the Hamiltonian take the form

$$c_i^\dagger c_j = 1_1 \otimes 1_2 \otimes \ldots \otimes 1_{i-1} \otimes c_i^\dagger \otimes 1_{i+1} \otimes \ldots \otimes 1_{j-1} \otimes c_j \otimes 1_{j+1} \otimes \ldots \otimes 1_{N-1} \otimes 1_N \,, \quad (2.11)$$

where $i < j$. Compared to the on-site terms, the construction of the NN terms is more complicated. There is going to be a string of identities followed by the first operator that makes up the NN term, then more identities until the second term is inserted. Finally, a string of identities is added until the end of the lattice is reached.

The distance between i and j depends on the relative position of site i with respect to the boundaries of the lattice as a consequence of the 2D-to-1D mapping. There are three relevant positions which we have previously defined as belonging to the bottom, middle and top groups. We will describe the finite-state automaton for each of the groups in the following sections.

2.3.4.1 Bottom terms

Let us start with a site at the bottom of the lattice, with coordinates $(x, 1)$ and analyse which terms of the Hamiltonian the corresponding MPO matrix needs to encode. This site has four neighbouring sites: $(x-1, 1)$, $(x+1, 1)$, $(x, 2)$, (x, L_y). Fig. 2.4 shows this configuration. Because of the 2D-to-1D mapping, an order relation exists between the lattice sites in 2D. Since we build the MPO using the finite-state automaton, the one-particle operator inserted at any site is only affected by the previous sites and not by the following sites. The 2D-to-1D mapping reads $(x, y) \to (x-1)L_y + y$ and turns the 2D coordinates (x, y) into a single number $(x-1)L_y + y$ that labels the lattice sites in 1D and explicitly defines an ordering of the sites in 1D. Site $(x, 1)$ has 1D index $(x-1)L_y + 1$ and its four neighbouring sites in the 2D lattice map to

$$(x-1, 1) \to (x-2)L_y + 1 \tag{2.12}$$

$$(x, 2) \to (x-1)L_y + 2 \tag{2.13}$$

$$(x, L_y) \to (x-1)L_y + L_y \tag{2.14}$$

$$(x+1, 1) \to xL_y + 1\,. \tag{2.15}$$

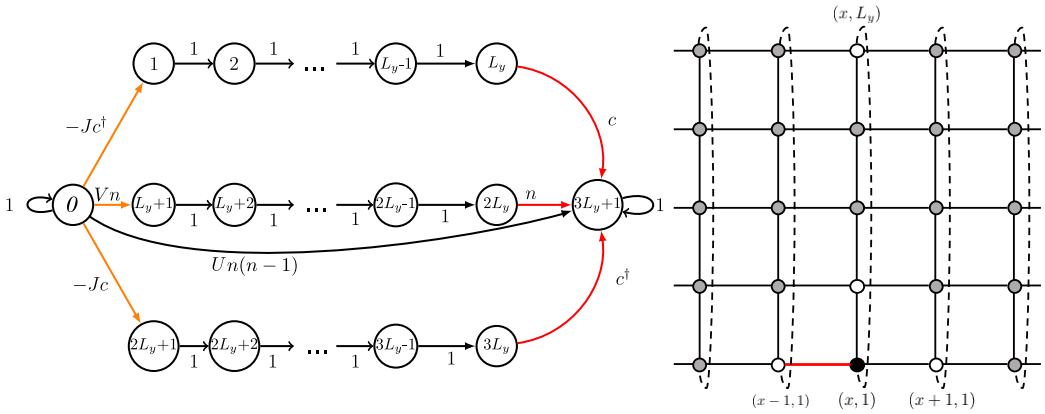


Figure 2.4: (Left) Finite-state automaton corresponding to one of the lattice sites at the bottom of the lattice with coordinates $(x, 1)$. (Right) Position of the bottom site in the 2D lattice in black and relevant NN term in red. The red link in the automaton corresponds to the insertion of the one-site operator that completes the NN term with the same colour in the lattice.

After the 1D mapping, only one of these four NN sites in 2D has a smaller index and therefore comes before site $(x, 1)$ in the 1D representation. This is the site with coordinates $(x-1, 1)$, and this pair of sites forms the NN term in the x direction starting at $(x-1, 1)$ and ending at $(x, 1)$. The MPO matrix M^i corresponding to the lattice site $(x, 1)$ has the purpose of completing only this hopping term. The other operators that need to be inserted at this site are those starting a NN term that ends on a successive lattice site or those adding an identity or a on-site interaction term.

Fig. 2.4 gives a graphical representation of the relevant terms on the lattice and the corresponding finite-state automaton. The site $(x, 1)$ is coloured black, and its four NN are coloured white. The only link with a NN term with a smaller index is the site $(x-1, 1)$, which is coloured red. Therefore, this is the only NN term that needs to be completed by the matrix element at that site. According to the 1D labelling, these sites are L_y sites apart, and the structure of the corresponding finite-state automaton needs to encode this information. The finite-state automaton will encode the insertion of the first term of the NN pair, then $L_y - 1$ identities followed by the operator that completes the NN term. The automaton has three branches for the three NN terms: the NN hopping and its Hermitian conjugate and the NN density-density interaction.

The on-site term is represented only by the link between the starting and finishing node.

2.3.4.2 Middle terms

In the same manner, let us consider a central site in the lattice with coordinates (x, y) and $1 < y < L_y$. This site has four neighbouring sites with coordinates: $(x-1, y)$, $(x+1, y)$, $(x, y+1)$, and $(x, y-1)$. The 1D labelling for site (x, y) becomes $(x-1)L_y+y$ and the four neighbouring sites map to

$$(x-1, y) \to (x-2)L_y + y \tag{2.16}$$

$$(x+1, y) \to xL_y + y \tag{2.17}$$

$$(x, y+1) \to (x-1)L_y + y + 1 \tag{2.18}$$

$$(x, y-1) \to (x-1)L_y + y - 1\,. \tag{2.19}$$

Only the sites at $(x-1, y)$ and $(x, y-1)$ come before site (x, y) in the 1D ordering so the MPO matrix M^i for this lattice site needs to complete the NN terms starting from both of these sites. Fig. 2.5 shows the corresponding finite-state automaton and the coloured lines in the lattice indicate the connections between sites which are considered in the automaton.

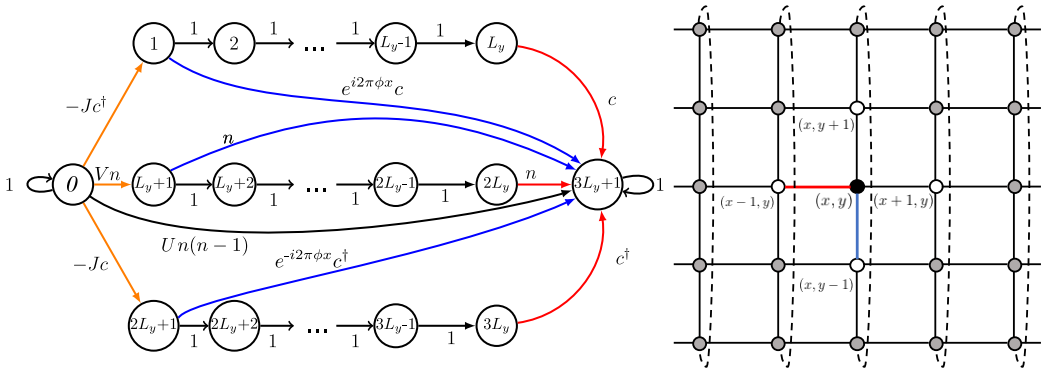


Figure 2.5: (Left) Finite-state automaton corresponding to one of the lattice sites at the centre of the lattice with coordinates (x, y) and $1 < y < L_y$. (Right) Position of the middle site in the 2D lattice in black and relevant NN terms in red and blue. The red and blue links in the automaton correspond to the insertion of the one-site operator that completes the NN term with the same colour in the lattice.

2.3.4.3 Top terms

Let us consider a site at the top of the 2D lattice with coordinates (x, L_y). This site has four neighbouring sites: $(x-1, L_y)$, $(x+1, L_y)$, (x, L_y-1), and $(x, 1)$. The 1D labelling for site (x, L_y) becomes $(x-1)L_y + L_y$ and the four neighbouring sites map to

$$(x-1, L_y) \to (x-2)L_y + L_y \tag{2.20}$$

$$(x, 1) \to (x-1)L_y + 1 \tag{2.21}$$

$$(x, L_y - 1) \to (x-1)L_y + L_y - 1 \tag{2.22}$$

$$(x+1, L_y) \to xL_y + L_y\,. \tag{2.23}$$

In this case, because of the mapping, the sites at $(x-1, L_y)$, (x, L_y-1) and $(x, 1)$ come before site (x, L_y) in the 1D ordering and the MPO matrix M^i at this lattice site needs to complete the NN terms starting from each of these sites. It is worth observing that this is the matrix which includes the term imposing the cylindrical PBC. This is a consequence of the mapping. Fig. 2.6 shows the finite-state automaton for this site and the coloured lines in the lattice highlight the corresponding terms.

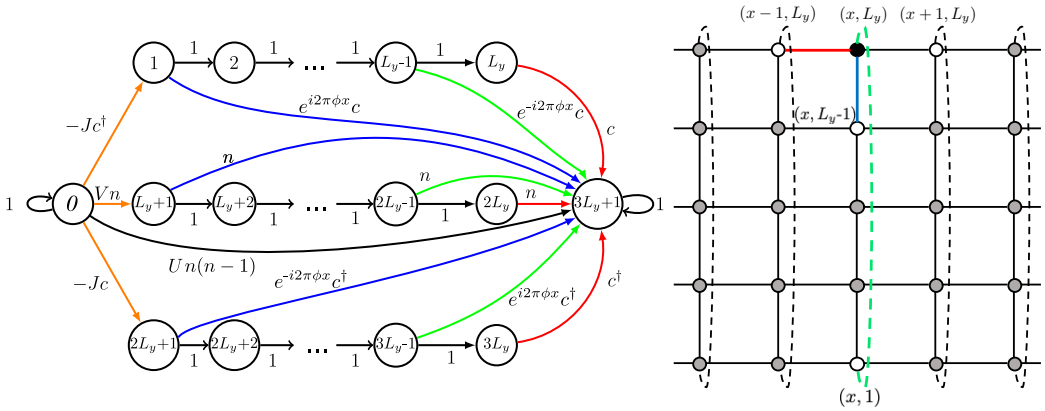


Figure 2.6: (Left) Finite-state automaton corresponding to one of the lattice sites at the top of the lattice with coordinates (x, L_y). (Right) Position of the top site in the 2D lattice in black and relevant NN terms in red, blue and green. The red, blue and green links in the automaton correspond to the insertion of the one-site operator that completes the NN term with the same colour in the lattice.

2.3.5 Additional consequences of the gauge field

So far we have considered how the finite-state automaton inserts the one-particle operators at each site to form all of the terms in the Hamiltonian. These one-particle operators need to be multiplied by the appropriate coefficients. The on-site interaction term $n_i(n_i - 1)$ is multiplied by U and the NN density-density interaction $n_i n_j$ term is multiplied by V, irrespective of the position of the sites. This is no longer the case for the coefficients of the NN hopping terms, which are site-dependent.

Let us consider the effect of the gauge field. As described in Section 2.3.3 the choice of gauge influences the periodicity of the 2D lattice in the x direction. Choosing the Landau gauge $\boldsymbol{A}_\uparrow$ leads to a q-site periodicity in x for the 2D Hamiltonian while choosing $\boldsymbol{A}_\rightarrow$ leads to a 1-site periodicity. We will analyse the case with $\boldsymbol{A}_\uparrow$ since the $\boldsymbol{A}_\rightarrow$ case can be seen as a sub-case of $\boldsymbol{A}_\uparrow$ where $q = 1$. In this gauge, the complex hoppings in the y direction are dependent on x. After the 2D-to-1D mapping, the q-site periodicity in the x direction is transformed into a $L_y \times q$ periodicity in 1D. The effect of the q-site periodicity of the system in the x direction is implemented by using site-dependent coefficients which multiply the operator that completes a NN

hopping term.

It is worth noticing that the phase of the coefficient that multiplies the term representing the hopping around the boundary conditions has the opposite sign compared to the terms that do not cross the boundary. This is a consequence of the ordering in which the terms are inserted by the MPO while creating the Hamiltonian. The complex phase $i2\pi\phi x$ corresponds to the NN term $c^{\dagger}_{x,L_y}c_{x,1}$. However, due to the mapping, the two terms are inserted in the opposite order. This is equivalent to inserting the Hermitian conjugate of the term, which requires using the complex conjugate of the coefficient.

2.3.6 Explicit form of the MPO matrices

At this point, we are equipped with all of the tools necessary to write the explicit form of the MPO matrices M^i. For each lattice site, we build the finite-state automaton that describes all of the terms that need to be inserted at that site. Starting from the automaton, we obtain the explicit form of the matrix elements M^i_{ab} through the procedure described in Section 2.2.1. As an example, the MPO matrix for a site i

corresponding to one of the top lattice sites from Section 2.3.4.3 reads $M^i =$

$$\left(\begin{array}{c|cccccc|cccccc|cccccc|c}
1 & -Jc^\dagger & 0 & 0 & \dots & 0 & -Jc & 0 & 0 & \dots & 0 & Vn & 0 & 0 & \dots & 0 & Un(n-1) \\
\hline
 & & 1 & & & & & & & & & & & & & & e^{i2\pi\phi x}c \\
 & & & 1 & & & & & & & & & & & & & 0 \\
 & & & & \ddots & & & & & & & & & & & & \vdots \\
 & & & & & 1 & & & & & & & & & & & e^{-i2\pi\phi x}c \\
 & & & & & & & & & & & & & & & & c \\
\hline
 & & & & & & & 1 & & & & & & & & & e^{-i2\pi\phi x}c^\dagger \\
 & & & & & & & & 1 & & & & & & & & 0 \\
 & & & & & & & & & \ddots & & & & & & & \vdots \\
 & & & & & & & & & & 1 & & & & & & e^{i2\pi\phi x}c^\dagger \\
 & & & & & & & & & & & & & & & & c^\dagger \\
\hline
 & & & & & & & & & & & 1 & & & & & n \\
 & & & & & & & & & & & & 1 & & & & 0 \\
 & & & & & & & & & & & & & \ddots & & & \vdots \\
 & & & & & & & & & & & & & & 1 & & n \\
 & & & & & & & & & & & & & & & & n \\
\hline
 & & & & & & & & & & & & & & & & 1
\end{array}\right),$$

where, for the sake of visual order, the empty terms in the matrix represent zeros. Each MPO matrix M^i has bond dimension $D = 3L_y + 2$, and a total of $q \times L_y$ distinct matrices are needed.

2.3.7 Bosonic and fermionic models

The previous analysis was carried out for spinless particles, without explicitly mentioning whether they were fermions or bosons. Let us describe what happens in each case.

2.3.7.1 Bosonic case

For the bosonic case, we consider the bosonic Harper-Hofstadter model with the addition of on-site interactions, so the NN interaction terms will not be present. As a consequence, we remove the L_y nodes that make up the central branch of the automaton in Fig. 2.6. Fig. 2.7 shows the finite-state automaton that generates the MPO matrix of the bosonic system for a site in the top group.

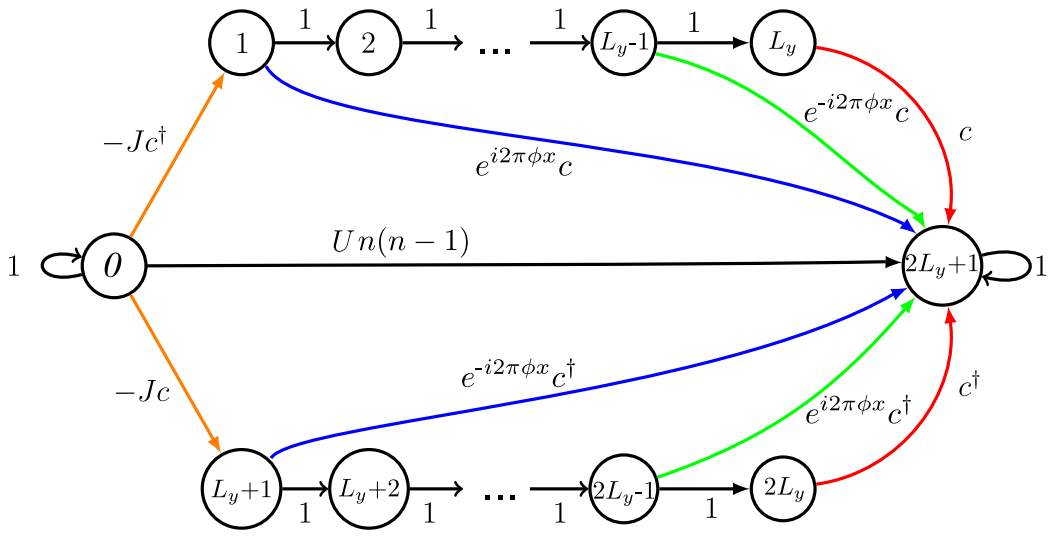


Figure 2.7: Finite-state automaton corresponding to all of the terms necessary to build the bosonic HH Hamiltonian.

The corresponding MPO matrix M^i reads

$$M^i = \left(\begin{array}{c|cccc|cccc|c} 1 & -Jc^\dagger & 0 & \cdots & 0 & -Jc & 0 & \cdots & 0 & Un(n-1) \\ & 1 & & & & & & & & e^{i2\pi\phi x}c \\ & & 1 & & & & & & & 0 \\ & & & \ddots & & & & & & \vdots \\ & & & & 1 & & & & & e^{-i2\pi\phi x}c \\ & & & & & & & & & c \\ \hline & & & & & 1 & & & & e^{-i2\pi\phi x}c^\dagger \\ & & & & & & 1 & & & 0 \\ & & & & & & & \ddots & & \vdots \\ & & & & & & & & 1 & e^{i2\pi\phi x}c^\dagger \\ & & & & & & & & & c^\dagger \\ \hline & & & & & & & & & 1 \end{array}\right).$$

Each MPO matrix M^i has bond dimension $D = 2L_y + 2$.

2.3.7.2 Fermionic case

Let us consider fermionic particles. We will include the NN interaction terms and the on-site interactions will be absent because they are suppressed by the Pauli exclusion principle. We need to take a more careful approach to generalise the methods we have developed so far. The standard procedure to treat spinless fermions in DMRG

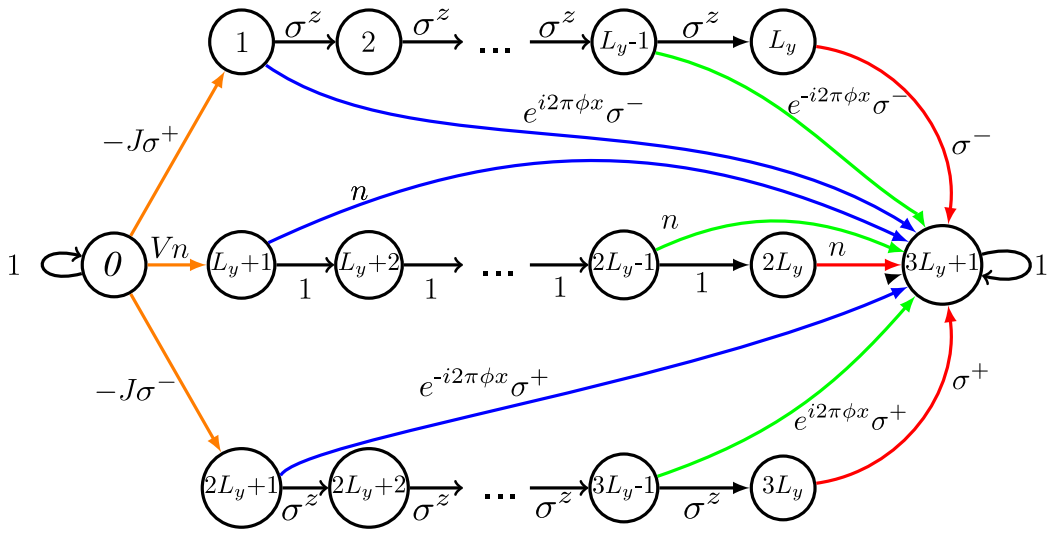


Figure 2.8: Finite-state automaton corresponding to all of the terms necessary to build the MPO of the fermionic Hamiltonian.

calculations is to map the fermionic operators c_i and $c_i^\dagger$ to spin 1/2 operators through the Jordan-Wigner transformation [165]. This transformation reads

$$c_i = \left(\prod_{j<i} \sigma_j^z\right) \sigma_i^- \quad \text{and} \quad c_i^\dagger = \left(\prod_{j<i} \sigma_j^z\right) \sigma_i^+ , \tag{2.24}$$

where σ^+, σ^- and σ^z are spin 1/2 operators. The effect of this transformation on the Hamiltonian is that of introducing a string of σ^z operators between the terms representing NN hopping terms. This string of operators will not be present between the NN density interaction terms because the string cancels out when computed for the number operators. Fig. 2.8 shows the finite-state automaton for the fermionic HH model. The corresponding MPO matrix M^i reads

$$M^i = \left(\begin{array}{c|cccccc|cccccc|cccccc|c}
1 & -J\sigma^+ & 0 & 0 & \dots & 0 & -J\sigma^- & 0 & 0 & \dots & 0 & Vn & 0 & 0 & \dots & 0 & 0 \\
\hline
 & \sigma^z & & & & & & & & & & & & & & & e^{i2\pi\phi x}\sigma^- \\
 & & \sigma^z & & & & & & & & & & & & & & 0 \\
 & & & \ddots & & & & & & & & & & & & & \vdots \\
 & & & & \sigma^z & & & & & & & & & & & & e^{-i2\pi\phi x}\sigma^- \\
 & & & & & & & & & & & & & & & & \sigma^- \\
\hline
 & & & & & & \sigma^z & & & & & & & & & & e^{-i2\pi\phi x}\sigma^+ \\
 & & & & & & & \sigma^z & & & & & & & & & 0 \\
 & & & & & & & & \ddots & & & & & & & & \vdots \\
 & & & & & & & & & \sigma^z & & & & & & & e^{i2\pi\phi x}\sigma^+ \\
 & & & & & & & & & & & & & & & & \sigma^+ \\
\hline
 & & & & & & & & & & & & 1 & & & & n \\
 & & & & & & & & & & & & & 1 & & & 0 \\
 & & & & & & & & & & & & & & \ddots & & \vdots \\
 & & & & & & & & & & & & & & & 1 & n \\
 & & & & & & & & & & & & & & & & n \\
\hline
 & & & & & & & & & & & & & & & & 1
\end{array}\right)$$

2.3.8 Extensions to long-range terms and other lattice geometries

The methods we have developed so far have focused on systems on a square lattice and with on-site or NN terms. However, they can be extended to treat different lattice geometries and longer-range terms. Once equipped with the long-range term toolbox, it is possible to convert the current model to another type of lattice such as triangular or honeycomb. We can imagine the honeycomb lattice, for example, as a square lattice with nearest-neighbour and next-nearest-neighbour terms, but where some of these terms are selectively suppressed. The toolbox of MPO methods we have created is therefore ready to be extended to new systems.

The next section will describe in detail how to implement the long-range interaction terms needed to study the dipolar Bose-Hubbard model.

2.4 Dipolar Bose-Hubbard model

We use the finite-state automata method to implement long-range interactions in a 2D lattice. We consider the dipolar Bose-Hubbard model, which has anisotropic interactions decaying with the cube of the distance between particles. We focus exclusively on the dipolar interactions and neglect the kinetic and on-site parts of the dipolar Bose-Hubbard Hamiltonian since the shorter-range terms have already been thoroughly described in the previous section. We will use the dipolar Bose-Hubbard model in Chapter 4 to study its ground states on a finite-size lattice.

For dipolar spinless bosons with polarised dipole moments, the long-range interacting part of the Hamiltonian reads

$$H_{dd} = \frac{1}{2} \sum_{i \neq j} V \frac{(1 - 3\cos^2\theta)}{|i-j|^3} n_i n_j \,, \tag{2.25}$$

where θ is the angle between the polarisation direction of the dipoles and the vector describing the relative position of coordinates i and j in the 2D lattice, and $V = D^2/a^3$ where D is the dipole moment and a is the lattice spacing. When the polarisation direction of the dipoles is orthogonal to the lattice ($\theta = \pi/2$), the interaction becomes isotropic with Hamiltonian

$$H_{dd} = \frac{1}{2} \sum_{i \neq j} \frac{V}{|i-j|^3} n_i n_j \,. \tag{2.26}$$

The dipolar interaction decays with a power law and has infinite range. However, we will cut off the interaction length at a fixed distance to limit the bond dimension of the MPO matrices.

The explicit form of the interaction terms as a tensor product of local operators

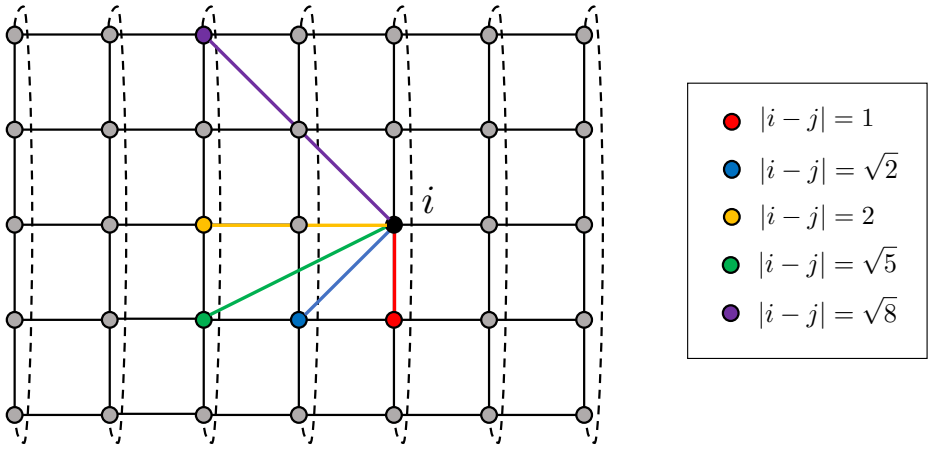


Figure 2.9: Long-range interacting terms considered in the MPO for the dipolar BH model. We perform a cutoff of the interaction at 5NN equivalent to $|i-j|=\sqrt{8}$. The sites are colour-coded according to their distance from the site at coordinates (x, y) labelled by the index i, coloured in black.

on each lattice site reads

$$n_i n_j = 1_1 \otimes 1_2 \otimes \ldots \otimes 1_{i-1} \otimes n_i \otimes 1_{i+1} \otimes \ldots \otimes 1_{j-1} \otimes n_j \otimes 1_{j+1} \otimes \ldots \otimes 1_{N-1} \otimes 1_N \,, \quad (2.27)$$

where $i < j$. A string of identity operators are inserted before, between and after the number operators n at sites i and j. We cut off the interaction terms in the 2D lattice at a distance $|i-j| = \sqrt{8}$, which means considering up to five nearest-neighbours (5NN) terms. Fig. 2.9 shows the square lattice and the interaction terms we are taking into account. As in the previous section, where only NN terms were present, the position of the sites with respect to the lattice affects the 2D-to-1D mapping and we need to consider its effect.

We are considering a significantly larger number of terms compared to the interacting Harper-Hofstadter model, making the mapping more complicated. In the next section, we will show how the translational invariance of the MPO is affected by the 2D-to-1D mapping and list the different terms that need to be taken into account.

2.4.1 Translational invariance

In order to determine how many different M^i matrices are necessary to build the MPO, we need to consider all of the possible sources affecting the translational invariance of the lattice after the 2D-to-1D mapping. For the current Hamiltonian, the translational invariance of the system is only changed through the 2D-to-1D mapping and the periodic boundary conditions. As a result, the matrices of the MPO describing the dipolar interaction are subject to a translational invariance of period L_y. The position of the lattice sites relative to the boundaries of the system in the y direction, and the cutoff of the interactions at 5NN lead to five inequivalent lattice site positions. A different matrix M^i will be needed for the MPO, corresponding to the coordinates (x, y) for the values of: $y = 1$, $y = 2$, $y = L_y - 1$, $y = L_y$ and for $2 < y < L_y - 2$. In the next sections, we will present the lattice configurations and the corresponding finite-state automaton for each of these cases.

2.4.1.1 Central term: $2 < y < L_y - 2$

Let us start with the terms corresponding to a site in a central position of the lattice with coordinates (x, y) and $2 < y < L_y - 2$. Due to the position of this site within the lattice and the cutoff of the interactions we have set, the longest-ranged term that needs to be implemented still falls within the boundaries of the lattice. Consequently, the periodic boundary conditions need not be taken into account explicitly. Fig. 2.10 shows the lattice sites that we need to consider, how far away they are from site (x, y), and how they are distributed around it. To build the finite-state automaton, let us repeat the type of reasoning we have followed in Section 2.3 but in a streamlined fashion, since we are already familiar with how it works.

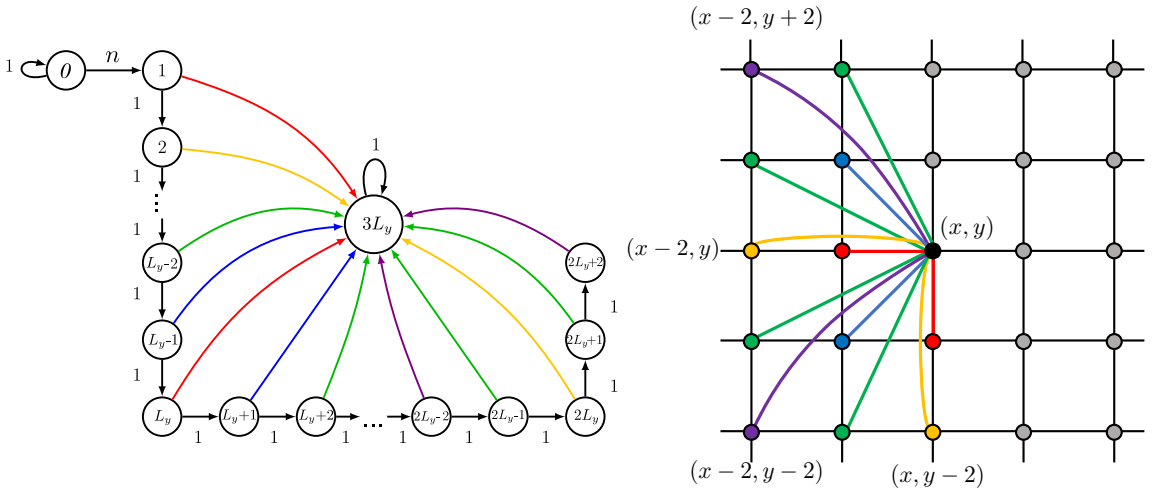


Figure 2.10: (Left) Finite-state automaton generating the matrix elements M_{ab} corresponding to a site located at coordinates (x, y) with $2 < y < L_y - 2$. (Right) Depiction of all of the long-range interacting terms implemented by the finite-state automaton. The links in the automaton are colour-coded according to the interaction term they implement.

Site (x, y) has 24 sites surrounding, which are within the 5NN cutoff we have imposed. However, for the purpose of building the MPO matrix, only the terms corresponding to sites coming before it in the 1D ordering need to be taken into account. There are 12 such sites which have a 1D distance from site (x, y) that goes from 1 to $2L_y + 2$, corresponding to the sites with 2D coordinates $(x, y-1)$ and $(x-2, y-2)$ respectively. The 1D distance is going to affect the number of nodes that make up the finite-state automaton and the corresponding MPO matrix. Fig. 2.10 shows the automaton that generates the MPO matrix. Let us describe it briefly. The starting and ending nodes of the automaton have labels 1 and $3L_y$ respectively, and they each have a self-pointing link corresponding to an identity operator. All of the other links ending at the node $3L_y$ have no explicit label for the sake of visual clarity, but they all represent the insertion of a density operator n. The links are colour-coded to encode the distance of the interaction term they represent. Each different colour corresponds to a different coefficient that multiplies the density operator and describes the power-law decay of the interaction. This colour-code is shown in Fig. 2.9.

In the next sections, we will show the lattice site configuration and the corresponding automaton for each site with inequivalent coordinates. For the sake of visual clarity, in all of the figures depicting the lattice, we will avoid drawing the links between the site of interest and all of the sites it is connected to. We will instead colour-code each site according to the scheme in Fig. 2.9, which uniquely identifies the strength of the interaction according to their distance. This simplification is necessary because all of the following cases contain interactions spanning through the PBC, which would become cumbersome to represent neatly. The horizontal dashed line cutting through the lattice symbolises an arbitrary number of additional lattice sites positioned in between.

2.4.1.2 Top term: $y = L_y$

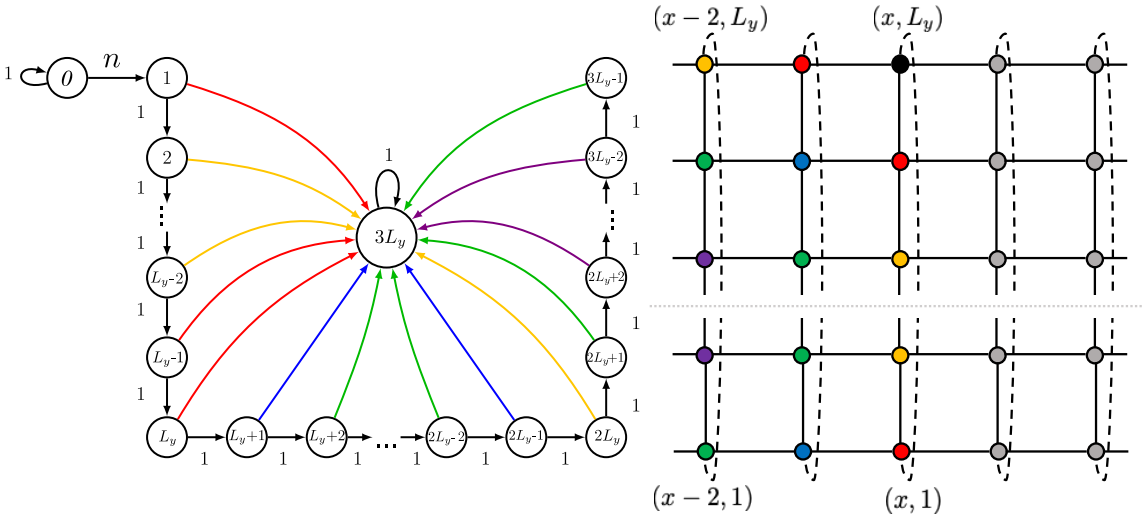


Figure 2.11: (Left) Finite-state automaton generating the matrix elements M_{ab} corresponding to a site located at coordinates (x, y) with $y = L_y$. (Right) Depiction of all of the long-range interacting terms implemented by the finite-state automaton. The links in the automaton are colour-coded according to the interaction term they implement.

2.4.1.3 Top term: $y = L_y - 1$

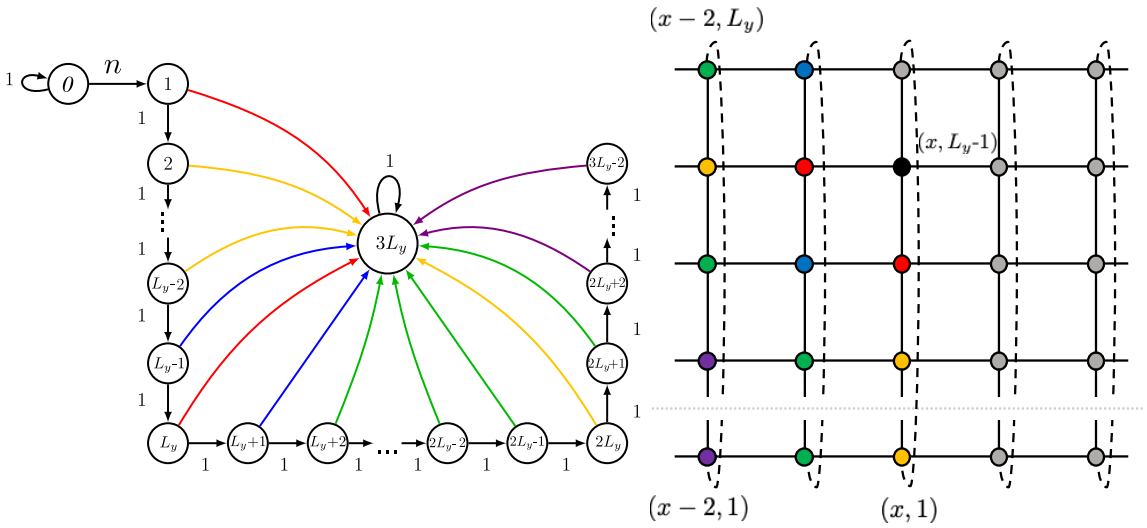


Figure 2.12: (Left) Finite-state automaton generating the matrix elements M_{ab} corresponding to a site located at coordinates (x, y) with $y = L_y - 1$. (Right) Depiction of all of the long-range interacting terms implemented by the finite-state automaton. The links in the automaton are colour-coded according to the interaction term they implement.

2.4.1.4 Bottom term: $y = 2$

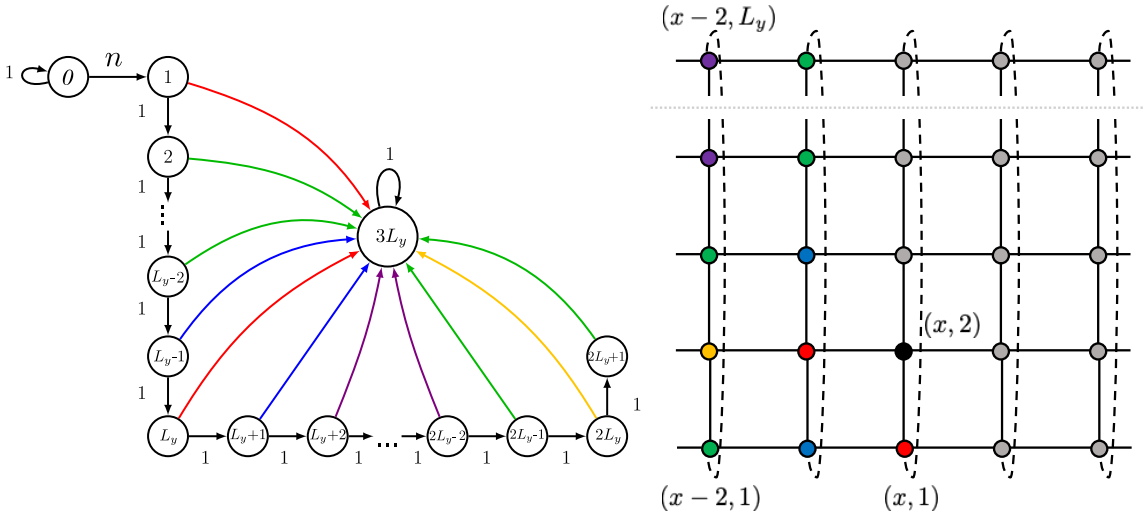


Figure 2.13: (Left) Finite-state automaton generating the matrix elements M_{ab} corresponding to a site located at coordinates (x, y) with $y = 2$. (Right) Depiction of all of the long-range interacting terms implemented by the finite-state automaton. The links in the automaton are colour-coded according to the interaction term they implement.

2.4.1.5 Bottom term: $y = 1$

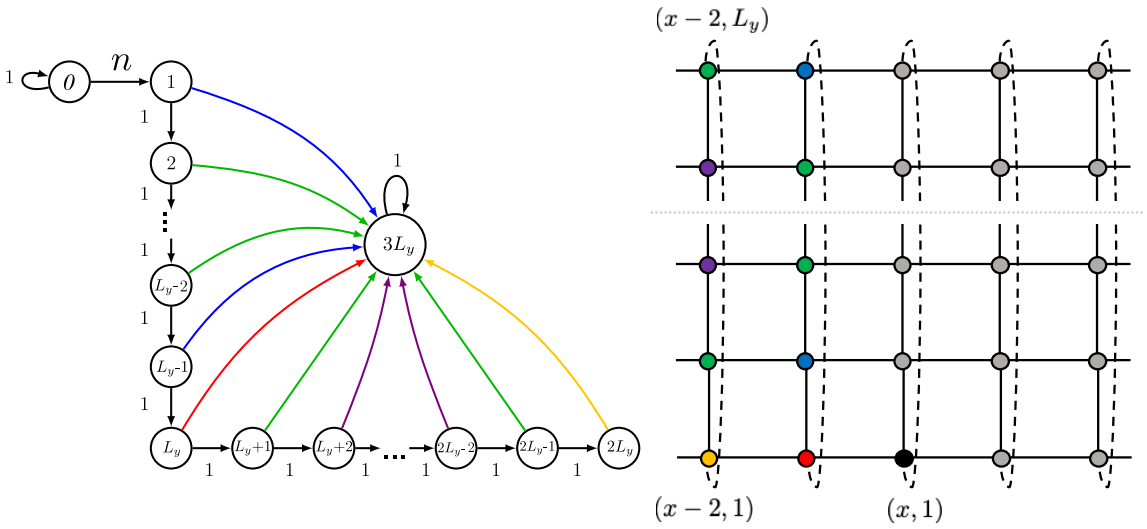


Figure 2.14: (Left) Finite-state automaton generating the matrix elements M_{ab} corresponding to a site located at coordinates (x, y) with $y = 1$. (Right) Depiction of all of the long-range interacting terms implemented by the finite-state automaton. The links in the automaton are colour-coded according to the interaction term they implement.

2.4.2 Dipolar interaction coefficients

In the definition of the MPO formalism for a general operator $\hat{O}$ as in Eq. (2.1), we have stated that the elements of each matrix M^i are one-particle operators which are multiplied by an appropriate coefficient. The finite-state automaton must encode both of these pieces of information: the operator and the coefficient. So far, we have described how the operator part is encoded in the finite-state automaton, glossing over the choice of coefficient, which has just been implicitly stated through the colour-coding of the sites. The structure of the graph that constitutes the automaton for each inequivalent lattice site is similar. This is because the terms composing the interaction span a similar range of distances when converted to the 1D lattice.

Let us consider the coefficients that multiply the one-particle operators. These coefficients have the form $V/|i - j|^3$, which describes the scaling of the interaction energy with the distance. The coefficients depend on the relative position of the

sites in the 2D lattice where the dipolar interaction actually exists, since they are a function of $|i-j|$. Because there are five inequivalent lattice positions in the 2D lattice, each of them needs to be treated differently. The relative position of sites i and j in 2D is described by the relative x coordinate Δx and by the relative y coordinate Δy. Because of the inequivalency of the sites in the lattice, pairs of sites that have the same 1D distance have different distances in 2D, depending on their position relative to the lattice boundaries in the y coordinate. Although the insertion of the operators is not changed, the calculation of the multiplicative coefficients that represent the power-law decay of the dipole interaction needs to be site-dependent. Two different factors need to be considered. The first is the fact that distances in 1D do not correspond to the same distance in 2D. As a simple example, let us consider the case of two lattice sites $(x, 2)$ and $(x, 1)$. These are NN sites in the 2D lattice, as well as after the 1D mapping. However, let us consider the sites $(x, 1)$ and $(x-1, L_y)$. They have distance $\sqrt{2}$ in the 2D lattice but have distance 1 in the 1D mapping. Secondly, the mapping of the distances from 1D to 2D is not unique. A separate mapping is necessary for each of the inequivalent lattice sites. For example, the terms which have a 2D-distance $\sqrt{8}$ have different distances in 1D according to their position. For a central site, the corresponding 1D distance is $2L_y - 2$ and $2L_y + 2$, but for a top site ($y = L_y$) the same 2D distances map to the 1D distances of $2L_y + 2$ and $3L_y - 2$. This fact needs to be included in each separate automaton that builds the MPO. Five different 1D-to-2D mappings to calculate Δx and Δy are used.

2.5 Testing, benchmarking and applications

We have thoroughly tested the implementation of the MPO for the interacting Harper-Hofstadter and dipolar Bose-Hubbard Hamiltonians by comparing the results obtained from DMRG with quantities known in the literature. We have reproduced the

correlation functions of a bosonic integer quantum Hall system on a square lattice from Ref. [124] and the currents for a fermionic fractional quantum Hall system on a cylindrical lattice from Ref. [166]. In addition, we have developed an exact diagonalisation code to compute the ground state of the bosonic Harper-Hofstadter model and the dipolar Bose-Hubbard model for small systems with size of up to $L_x \times L_y = 4 \times 5$ and up to 4 particles. We have confirmed the agreement between the energy and all of the expectation values used throughout our calculations between the DMRG code and the exact diagonalisation code.

The extensive development of the 2D lattice Hamiltonians that we have carried out using the TNT library has produced a powerful and general tool to explore 2D lattice systems. The types of particles that we can study are spinless fermions, spinless bosons and spins. We can define a general gauge field that affects the complex phase of the particle hoppings and add arbitrary on-site terms. We can add on-site interactions, NN, NNN etc. with site and range-dependent interaction strength. This is a general tool that allows us to study a variety of different physical systems.

In the next chapters, we will consider two systems. Chapter 3 will discuss the bosonic Harper-Hofstadter model and Chapter 4 will consider the dipolar Bose-Hubbard model.

Chapter 3

Bosonic fractional quantum Hall ground states on a finite cylinder

In this chapter, we make use of the 2D DMRG methods presented in Chapter 2 to study the ground-state properties of a bosonic Harper-Hofstadter (HH) model. With the addition of on-site interactions, this model describes the physics of a quantum Hall system in an optical lattice setting, using ultracold atoms [42, 114]. We will consider a finite cylindrical geometry and a filling fraction $\nu = 1/2$.

We perform our calculations on a finite cylinder geometry. The reason for the choice of a finite geometry is twofold. On the one hand, it gives access to the physical boundaries of the system which show relevant properties for a quantum Hall state. On the other hand, the experimental realisation of lattice systems is inherently finite, and edge effects will play a role. A finite cylinder will therefore exemplify the behaviour of an experimental setup. Moreover, a proposal has been put forward for the realisation of an experiment that implements a fermionic version of this system on a finite real-space cylindrical geometry [166]. This system is ideally suited to studying the edge modes of the system and has been shown to support fermionic fractional quantum Hall states [133, 166].

To characterise the ground state of the system, we compute a set of observables whose behaviour is known for a Laughlin state in the continuum in a finite geometry. A fractional quantum Hall state with a gapped, insulating bulk and gapless edge modes has been shown to have a uniform density in the bulk and a density spike near the edges in the continuum [167, 168]. Moreover, chiral edge currents [76, 169] and algebraically decaying one-particle correlation functions near the edge [123, 124] are typical of the state. Additionally, we make use of the topological entanglement entropy, which is known for the Laughlin state [89, 170, 171], to unambiguously characterise the topological nature of the state. We compute the zero-temperature ground states of systems with size, geometry and parameters which are in line with experimentally realisable systems and find that their ground states show a set of physical properties compatible with those of a Laughlin state in the continuum. Our results aim at providing guidance to experimentalists on how to observe fractional quantum Hall grounds states in optical lattices in the limit of large magnetic fluxes.

This chapter is structured as follows. In Section 3.1, we describe the interacting bosonic HH model. In Section 3.2, we calculate the topological entanglement entropy for our system. In Section 3.3 we compute a set of observables that characterise the edge and bulk properties of the state and in Section 3.4 we generalise the model outside of the hard-core limit. Finally in Section 3.5 we discuss and summarise our results.

The results presented in this chapter have been published in Ref. [61].

3.1 Bosonic Harper-Hofstadter model

We consider a bosonic HH model with the addition of on-site interactions. We have introduced this model in Section 2.3, so we will only recall the relevant information to describe our system. N_b spinless bosons live on a square lattice with L_x sites in

the x direction and L_y sites in the y direction, and mean particle density n_b. We impose periodic boundary conditions (PBC) in the y direction, turning the lattice into a finite cylinder geometry.

The Hamiltonian of the system reads

$$H = H_{\text{kin}} + H_U \,, \tag{3.1}$$

where H_{kin} is the single-particle kinetic Hamiltonian and H_U is the on-site interaction Hamiltonian. H_{kin} reads

$$H_{\text{kin}} = -J \left[\sum_{x=1}^{L_x-1} \sum_{y=1}^{L_y} c_{x,y}^\dagger c_{x+1,y} + \sum_{x=1}^{L_x} \sum_{y=1}^{L_y-1} e^{i2\pi x\phi} c_{x,y}^\dagger c_{x,y+1} + \sum_{x=1}^{L_x} e^{i2\pi x\phi} c_{x,L_y}^\dagger c_{x,1} \right] + \text{H.c.} \,, \tag{3.2}$$

where $c_{x,y}$ is the annihilation operator for a boson at site (x, y), obeying bosonic commutation relations $[c_i, c_j^\dagger] = \delta_{ij}$ and J is the hopping amplitude. The filling fraction of the system is defined as $\nu = n_b/n_\phi$, where $n_\phi \equiv \phi$ is the flux per plaquette.

The interacting part of the Hamiltonian H_U in Eq. (3.1) reads

$$H_U = U \sum_{x=1}^{L_x} \sum_{y=1}^{L_y} n_{x,y}(n_{x,y} - 1) \,, \tag{3.3}$$

where U is the on-site interaction strength and $n_{x,y} = c_{x,y}^\dagger c_{x,y}$ is the number operator at site (x, y). Since the system is made of bosons, each site can be occupied by at most N_b particles. However, in our numerical calculations using DMRG, we need to fix a maximum occupation number $n_{\max}$ at each site, to limit their computational complexity. This limits the dimension of the local Hilbert space on each site to $n_{\max}$.

Throughout this chapter, we will consider two interaction regimes. First, we will work in the hard-core limit, where $U/J \to \infty$. No two particles are allowed to be in the same lattice site, and the local Hilbert space at each site is constrained to have either zero or one particle. This implies that $n_{\max} = 1$ and the on-site interaction

term in the Hamiltonian of Eq. (3.1) can be omitted.

Later in the chapter, we will drop the hard-core constraint and consider general interaction strength U. In this case, we will choose $n_{\max}$ in such a way that our calculations converge.

3.2 Topological entanglement entropy

In order to investigate the topological nature of the system, we compute the topological entanglement entropy γ for its ground state. We use the scaling relation of the entanglement entropy with the length of the bipartition boundary [92, 172]

$$S(L) = cL - \gamma\,, \tag{3.4}$$

where L is the length of the boundary and c is a non-universal constant. Obtaining a non-zero value of γ indicates that the ground state of the system is topologically ordered and supports anyonic quasiparticle excitations. In order for Eq. (3.4) to hold, it is necessary that only Abelian anyons be present in the system, and that the degenerate ground states are in a proper linear superposition such that their entanglement entropy is minimal, called minimally entangled states [173]. We assume these conditions to hold and that the ground states we obtain are in the minimally entangled basis as a result of DMRG selecting low entanglement states [174].

We perform the bipartition of the cylinder by cutting it in two equal parts along the y direction. Each half-cylinder has size $L_x/2 \times L_y$. We consider the ground state for filling fraction $\nu = 1/2$ and $\phi = 1/6$. We fix $L_x = 6$ and scale the cylinder circumference L_y, which is the length of the boundary L that appears in Eq. (3.4). Since the complexity of the DMRG calculation already scales exponentially with the circumference of the lattice, we choose L_x to be a small number to limit the computational cost. The values of L_y are constrained to be even, to ensure that the

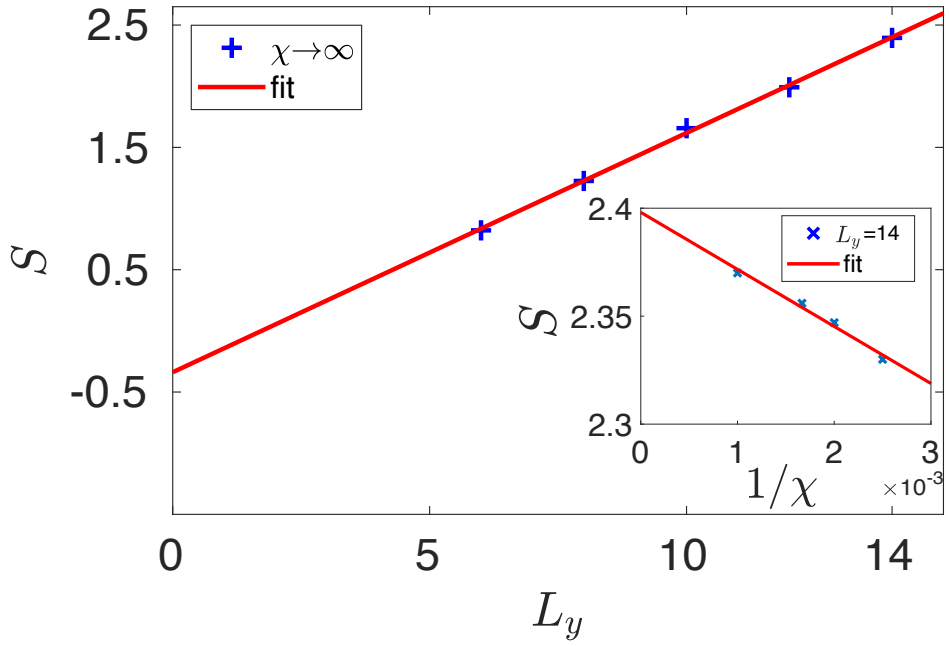


Figure 3.1: Entanglement entropy S for a cylinder of length $L_x = 6$, filling fraction $\nu = 1/2$ and $\phi = 1/6$ as a function of circumference L_y. The blue crosses are the results of an extrapolation of S to $\chi \to \infty$, and the red solid line is the linear fit to these values. The inset shows the linear fit of S as a function of $1/\chi$ for $L_y = 14$.

total number of particles in the system is an integer. For each size, we always obtain two degenerate ground states. We selectively obtain either of the two ground states by changing the starting wavefunction for DMRG. This two-fold degeneracy is typical of topologically ordered systems and consistent with the centre-of-mass degeneracy of the corresponding system on a torus, which has been shown to be size-dependent [175].

For each system size, we compute the entanglement entropy S from the MPS formulation of the ground-state wavefunction. The MPS gives direct access to the Schmidt values λ_i for the bipartition of the system, which we use to compute S as

$$S = -\mathrm{tr}[\rho_L \ln(\rho_L)] = -\sum_i |\lambda_i|^2 \ln(|\lambda_i|^2)\,, \tag{3.5}$$

where ρ_L is the density matrix of the left part of the system after a performing the bipartition cut.

Having $S(L_y)$ for each value of L_y allows us to derive the value of the topological entanglement entropy as in Eq. (3.4). For each value of L_y we perform a finite entanglement scaling by considering increasing bond dimensions $\chi = 400, 500, 600, 1000$. We perform a linear fit of $S_\chi(L_y)$ as a function of $1/\chi$ and extrapolate the value of $S_\infty(L_y)$ for $\chi \to \infty$. We use these values $S_\infty(L_y)$ to calculate γ

$$\gamma \approx 0.34 \pm 0.05\,, \tag{3.6}$$

where the error is for the 68% confidence interval of the result of the linear fit, shown in Fig. 3.1.

The non-zero value of the topological entanglement entropy indicates that the ground state of the system is topologically ordered. Analytical results for the topological entanglement entropy of a Laughlin state with filling fraction $\nu = 1/q$ give $\gamma = \ln\sqrt{q}$ [170, 171]. The value of γ we obtain is in close agreement with the analytical result $\gamma = \ln\sqrt{2} \approx 0.347$.

3.3 Quantum Hall signatures

To compare how accurately the ground-state properties of the system are compatible with those of a Laughlin state, we calculate a set of observables whose behaviour is known in the continuum version of the system, where the ground state is described by the Laughlin wavefunction. The observables we consider are the particle density, the currents and the correlation functions around the cylinder.

We consider the bosonic HH Hamiltonian on a finite cylinder and in the hard-core limit for filling fraction $\nu = 1/2$ and $\phi = 1/3$. The results coming from ED of small systems [41, 42, 44] show that the overlap of the ground state with the Laughlin

wavefunction is small, for large values of the magnetic flux $\phi > 0.2$. Selecting $\phi = 1/3$ is, therefore, a relevant parameter to choose in order to characterise the ground state by going beyond the calculation of the overlap. Previous works have gone beyond the overlap calculations by computing the Chern number [42] and considering the pumping of charges through an infinite cylinder using DMRG [135].

We instead choose to use a finite cylinder geometry which gives access to the edge properties of the system, which are especially relevant for quantum Hall physics, and are not available in the torus or infinite cylinder geometry. We consider a system with circumference $L_y = 6$ and increasing cylinder lengths from $L_x = 9$ up to $L_x = 18$, to see how the system length affects the edge properties of the system. These system sizes always lead to non-degenerate ground states, in agreement with the degeneracy of the system on a torus geometry, where a unique ground state is found for appropriate values of L_x and L_y [175]. For all of the system sizes that we have considered, we obtain a non-degenerate ground state in the corresponding cylinder geometry. All calculations have been performed with bond dimension $\chi = 1000$, which is sufficient to obtain converged expectation values for all of our quantities of interest. We also fix the total number of particles in the system by imposing $U(1)$ quantum number conservation symmetry [11].

3.3.1 Particle density

Let us consider the local density profile of the ground state, defined as the expectation value of the number operator at each site, which reads

$$n(x) = \frac{1}{L_y} \sum_{y=1}^{L_y} \langle c^\dagger_{x,y} c_{x,y} \rangle \,. \tag{3.7}$$

Because of the rotational symmetry around the cylinder, the ground states are translationally invariant along y, so we average the expectation values over each ring at a

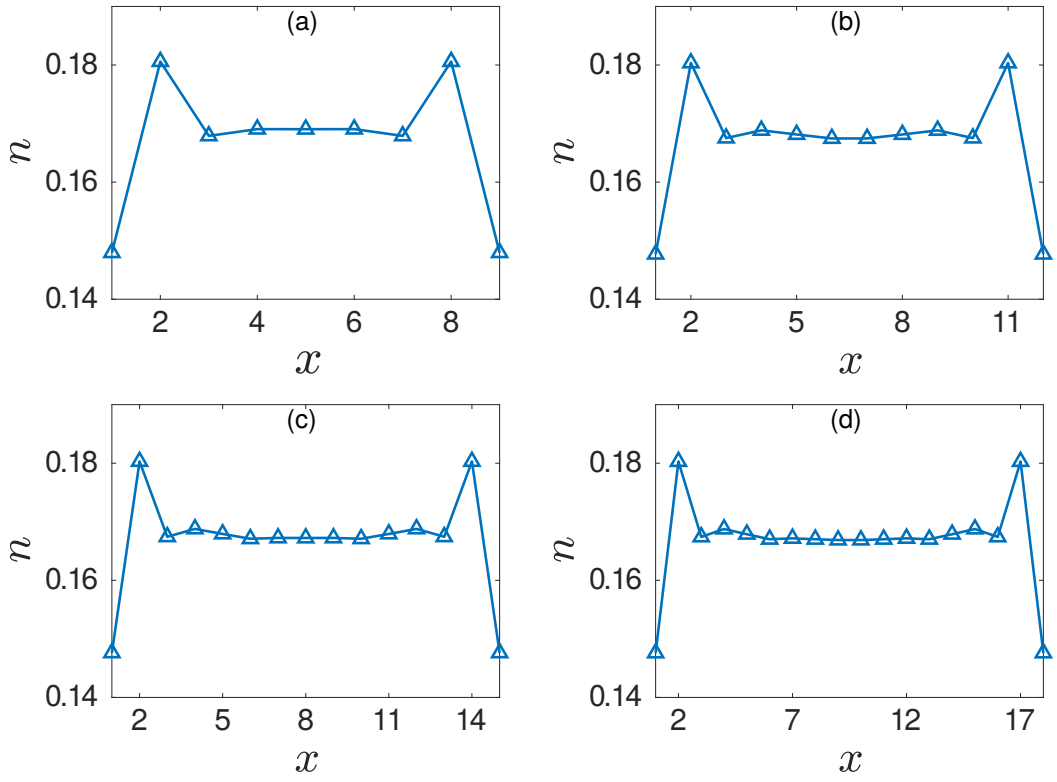


Figure 3.2: Particle density n as a function of the x coordinate for system sizes $L_x \times L_y$: (a) 9×6, (b) 12×6, (c) 15×6 and (d) 18×6. Lines connecting the data points are a guide to the eye.

fixed y, making $n(x)$ only dependent on the x coordinate. The rotational symmetry in y and the need to only consider the x dependence of the observables is a further advantage of our choice of cylindrical boundary conditions.

Previous works have calculated the density profiles of Laughlin states in the continuum for finite geometries such as the disk [167, 168]. They found that the density spreads uniformly in the bulk and shows a peak close to the edges before going to zero.

Fig. 3.2 shows the density profile of the ground state for four different lengths of the cylinder. In agreement with the behaviour of the Laughlin state in the continuum, the density has a uniform value in the bulk, with constant value $n \approx 0.17 \approx n_b$, where

n_b is the mean number of bosons. The density profiles have their lowest value at the edges of the cylinder and show a spike in the second outermost ring. The change in behaviour between bulk and edges become increasingly evident for larger values of L_x. The value of the density in the first and second ring, making up the spike, remain constant, but the additional central rings, making up the bulk of the cylinder, become progressively more uniform. We conclude that the density profiles are compatible with the behaviour of a Laughlin ground state.

3.3.2 Edge currents

To further characterise the ground state of the system we consider the behaviour of the currents around the circumference of the cylinder as a function of the x coordinate. We define the current $\mathcal{I}^y$ around the cylinder in the y direction as

$$\mathcal{I}^y(x) = \frac{1}{L_y} \sum_{y=1}^{L_y} \langle iJe^{i2\pi x\phi} c^\dagger_{x,y} c_{x,y+1} + \text{H.c.} \rangle \,. \tag{3.8}$$

Because of the rotational symmetry of the system around its circumference, the current does not depend on y and we average its value over y. In the sum, the lattice site with $y = L_y + 1$ is identified with $y = 1$ as a consequence of the periodic boundary conditions.

Fig. 3.3 shows the currents $\mathcal{I}^y$ as a function of the x coordinate for the four system lengths. For all of the system sizes, the currents have their maximal magnitude at the edges and have different signs at each edge. The sign difference indicates that the currents are chiral, meaning that they flow in opposite directions around each edge of the cylinder. The magnitude of the currents at the edges stays constant when increasing the system size. In the bulk, the current fluctuates close to zero and gets more uniform with a negligible magnitude for larger system lengths. The effect of the boundaries penetrates the bulk of the system for three sites from the edge where the

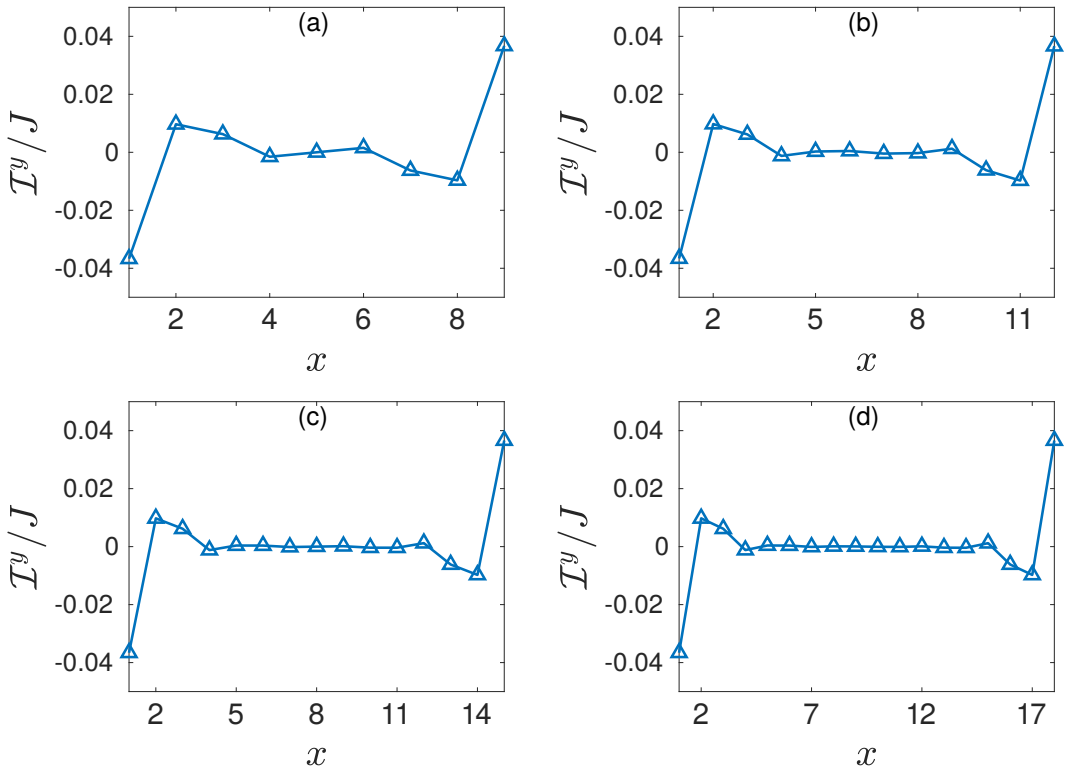


Figure 3.3: Current around the cylinder $\mathcal{I}^y/J$ as a function of the x coordinate for system sizes $L_x \times L_y$: (a) 9×6, (b) 12×6, (c) 15×6 and (d) 18×6. Lines connecting the data points are a guide to the eye.

current is significantly non-zero and oscillates around zero. These oscillations have the same extension into the bulk of the system as for those in the density profiles. The addition of more sites in the bulk does not affect the edge properties of the system.

This behaviour of the edge and bulk currents indicates the presence of conducting edges states and an insulating bulk. They are compatible with the physics shown by Laughlin states at filling $\nu = 1/2$. This further confirms the similarity of the lattice ground state with the Laughlin wavefunction.

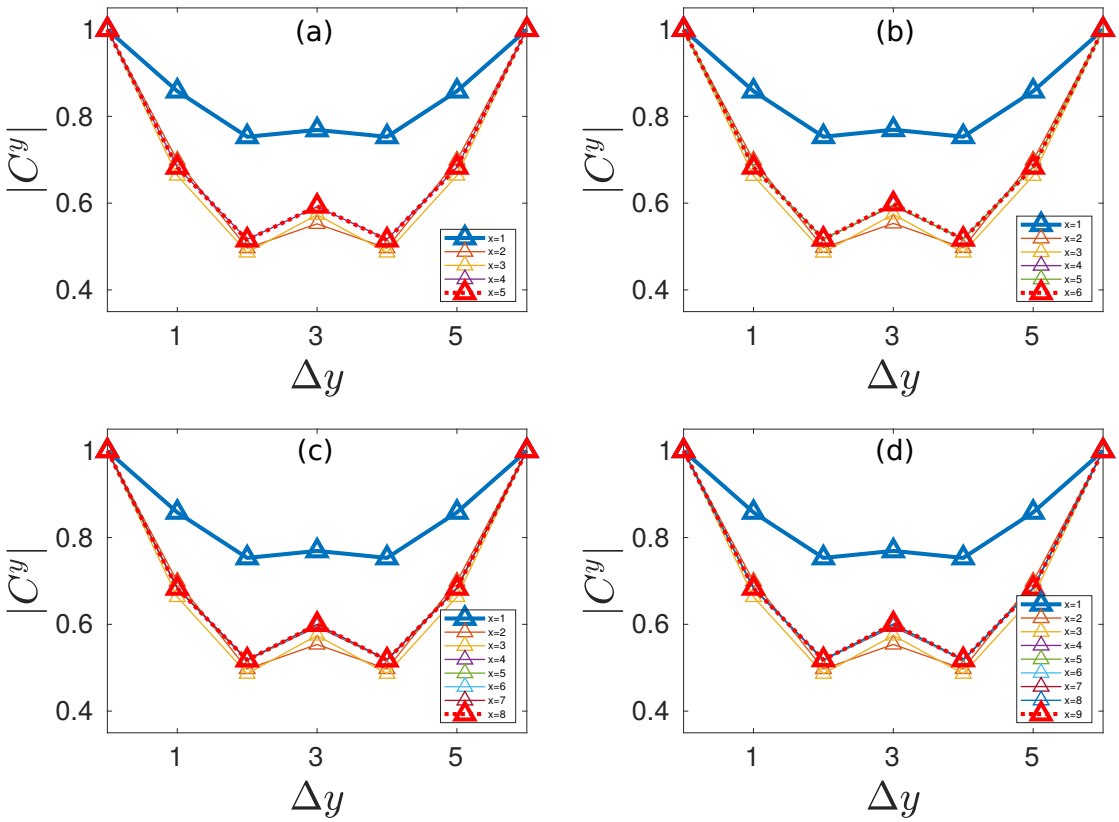


Figure 3.4: Correlation functions C^y for system sizes $L_x \times L_y$: (a) 9×6, (b) 12×6, (c) 15×6 and (d) 18×6. Each line represents the correlation function around a ring identified by its x coordinate. Only the rings from $x = 1$ to $x = L_x/2$ are shown due to the inversion symmetry of the cylinder. Lines connecting the data points represent a guide to the eye.

3.3.3 Correlation functions

To further characterise and distinguish the properties of the bulk of the system from those of the edge, we consider the one-particle correlation functions around the circumference of the cylinder. We write the correlation function along y as

$$C^y(x, \Delta y) = \frac{\langle c^\dagger_{x,1} c_{x,1+\Delta y} \rangle}{n(x)}, \tag{3.9}$$

which measures the correlation of two particles with the same x coordinate but Δy sites apart along y.

In the proximity of the edge, the correlation function is expected to decay algebraically as a function of the distance

$$C^y(x, \Delta y) \propto \frac{1}{\Delta y^\alpha}, \ for\ x \approx 1,\ L_x\,, \tag{3.10}$$

indicating the presence of a gapless edge mode. In a gapped bulk, where currents are absent, the correlation function is expected to decay exponentially

$$C^y(x, \Delta y) \propto e^{-\Delta y/\xi}, \ for\ x \approx L_x/2\,, \tag{3.11}$$

where ξ is the correlation length [123, 124].

Fig. 3.4 shows the correlation functions for each of the four system sizes we have considered. The separate lines in each plot represent the correlation function for a different value of x. The plots are similar for all system sizes. In each of the plots, there is a significant change in behaviour between the correlation functions at the edge of the cylinder, with $x = 1$, and all of the other ones in the bulk. Its decay is much slower as opposed to all of the other correlation functions. We find that the increased system size does not affect the edge properties of the system.

The behaviour of the correlation function is consistent with the slower decay in the presence of a conducting edge, where long-range correlations are present, and with a faster decay in the bulk, which is gapped and insulating. Despite the quantitatively slower decay of the correlation functions at the edges, the circumference of the cylinder is not sufficiently large to confidently conclude that the decay at the edge follows a power law and the decay in the bulk is exponential.

3.4 Interaction-strength dependence

The system we have considered so far was in the hard-core limit, corresponding to having an infinite on-site interaction in the lattice. However, the condensed-matter equivalent of the system is characterised by a finite interaction strength as a consequence of the Coulomb interaction. It is therefore of interest to explore how the ground state in the hard-core limit arises when increasing the on-site interaction strength starting from zero. Additionally, an experimental setting would have control over the on-site interaction strength of the bosons and would allow for the transition to be explored.

We consider a system with lattice size $L_x \times L_y = 9 \times 6$ at filling fraction $\nu = 1/2$, $\phi = 1/3$ and we vary the interaction strength U/J. For this value of ϕ, all of the observables we have previously studied confirm that the physics of the ground state is compatible with that of a Laughlin state.

We will focus on the behaviour of the currents and the correlation functions around the cylinder to characterise how the ground-state properties change with U/J.

In our DMRG calculations, we used a maximal occupation number at each site of $n_{\max} = 4$ and bond dimension $\chi = 500$. Only for $U = 0$ did we use $n_{\max} = 9$.

3.4.1 Edge currents

Following the analysis performed in the previous sections, we start by calculating the currents around the cylinder. We have already studied their behaviour in the hard-core limit where $U/J \to \infty$. Now we explore how this limit is reached by increasing U/J from the non-interacting case. Fig. 3.5 shows the currents $\mathcal{I}^y(x)$ for four values of the interaction strength from $U/J = 0$ to $U/J = 8$. For $U/J = 8$ [see Fig. 3.5 (d)] and above, the currents become almost indistinguishable from the hard-core limit. For smaller values of the interaction strength, the magnitude of the currents in the

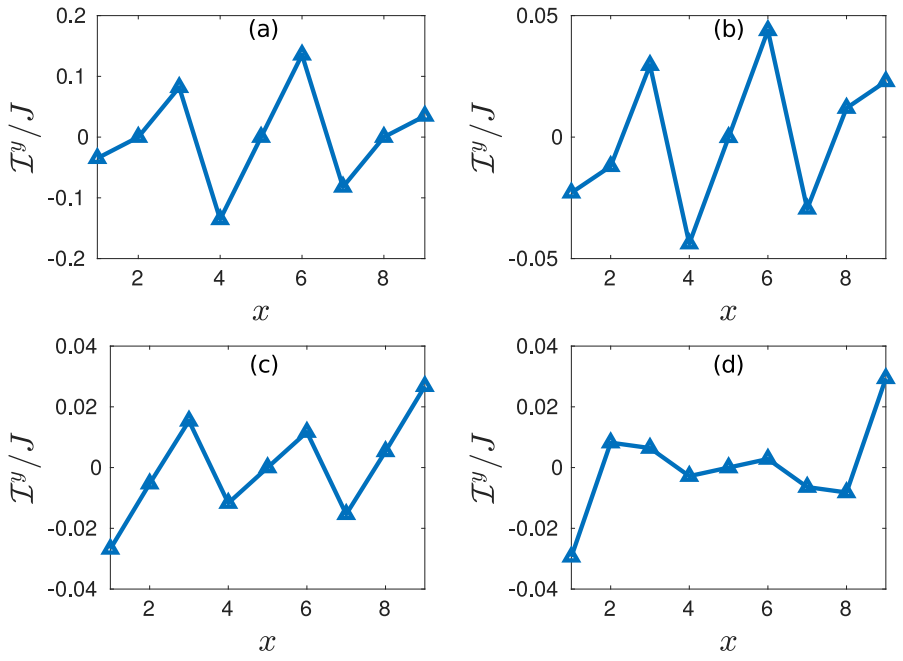


Figure 3.5: Current around the cylinder $\mathcal{I}^y(x)/J$ for an $L_x \times L_y = 9 \times 6$ lattice, with $\nu = 1/2$ and $\phi = 1/3$. The interaction strength takes values (a) $U/J = 0$, (b) $U/J = 0.1$, (c) $U/J = 2$, (d) $U/J = 8$. Lines connecting the data points are a guide to the eye.

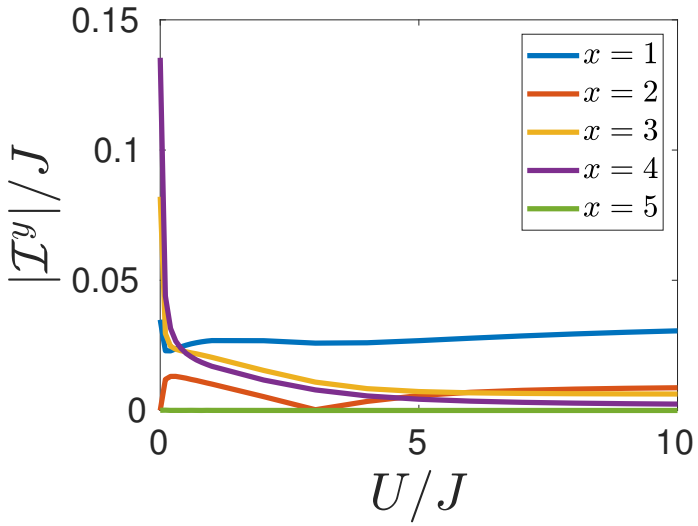


Figure 3.6: $|\mathcal{I}^y(x)|$ for an $L_x \times L_y = 9 \times 6$ lattice, with $\nu = 1/2$ and $\phi = 1/3$. Each line represents a different value of the x coordinate. Due to the inversion symmetry of the cylinder, only the first five lattice sites along x are considered.

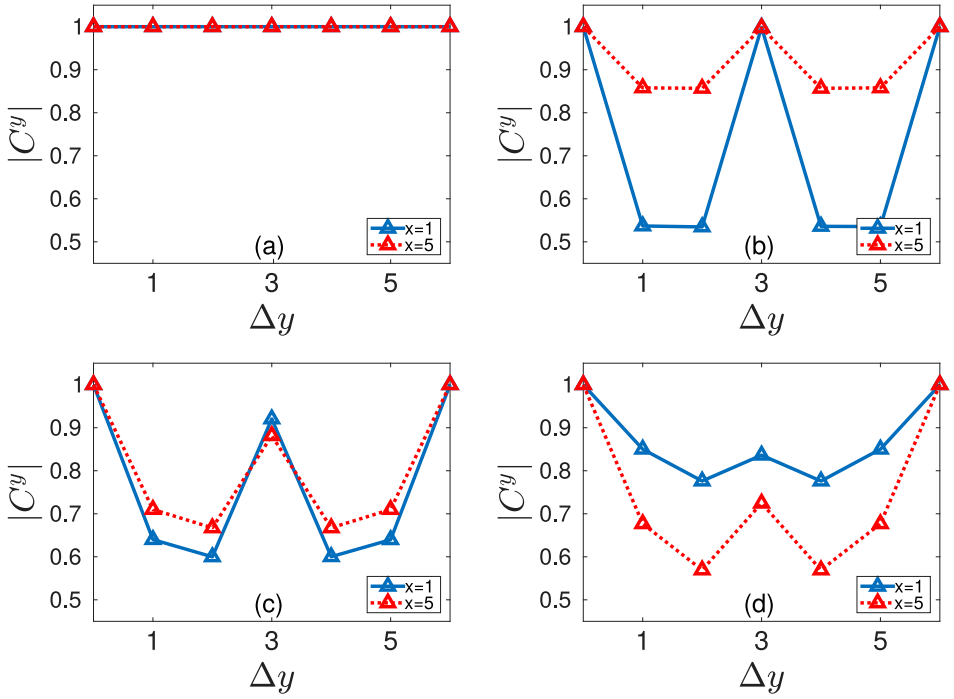


Figure 3.7: Correlation functions C^y for an $L_x \times L_y = 9 \times 6$ lattice, with $\nu = 1/2$ and $\phi = 1/3$. The interaction strength takes on values (a) $U/J = 0$, (b) $U/J = 0.1$, (c) $U/J = 2$, (d) $U/J = 8$. Lines connecting the data points are a guide to the eye.

bulk of the system increases and the edge currents are no longer dominant. For the non-interacting limit, the ground state shows strong currents oscillating in the bulk.

We can better understand the behaviour of the currents by computing their value around each ring of the cylinder as a function of the interaction strength. Fig. 3.6 shows such currents. Each line represents a different x coordinate up to the central ring which is always zero as a consequence of the inversion symmetry of the cylinder. The line of the central-most rings, with $x = 3$ and $x = 4$, have a non-zero current and decrease monotonically. The line corresponding to the ring located at the edge, with $x = 1$, quickly saturates after having a minimum around $U/J \approx 0.5$. This shows how, when increasing interaction strength, the edge currents become dominant.

3.4.2 Correlation functions

Let us consider the decay of the correlation functions around the cylinder $C^y(x, \Delta y)$ as defined in Eq. (3.9), when varying the interaction strength of the system. For the non-interacting limit where $U = 0$, we find that the correlation functions around the cylinder are constant for every value of the x coordinate. Fig. 3.7 (a) shows the correlation functions for $U = 0$. In Section 3.3.3, we found that, in the hard-core limit, only the correlation function at the edge differs from the ones in the bulk. Therefore, we plot only $C^y(1, \Delta y)$ and $C^y(5, \Delta y)$. These values are representative of the edge and bulk behaviour, respectively.

Fig. 3.7 (b-d) shows $C^y(x, \Delta y)$ with $x = 1$ and $x = 5$ for three representative values of $U > 0$. In the hard-core boson case, we have observed that the decay of the correlations is slower at the edges and faster in the bulk. We find that, for small but positive values of U, this behaviour is reversed. In particular, up to $U/J \approx 2.5$, the correlation at the edges decays significantly faster before showing a revival as shown in Fig. 3.7 (b) and (c). When $U/J > 2.5$ the bulk correlations decay faster than the edge ones, and when $U/J \approx 8$, they become close to the ones in the hard-core limit as shown in Fig. 3.7 (d). All correlations show a peak at $\Delta y = 3$ and although we cannot fully understand its presence, we assume it to be a finite-size effect.

3.4.3 Additional quantities

To further quantify how the hard-core limit is reached from the behaviour of the currents and correlation functions, we compute two new quantities. Using the currents from Eq. (3.8) we define

$$R_{\mathcal{I}} = \frac{|\mathcal{I}^y(1)|}{\sigma(\text{bulk})}\,, \tag{3.12}$$

where $\mathcal{I}^y(1)$ is the edge current and $\sigma(\text{bulk})$ is the standard deviation of the currents in the bulk. $R_{\mathcal{I}}$ quantifies how dominant the currents at the edge are relative to the

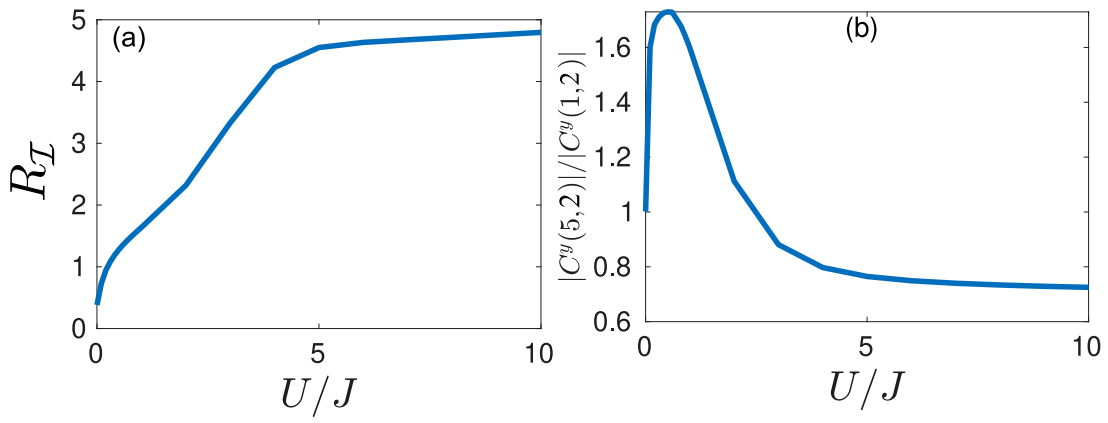


Figure 3.8: (a) $R_{\mathcal{I}}$ as defined in Eq. (3.12) for a system of size $L_x \times L_y = 9 \times 6$, $\phi = 1/3$ and $\nu = 1/2$. (b) Ratio $|C^y(5,2)|/|C^y(1,2)|$ of the decay after two sites of the correlation function in the bulk ($x = 5$) and at the edge ($x = 1$).

currents in the bulk. Fig. 3.8 (a) shows $R_{\mathcal{I}}$ as a function of U/J. $R_{\mathcal{I}} > 1$ when $U/J > 0.5$ indicating that the edge current becomes dominant. For larger values of the interaction strength, $R_{\mathcal{I}}$ increases monotonically and saturates for $U/J \approx 5$. For larger values, the behaviour of the currents becomes similar to that of the Laughlin-like state in the hard-core limit.

We also calculate the ratio between the value of the correlation function in the bulk ($x = 5$) and at the edge ($x = 1$) at a distance of two sites $|C^y(5,2)|/|C^y(1,2)|$. This quantity expresses the relative rate of decay of the correlations and is shown in Fig. 3.8 (b). For small values of U, this ratio has a larger-than-one value, becomes smaller than one when $U/J > 2.5$, and then decreases monotonically for larger values of U. This indicates the existence of a region of small U where the decay of correlation functions is faster at the edges as compared to the bulk, before becoming compatible with a Laughlin state. These results indicate that the transition from the non-interacting case to the hard-core limit goes through a transitory state, where $|C^y(5,2)|/|C^y(1,2)| > 1$. This state has physical properties which are distinct from those of a Laughlin state. The appearance of Laughlin-like physics only for large values of U is consistent with the results coming from the ED of small systems.

Fig. 3.8 (a,b) shows an additional striking feature of the transition from the non-interacting system to the hard-core limit. The transition appears to be completely smooth without a sharp change in any of the observables we compute. For small values of the magnetic flux $\phi < 0.2$, ED calculations for small systems [42] have shown that a sharp phase transition occurs at $U = 0$, where the ground state shows no topological order, to a topologically ordered ground state for $U > 0$. This transition is analogous to the continuum case.

Our system does not show this type of transition. This is because we have considered a large value of $\phi = 1/3$, where the discrepancy between the lattice system and its continuum version becomes significant. ED shows that the overlap of the ground state with the Laughlin function gradually increases as a function of U and no sharp transition is present. Our analysis extracts further details about the transition which complement the calculation of the overlap of the ground-state wavefunctions. Both the correlations and the currents show that the system goes through a state where the currents are dominant in the bulk, and the correlations decay faster at the edges, before reaching the Laughlin-like state from the non-interacting case.

3.4.4 $\phi = 1/4$

A different situation is expected for smaller values of ϕ where the overlap with the Laughlin state at $U = 0$ is larger [42]. We study the transition that occurs as a function of the interaction strength for a system with flux density $\phi = 1/4$ to explore whether a smaller flux density affects the smoothness of the transition we observed for $\phi = 1/3$. We consider a system with size $L_x \times L_y = 8 \times 4$, $\phi = 1/4$ and $\nu = 1/2$ and focus on the behaviour of the edge currents. Fig. 3.9 (a) shows $R_{\mathcal{I}}$ as a function of U/J. A sharp change in the value of $R_{\mathcal{I}}$, caused by a decrease of the denominator, occurs at $U/J \approx 9.8$ and then saturates. For small U, $R_{\mathcal{I}}$ increases sharply with U/J until $U/J \approx 3$, where it levels off and subsequently decreases slightly until the transition

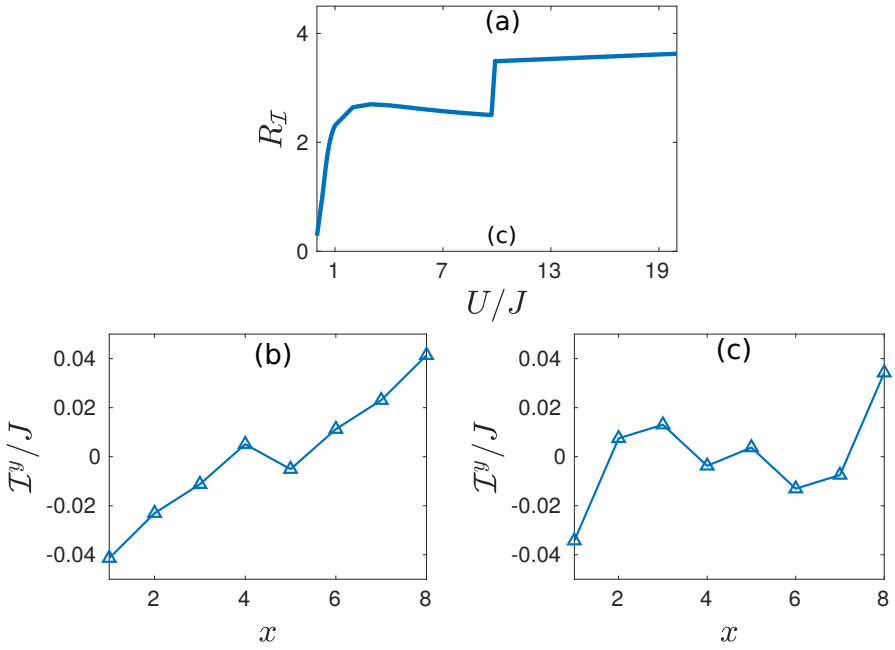


Figure 3.9: (a) $R_{\mathcal{I}}$ for a system of size $L_x \times L_y = 8 \times 4$, $\phi = 1/4$ and $\nu = 1/2$. Current $\mathcal{I}^y(x)/J$ for the system in (a) for $U/J = 9.6$ (b) and $U/J = 9.9$ (c). Lines connecting the data points in (b) and (c) are a guide to the eye.

point. Fig. 3.9 (b) and (c) show the corresponding edge currents immediately before and after the transition. Before the jump, for $U/J = 9.6$ the currents grow in a fashion close to linear with the distance from the centre. After the transition, for $U/J = 9.9$, only the edge currents are dominant, and they become reminiscent of the hard-core behaviour for the $\phi = 1/3$ case as in Fig. 3.5 (d). This suggests that lowering the flux density leads to a regime where a sharp transition occurs, in line with the results from ED calculations.

For the DMRG calculations, we used a maximum occupation number per site $n_{\max} = 4$, and bond dimension up to $\chi = 300$.

3.5 Conclusion and outlook

The fractional quantum Hall effect is the paradigmatic physical system showing topological order. All of the ingredients necessary to simulate its physics, i.e. 2D geometry, repulsive interaction potential and an orthogonal magnetic field have been realised and are available in quantum gas experiments. Additionally, experimental proposals for topologically non-trivial geometries, such as a finite cylinder, have been put forth as a way to simulate quantum Hall physics. Previous numerical studies of the ground state of such systems on a lattice using tensor network methods considered a torus geometry or an infinite cylinder. We have instead considered a finite cylindrical geometry. Quantum Hall physics is characterised by a variation in behaviour between the bulk and the boundaries of the system. The finite cylinder geometry has allowed us to consider this discrepancy. Moreover, physical edges are also inherently present in experiments as a consequence of their finite nature.

We have used the interacting bosonic Harper-Hofstadter model on a finite square lattice with cylindrical boundary conditions and computed its ground-state wavefunctions through DMRG calculations. We have shown how this system at filling fraction $\nu = 1/2$ supports topologically ordered ground states by estimating its topological entanglement entropy in Sec. 3.2. Not only was the value of the topological entanglement entropy non-zero, but it was in good agreement with the theoretical prediction for a $\nu = 1/2$ Laughlin state in the continuum. This was further confirmed by the two-fold degeneracy of the ground states we have obtained.

Taking advantage of the finite cylindrical geometry of the system and the presence of physical edges, we have computed a set of observables, related to edge properties, to explore the compatibility of the ground state with the physical features typical of a Laughlin state. Such properties cannot be inferred solely from the ground-state overlap with the Laughlin wavefunction typically used as means of comparison in small systems on a torus geometry using ED. For large values of the magnetic flux

density, where the overlap quickly becomes small, additional quantities become useful to make a comparison of the physical properties.

We have successfully studied the behaviour of the density profiles, the currents and correlation functions around the cylinder. We find that all of these observables are fully compatible with the features of a fractional quantum Hall ground state corresponding to a Laughlin wavefunction in the continuum. The overall results are indicative of a ground state with a gapped insulating bulk with exponentially decaying correlation functions and gapless edge modes that lead to chiral edge currents with power-law decaying correlations.

In the second part of the chapter, we have dropped the hard-core constraint to consider general values of the on-site interactions. The correlations and the currents show that the transition to the fractional quantum Hall state is smooth, indicating the absence of a sharp transition. Moreover, for small values of U/J, a transient state occurs where the correlations in the edge decay faster than those at the bulk. When $U/J > 2.5$, the correlation functions and currents show the same qualitative behaviour as the Laughlin state, and they become close to the hard-core boson limit when $U \approx 8$. Additionally, the use of the ratio of the currents at the edge to the variation of the currents in the bulk $R_{\mathcal{I}}$, and the ratio of the correlations $|C^y(5,2)|/|C^y(1,2)|$ strongly indicate that there is no sharp transition that induces the fractional quantum Hall state from the non-interacting case. Considering a state with smaller flux density $\phi = 1/4$ we observe from the currents around the cylinder that a sharp jump of the ratio $R_{\mathcal{I}}$ occurs for large U. The behaviour of the currents become compatible with the Laughlin state after the transition.

The physics of quantum Hall systems in lattices away from the continuum is still not completely understood for a wide range of parameters. For large magnetic fluxes, which can be experimentally reached, the physics of the system is the most different from the continuum limit and most interesting to explore. The density profiles and the

correlation functions that we have calculated for the ground states of the system can be measured in experimental implementations of the system using ultracold atoms and can be used as signatures for detecting fractional quantum Hall states. An additional advantage of the cylindrical geometry is that it is suitable to reproduce Laughlin's thought experiment [75], in which one flux quantum is threaded through the cylinder axis, inducing a transfer of particles from one edge of the cylinder to the other. In this way, the Hall conductivity of the system can be derived. An interesting direction of future research for this system is to implement the flux threading procedure to further characterise the ground state of the system and explore how the presence of physical edges affects the transfer of particles.

Chapter 4

Dipolar Bose-Hubbard ground states on a finite lattice

Quantum gases in optical lattices have become a powerful tool to perform quantum simulation of strongly-correlated system models originating from condensed-matter physics. The set of observables typically used in condensed-matter physics experiments to characterise the state of the system is not always directly accessible when using ultracold gases. Therefore, it is essential to investigate how order parameters accessible in either type of system lend themselves to characterise the phases they support.

Ultracold molecules in optical lattices are an attractive experimental implementation of a system with dipolar interactions, and we consider it as our system of reference. The progress in trapping and cooling dipolar molecules [176, 177] has led the way to the realisation of ultracold polar molecules in optical lattices [55, 178, 56, 179]. The dipolar interaction leads to the realisation of many different phases such as superfluid, supersolid, solid [58, 180, 181, 182], and even topological phases [183, 184, 185, 186].

Theoretical calculations and numerical simulations typically identify the phases of the system in the grand-canonical ensemble through the use of order parameters,

which show a sharp change as a function of a control parameter in the thermodynamic limit where the number of particles $N \to \infty$. On the other hand, the experimental implementation of such systems is characterised by a finite system size with the presence of boundaries, and a generally small number of particles. Moreover, many of the order parameters used in numerical simulations come from a condensed-matter tradition. A clear example is the structure factor, which is accessible in solid-state physics through neutron scattering and is, therefore, a natural quantity to consider. However, in the ultracold gas implementation of these types of Hamiltonian, the structure factor is not always accessible although it has been measured experimentally in cold-atom setups through the measurement of compressibility or density fluctuations [187, 188]. Therefore, it becomes crucial to explore how different states can be identified in finite systems using the toolbox of ultracold gases in an optical lattice.

In this chapter, using DMRG calculations, we systematically calculate and compare a set of observables used in numerical simulations and available in ultracold gas lattice experiments and analyse how well they are suited to determine the phase of a finite-size dipolar Bose-Hubbard model on a 2D square lattice. This analysis aims at giving guidance to experiments on how to practically observe the phases supported by the system and to simulations by proposing observables which are relevant to experiments.

This chapter is structured as follows: in Section 4.1 we introduce the dipolar Bose-Hubbard model and the specifics of our system. Section 4.2 describes the results we obtained for the half-filled case, focusing on how to characterise solid order in Section 4.2.1 and superfluid order in Section 4.2.2; in Section 4.2.3 we use the entanglement entropy to further identify the transitions. Section 4.2.4 studies the effects of the boundary conditions and finite size on the system. In Section 4.3, we characterise the supersolid state that appears when adding an extra particle to the half-filled system and in Section 4.4 we explore the star solid state of the system at

quarter-filling. In Section 4.5, we use unsupervised learning techniques to explore whether density measurements available from quantum gas microscope experiments can be used to discriminate between the states of the system. Finally, in Section 4.6, we summarise the results of this chapter.

The results presented in this chapter have been published in Ref. [62].

4.1 Dipolar Bose-Hubbard model

We consider a dipolar Bose-Hubbard (dBH) model composed of spinless bosons. The bosons inhabit a square lattice with L_x sites in the x direction and L_y sites in the y direction. We fix all dipole moments to be aligned and orthogonal to the lattice such that the dipolar interaction becomes repulsive and isotropic. The Hamiltonian of the system reads

$$H = -J \sum_{\langle i,j \rangle} b_i^\dagger b_j + \frac{1}{2} \sum_{i \neq j} \frac{V}{|i-j|^3} n_i n_j \,, \tag{4.1}$$

where b_i is the annihilation operator for a boson at site i, satisfying bosonic commutation relations $[b_i, b_j^\dagger] = \delta_{ij}$ and $n_i = b_i^\dagger b_i$ is the number operator at site i. J is the hopping amplitude, V characterises the long-range static dipole interaction and it can be expressed as $V = D^2/a^3$ where D is the dipole moment and a is the lattice spacing, such that $|i-j|$ is the distance between sites i and j in units of a. $\langle \ldots \rangle$ represents nearest-neighbour pairs. The Hamiltonian in Eq. (4.1) describes molecules confined to a 2D plane by a strong transverse trapping field, with harmonic frequency $\omega_\perp$, which prevents the molecules from collapsing from the attractive interaction between aligned dipoles. By appropriately tuning $\omega_\perp$ [189, 190], the minimum available inter-particle distance suppresses the tunnelling to already occupied sites [191]. Assuming that the initial configuration of the lattice has no double occupations, the molecules effectively behave as if they were hard-core bosons and therefore collisionally stable, avoiding losses in multiply-occupied sites due to inelastic collisions [192, 193] and/or

so-called 'sticky collisions' (whereby two molecules form a long-lived complex which is unobservable) [194, 195]. We impose a hard-core constraint such that the local Hilbert space at each site is restricted to have either zero or one boson. As a consequence, there is no on-site interaction term in the Hamiltonian of Eq. (4.1).

Although the dipolar interaction has an infinite range, we perform a cut-off of the interaction length to $|i-j| = \sqrt{8}$ in units of the lattice spacing a. This corresponds to considering terms up to the fifth nearest neighbour. In a cold molecule setup made with RbCs ($D \approx 1.2$ Debye) and lattice constant $a = 532$nm, this cut-off corresponds to neglecting interactions weaker than $\approx k_B \times 3$nK, as smaller interaction effects would be washed out by finite temperature effects.

We work in the canonical ensemble by fixing the total number of bosons N in the system and lattice filling $\nu = N/(L_x L_y)$. We consider the lattice to have periodic boundary conditions (PBC) along the y direction. This turns the square lattice into a finite cylinder. The cylindrical geometry has several advantages. It gives access to both bulk and boundary properties of the system and, as explained in Chapter 2, it is amenable to getting accurate results thorough DMRG calculations. Besides, the finite geometry that we are considering is similar to the experimental implementations where boundary effects are present.

The finite size of the system affects the ground states that are supported. In the presence of the repulsive dipolar interactions, the bosons are pushed away from each other. If the system has boundaries, it is energetically advantageous for the particles to localise in their proximity, because they will only be subject to interaction energy of the bosons on the inside of the system. The bosons will, therefore, tend to move close to the boundaries. Section 4.2.4 will analyse the effect of the edges and the use of open boundary conditions (OBC).

The PBC around the cylinder also affect the sizes of the systems we study. As an example, let us consider the system in the checkerboard solid ground state, which

occurs for half filling $\nu = 1/2$ in the strong interaction limit [see Fig. 4.1 (b)]. In this case, the bosons occupy only one of the two checkerboard sub-lattices in the system. If the lattice dimension L_y is odd, the system becomes frustrated as the two distinct checkerboard sub-lattices are no longer well defined. Throughout our analysis, we are careful to choose system sizes that are compatible with this effect.

All of our DMRG calculations are carried out using the methods described in Chapter 2. We fix the total number of particles in the system by imposing $U(1)$ quantum number conservation symmetry [11]. For all of the system sizes we consider, a maximum bond dimension of $\chi = 1000$ ensures convergence for all of the expectation values we have computed.

In the next section, we start considering the dBH system at half filling.

4.2 Half filling

In this section, we study how the dipolar interaction strength V/J affects the ground states of the dBH system in a finite cylindrical geometry at a fixed filling fraction $\nu = 1/2$. We determine the state of the system by considering a set of observables used as order parameters to identify solid order and superfluid (SF) order. We will use the structure factor, the occupation imbalance and the density profiles to study the solid order. We will calculate the one-body density matrix, the correlation functions, and the natural occupation numbers to study the SF order. Finally, we will calculate the entanglement entropy, which proves to be a versatile quantity to detect transitions.

4.2.1 Solid order

Solid order is characterised by a modulation of the density-density correlations. For example, the structure of a crystal is determined through X-ray or neutron scattering. The radiation hitting a periodic density distribution is scattered by it, and will show

intensity peaks located at the maximum of the static structure factor. In our 2D lattice, the static structure factor is defined as the Fourier transform of the density-density correlations

$$S(k_x, k_y) = \frac{1}{(L_x L_y)^2} \sum_{x,y,x',y'} e^{ik_x(x-x')+ik_y(y-y')} \langle n_{x,y} n_{x',y'} \rangle \,, \tag{4.2}$$

where the angular brackets represent the expectation value with respect to the ground-state wavefunction and, for the sake of clarity, we have switched to a notation where the subscripts (x, y) represent the x and y coordinates of the site in the 2D lattice. A non-zero value of the structure factor at momentum $(k_x, k_y) \neq (0, 0)$ indicates the presence of solid order and a single realisation of the state will show a periodic modulation of the density. The density is defined as the expectation value of the number operator at each site

$$\tilde{n}_{x,y} = \langle n_{x,y} \rangle \,. \tag{4.3}$$

For example, for the checkerboard solid configuration present at filling $\nu = 1/2$, the structure factor has a peak at $(k_x, k_y) = (\pi, \pi)$ and value $S(\pi, \pi) = 1/4$ in the thermodynamic limit. $S(k_x, k_y)$ has been commonly used in numerical simulations [196, 197] to identify solid order in optical lattice setups. Figure 4.1 shows instances of the density pattern $\tilde{n}_{x,y}$ in the limits of small interaction at $V/J = 1$, where the density is uniform in the bulk, and for a large value of the interaction at $V/J = 10$, showing a checkerboard pattern in the density characteristic of solid order. In the solid regime, each realisation of the ground state occupies one of the two available checkerboard sub-lattices.

In the presence of a discrete lattice, as in our dBH model, the lattice potential provides a privileged frame from where to determine the density modulation. Therefore, we choose the occupation imbalance as an alternative quantity which is able to capture solid order and is accessible in quantum gas microscope setups [39, 198, 199].

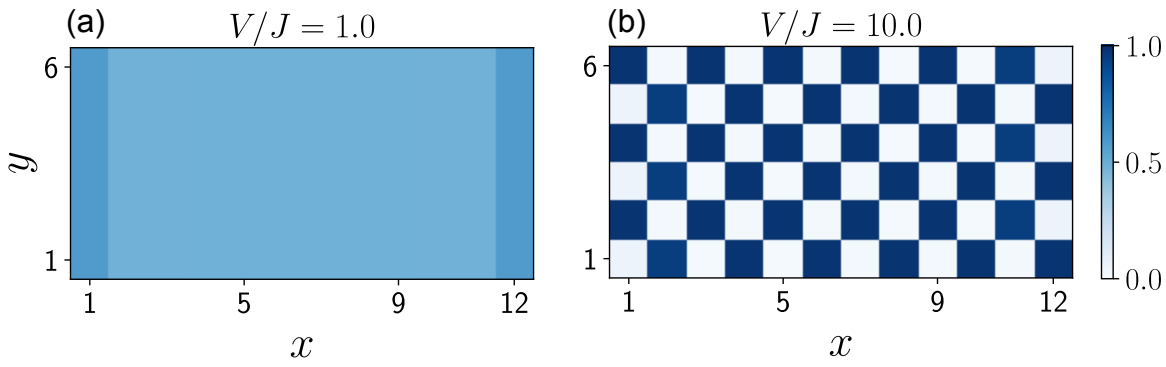


Figure 4.1: Local density $\tilde{n}_{x,y}$ at $V/J = 1$ (a), $V/J = 10$ (b) for lattice size $L_x \times L_y = 12 \times 6$ and $\nu = 1/2$.

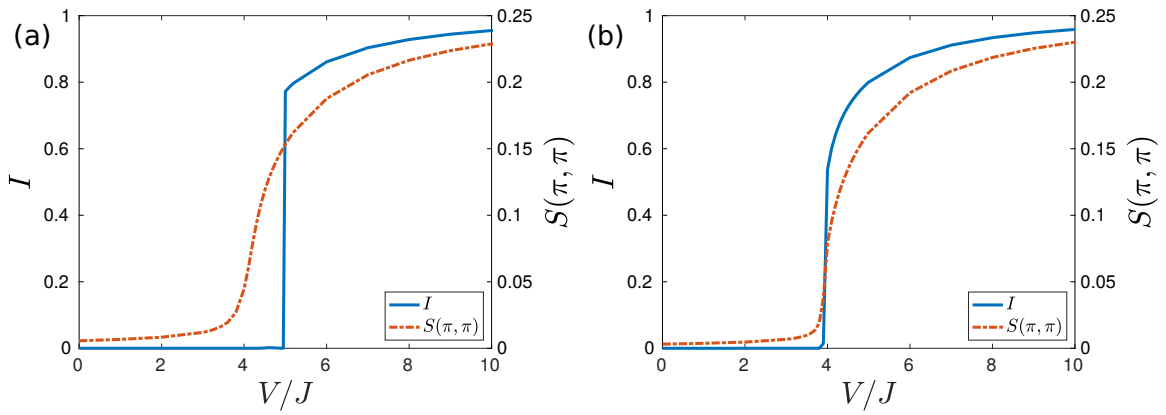


Figure 4.2: Structure factor $S(\pi, \pi)$ and occupation imbalance I as a function of the interaction strength V/J at filling $\nu = 1/2$ for lattice size (a) $L_x \times L_y = 12 \times 6$ and (b) $L_x \times L_y = 16 \times 8$.

The occupation imbalance I, for the checkerboard solid, reads

$$I = \left| \frac{\sum_{x,y} (-1)^{(x+y)} \tilde{n}_{x,y}}{\sum_{x,y} \tilde{n}_{x,y}} \right| , \tag{4.4}$$

and it condenses the information of $\tilde{n}_{x,y}$ into a single number by quantifying how the two equivalent checkerboard sub-lattices are populated. A uniform distribution has occupation imbalance $I = 0$ and a checkerboard pattern has $I = 1$. We calculate the structure factor and the occupation imbalance as order parameters to identify solid order, and we examine the density profiles to obtain a more qualitative picture for the properties of the ground state.

We consider two system sizes, $L_x \times L_y = 12 \times 6$ and $L_x \times L_y = 16 \times 8$, to explore how the size of the system affects the transition. Fig. 4.2 shows the structure factor and occupation imbalance for both system sizes as a function of the interaction strength V/J. For the smaller system size, the occupation imbalance and structure factor behave differently in proximity to the transition point [see Fig. 4.2 (a)]. The imbalance shows a sharp change from zero to a finite value, indicating the transition to a state where the particle density has a checkerboard pattern. On the other hand, the structure factor increases in a gradual way, showing no clear discontinuity. This difference in behaviour is a consequence of the finite size of the lattice and a manifestation of the effect of the boundaries. We can better understand this effect by observing the density pattern in the window of interaction strength where the imbalance is still zero, but the structure factor is non-zero. Fig. 4.3 shows the density profile for $V/J = 4.7$. For this value of the interaction strength, we observe that the checkerboard pattern is slowly starting to form at the centre of the lattice. We notice, however, that this effect is minimal, as shown by the scale of the colour bar in the figure. The difference in the value of the density between the central sites which are seeding the checkerboard pattern is of the order of 10^{-3}. Such a small difference is negligible for the overall occupation imbalance but affects the value of the structure factor.

When we consider the larger system size with $L_x \times L_y = 16 \times 8$ the difference in behaviour for the two observables diminishes considerably [see Fig. 4.2 (b)]. Close to the transition point, both the occupation imbalance and the structure factor show a sharp change. The discontinuity indicates that the transition is of the first order, in agreement with the Landau-Ginzburg-Wilson theory for the transition from the SF to the checkerboard solid phases which break two different symmetries: the Z_2 symmetry of the checkerboard solid and the $U(1)$ symmetry of the SF [200].

The analysis of the structure factor and occupation imbalance for the two system

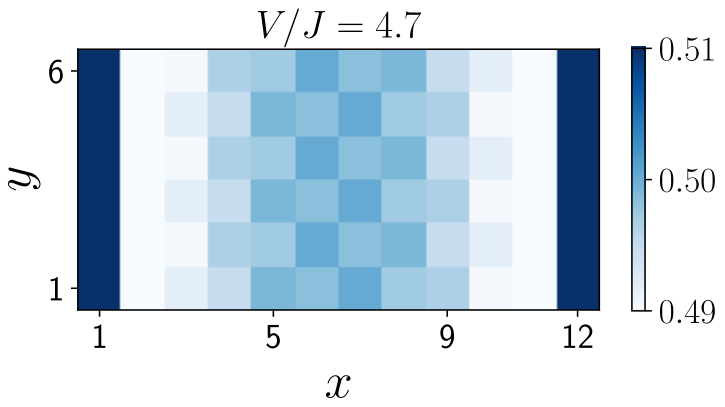


Figure 4.3: Density $\tilde{n}_{x,y}$ for $V/J = 4.7$ at filling $\nu = 1/2$ for lattice size $L_x \times L_y = 12 \times 6$.

sizes brings us to the conclusion that the structure factor is more sensitive to finite-size effects and is less accurate at capturing the position of the transition for small systems. We consider the transition point given by the imbalance to be more accurate than the one obtained from the structure factor in the smaller system. This is because the transition point obtained from the imbalance agrees with the observables that we calculate in the following sections.

4.2.2 Superfluidity and off-diagonal long-range order

In order to fully characterise the state of the system, it is necessary to find quantities that signal off-diagonal long-range order typical of a SF. Superfluidity is a complex phenomenon commonly associated with a range of properties of a system (dissipationless flow through narrow capillaries, quantised circulation, etc.) [201, 202]. It often appears connected with Bose-Einstein condensation, which is the macroscopic occupation of one single-particle state [201, 202]. Macroscopic occupation exists if the largest eigenvalue of the one-body density matrix (OBDM) is of the order of the number of particles in the system [203, 204, 205]. In two spatial dimensions, as for our system of interest, the Hohenberg-Mermin-Wagner theorem precludes true long-range order and condensation, because of the thermal phase fluctuations of the order

parameter [202]. However, for finite two-dimensional systems, algebraic decay of correlations in the OBDM is sufficient to imply a non-zero SF density and non-vanishing condensate fraction, in agreement with the Josephson relation between these quantities [206, 207]. Experimentally, condensation in cold-atom lattice systems has been determined by measuring the momentum distributions after release from the trap and ballistic expansion [97, 198], while superfluidity in two dimensions has been established, e.g., by the observation of dissipationless flow of a cold atomic gas past an obstacle moving below a critical velocity [208].

Based on these considerations, we have calculated the OBDM, from which we obtain the condensate fraction and the non-local density correlations and analyse their decay as a signal of superfluidity in 2D.

Having access to the full form of the ground-state wavefunction from the DMRG calculation, we compute the OBDM as

$$\rho(x, y, x', y') = \langle b^\dagger_{x,y} b_{x',y'} \rangle \,. \tag{4.5}$$

Let us first consider the condensate fraction and the natural occupation numbers for the ground state. We obtain the natural occupation numbers as the eigenvalues of the OBDM and the corresponding eigenvectors are the natural orbitals [203, 209]. The condensate is the orbital with the largest eigenvalue. Let us name the eigenvalues of $\rho(x, y, x', y')$ by e_i, with $i = 1, \ldots, L_x L_y$. The condensate fraction of the ground state is e_1/N. The condensate fraction can be experimentally measured in optical lattice setups, associating e_1 with the population of the lowest-momentum state [97, 198, 210]. Although there is no direct experimental access to higher occupation numbers, $e_{j>1}$, we also numerically consider the difference between the two largest natural occupation numbers $\delta_e = e_1/N - e_2/N$.

Fig. 4.4 shows the behaviour of the condensate fraction e_1/N and δ_e as a function

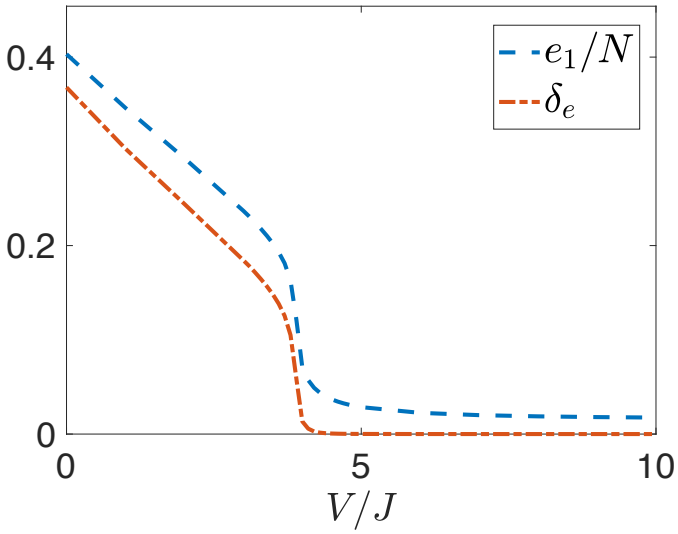


Figure 4.4: Condensate fraction e_1/N and δ_e at filling $\nu = 1/2$ for lattice size $L_x \times L_y = 16 \times 8$.

of the interaction strength V/J for the $L_x \times L_y = 16 \times 8$ lattice. The condensate fraction of the ground state before the transition is an indicator of the SF regime and is, therefore, a good order parameter for this finite system. For $V/J > (V/J)_c$, the critical interaction strength for the appearance of solid ordering, the condensate fraction is approximately $1/N$, while it reaches ≈ 0.4 for $V/J \to 0$ in the $L_x \times L_y = 16 \times 8$ lattice, in agreement with the findings in [58]. The condensate fraction is still considerably smaller than 1 as a consequence of the strong correlations in the system, due to the hard-core constraint, leading to a depletion of the dominant single-particle state. Looking closely at the behaviour of both observables, we see that δ_e reacts more sharply through the transition as compared to the condensate fraction. This is because, when there is no preferential occupation of the condensate state, $\delta_e \to 0$ whereas $e_1/N \to 1/N$.

As an additional measure of SF order we consider the behaviour of the single-particle correlation functions along the axis of the cylinder. The correlation function

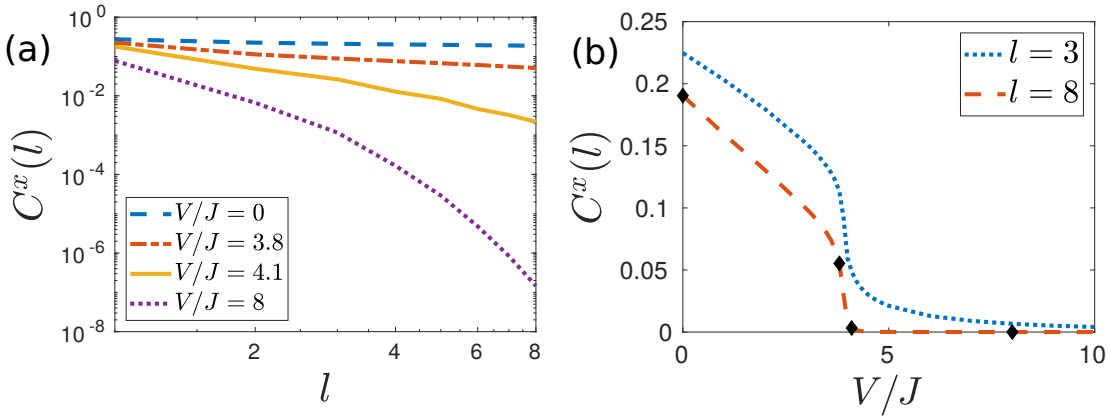


Figure 4.5: (a) Correlation functions $C^x(l)$ along the axis of the cylinder for four interaction strengths for the $L_x \times L_y = 16 \times 8$ system. Both axis are in a logarithmic scale. (b) $C^x(3)$ and $C^x(8)$ as a function of the interaction strength V/J. The diamonds correspond to the interaction strengths chosen in (a).

in the x direction reads

$$C^x(l) = \langle b^\dagger_{x,y} b_{x+l,y} \rangle \, . \tag{4.6}$$

The phase of the ground state determines the type of decay shown by $C^x(l)$. In fact, in two dimensions, a SF state has correlation functions that decay with a power law, whereas in the solid state the decay is exponential, signalling a lack of long-range coherence. Fig. 4.5 (a) shows the behaviour of the correlation functions for several representative values of the interaction strength, chosen in the SF limit, immediately before and after the transition, and in the solid limit. Using a logarithmic scale for both axes of the plot stresses the difference between power-law and exponential decay of the correlations. Power-law decay looks linear, whereas exponential decay has a downward bend. Immediately before and after the transition, the correlation functions behave differently indicating the change in state. To better show how rapidly the decay changes at the transition, it is insightful to plot the value of the correlation functions at a fixed distance, as a function of the interaction strength. For the system length $L_x = 16$, we choose two sample distances for $C^x(l)$ with $l = 3$ and

$l = 8$. Fig. 4.5 (b) shows $C^x(3)$ and $C^x(8)$. They both show a sharp change at the transition value $(V/J)_c \approx 3.9$. The difference in behaviour between the exponential and power-law decay is particularly evident at a distance of 8 sites, where $C^x(8)$ is negligible in the solid but still non-zero in the SF regime. The location of the transition given by the correlations is in strong agreement with the other observables we have considered, indicating a transition at $V/J = 3.9$ for the $L_x \times L_y = 16 \times 8$ lattice size. We have limited the maximum value of l to 8 to avoid boundary effects, and for each value of l we only used sites in the centre-most area of the lattice, always staying at least four sites away from the boundary, and averaged over all y coordinates.

4.2.3 Entanglement entropy

A large body of research is focused on the study of the entanglement entropy of strongly correlated systems as a means to characterise their properties [211, 212, 213]. For systems with local interactions, the entanglement entropy upon bipartition is known to follow area laws [92, 139] that govern the scaling of the entanglement entropy with the boundary area of the bipartition. The coefficients of the scaling contain information on the nature of the ground state and the type of excitations it supports, and can even be used to characterise topological order, as we have done in Chapter 3. The entanglement entropy has been recently used to characterise the transition in many-body localisation and topological phases in quantum gas experiments [199, 214]. The entanglement entropy of four-site and six-site one-dimensional (1D) Bose-Hubbard systems in an optical lattice was measured through the quantum interference of two copies of a state [214, 215]. Ref. [199] assessed the growth of entanglement entropy in larger 1D systems by measuring local density fluctuations and comparing with DMRG simulations.

We calculate the entanglement entropy of the ground state to investigate whether

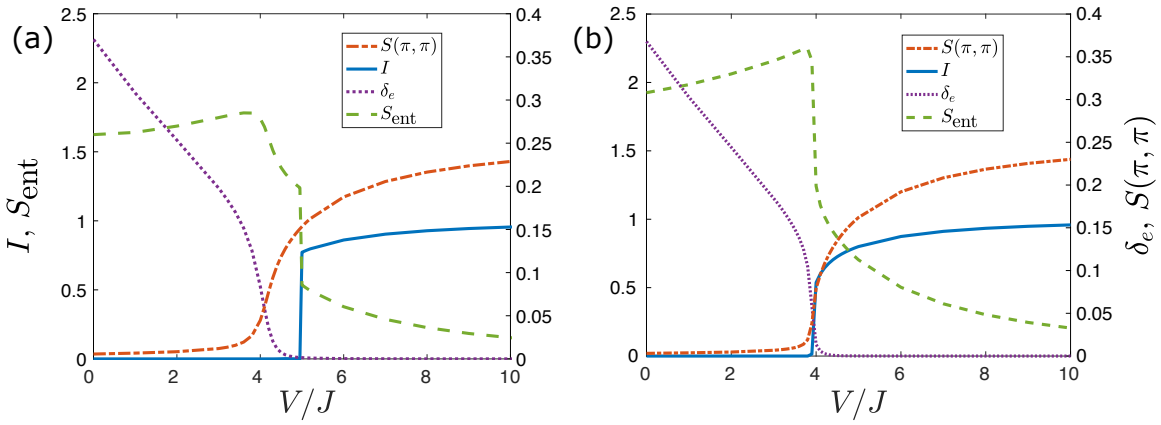


Figure 4.6: Structure factor $S(\pi,\pi)$, occupation imbalance I, natural occupation number difference δ_e, and entanglement entropy S_{ent} as a function of the interaction strength V/J at filling $\nu = 1/2$ for lattice size (a) $L_x \times L_y = 12 \times 6$ and (c) $L_x \times L_y = 16 \times 8$.

it can be used as an additional quantity to discriminate between the states supported by the system. For a bipartite system, the entanglement entropy S_{ent} reads

$$S_{\text{ent}} = -\text{tr}[\rho_L \ln(\rho_L)] = -\sum_i |\lambda_i|^2 \ln(|\lambda_i|^2)\,, \tag{4.7}$$

where ρ_L is the density matrix of the left part of the system after the bipartition. We perform the bipartition of the system by dividing the lattice into two equal parts, each of size $L_y \times L_x/2$. The second part of Eq. (4.7) indicates how we compute S_{ent} from the MPS formulation for the ground state. The λ_i are the Schmidt coefficients which are directly accessible from the results of the DMRG calculations.

Fig. 4.6 shows S_{ent} for both of the system sizes we have considered. In both cases, it shows a sharp change in correspondence of the transition point. This suggests that the entanglement entropy is highly sensitive to the transition and is a useful quantity to identify its location. Additionally, the decrease in value for S_{ent} at large values of the interaction indicates the lack of long-range coherence for the solid state. Its non-zero value before the transition signals the presence of long-range correlations in the ground state.

All of the order parameters and observables we have considered, shown in Fig. 4.6, confirm the presence of a transition from solid to SF at a critical value of the interaction strength $(V/J)_c$ that only depends on the system size. For the $L_x \times L_y = 12 \times 6$ system, it is $(V/J)_c \approx 4.9$, and for the largest system we have considered, $L_x \times L_y = 16 \times 8$, it is $(V/J)_c \approx 3.9$, which should be compared to the value of $(V/J)_c \approx 3.5$ obtained in the thermodynamic limit by quantum Monte Carlo methods [216]. All of the observables agree on the position of the transition, and we conclude that, for small system sizes and in the presence of boundary effects, the static structure factor is less sensitive to the transition than the occupation imbalance. The occupation imbalance, the condensate fraction, and the entanglement entropy are a set of experimentally accessible quantities that can accurately identify the location of the transition and the type of states in this finite-size system.

4.2.4 Lattice size and boundary conditions

As mentioned in Section 4.1, the size and boundary conditions of the system strongly affect its ground states. Let us consider a system size $L_x \times L_y = 12 \times 6$ with OBC. Because the interaction is repulsive and the boundary conditions are open both in the x and y directions, the occupation of the four corner sites of the system is energetically preferred. Fig. 4.7 shows the density profile of the ground state for two interaction strengths before the transition and deep into the solid limit. Fig. 4.7 (a) shows how, before the transition to the checkerboard solid, the four corners of the system are preferentially populated. Fig. 4.7 (b) shows how, after the transition, in the solid limit, the ground state forms three domains. One domain extends throughout the whole system, while the remaining two are confined around two opposite corners.

In the following section, we show an example of a checkerboard solid ground state for a system size and filling fraction compatible with OBC, without the appearance of domains.

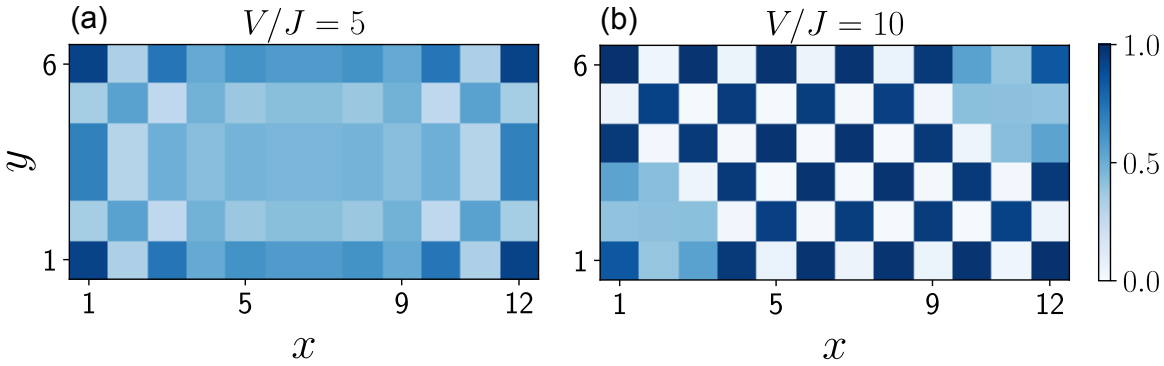


Figure 4.7: Local density $\tilde{n}_{x,y}$ for $V/J = 5$ (a), $V/J = 10$ (b) for lattice size $L_x \times L_y = 12 \times 6$, filling fraction $\nu = 1/2$ and OBC.

4.2.4.1 Checkerboard solid with open boundary conditions

We consider a system with OBC in both x and y direction with system size $L_x \times L_y = 7 \times 13$, and filling fraction $\nu = 46/91$. Both L_x and L_y are odd and the filling fraction is chosen such that, in the strong interaction regime, all of the lattice sites for which $(-1)^{(x+y)} = 1$ are occupied. Only one of the two available checkerboard sub-lattices is compatible with the combination of system size, filling fraction, and hard-core constraint.

Fig. 4.8 shows the local density configuration in the SF and the solid limit. This choice of system size and filling fraction makes the open boundary conditions compatible with a checkerboard solid ground state because all of the lattice sites lying in the corners are occupied. To achieve this, the filling fraction needs to be larger than $\nu = 1/2$, and we fix it at $\nu = 46/91$.

Fig. 4.9 shows how the observables introduced in the previous sections behave in the transition from SF to solid. Compared to the system previously studied, at half filling and with cylindrical boundary conditions, the observables show a smooth change when increasing the interaction strength, suggesting that the transition is no longer of first order. There are no longer two equivalent checkerboard sub-lattices that break the Z_2 symmetry of the solid because only one sub-lattice is compatible with the larger-than-half filling fraction in the strong interaction limit. This further

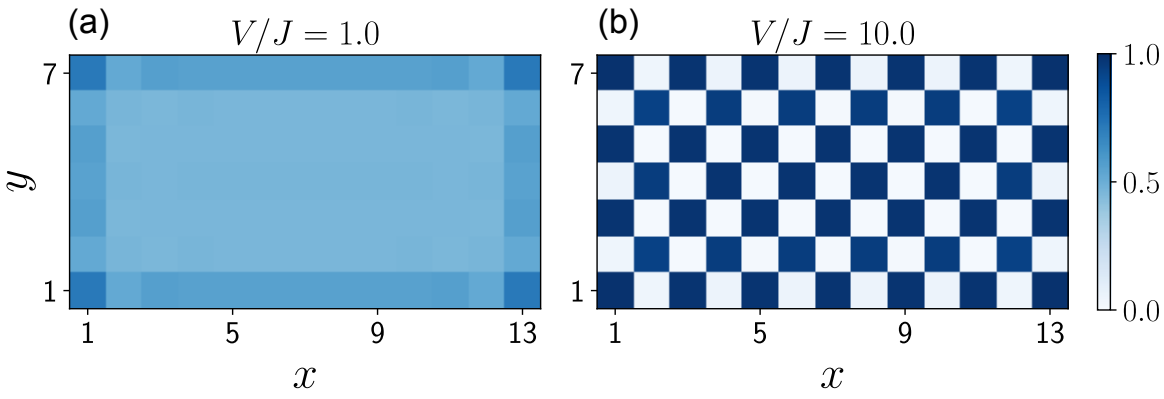


Figure 4.8: Local density $\tilde{n}_{x,y}$ for $V/J = 1$ (a) and $V/J = 10$ (b) for lattice size $L_x \times L_y = 13 \times 7$ with filling fraction $\nu = 46/91$ and OBC.

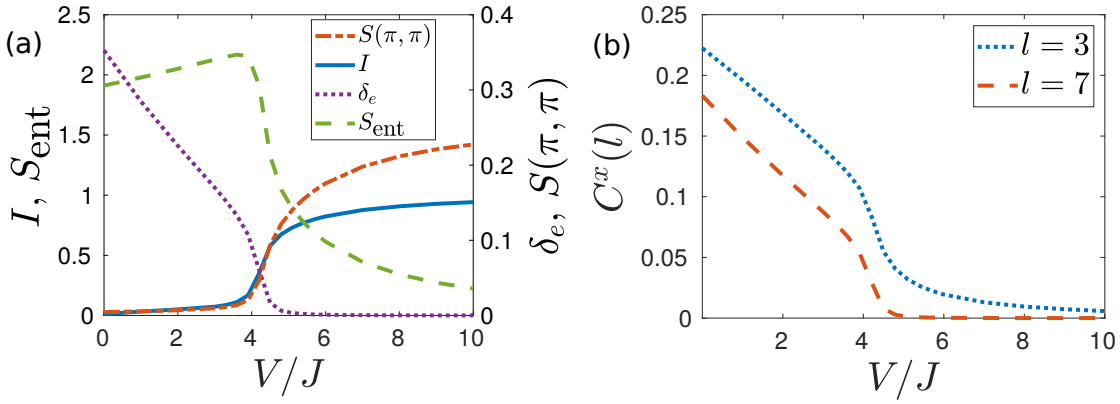


Figure 4.9: (a) Structure factor $S(\pi, \pi)$, occupation imbalance I, natural occupation number difference δ_e and entanglement entropy S_{ent} as a function of the interaction strength V/J for lattice size $L_x \times L_y = 13 \times 7$ and OBC at filling fraction $\nu = 46/91$. (b) $C^x(3)$ and $C^x(7)$ for the same system as (a).

indicates how, for the finite system, the lattice size and boundary conditions deeply affect the ground states and the type of transition.

To avoid the occurrence of domains in the system, while keeping the filling fraction at exactly $\nu = 1/2$, we employed cylindrical boundary conditions throughout our calculations.

4.3 Supersolidity triggered by one-particle doping

One of the most exciting predictions of Ref. [58] is the existence of a supersolid (SS) regime in the phase diagram of the dBH model.

Supersolid states are considered extremely relevant because they show superfluidity and solid order at the same time. In continuous systems, supersolidity appears when the two $U(1)$ symmetries associated to the translational invariance of a crystalline structure and to the global phase of the SF state are simultaneously broken [217, 218]. They were first predicted to appear when zero-point defects in ^{4}He condense without destroying the crystal structure at low temperatures [219, 220]. It was later observed [221, 222] that properties characteristic of superfluidity appeared in solid ^{4}He [223, 224, 225], although it was shown that the mechanisms originating the SS were different from the original proposal.

Lattice systems have been considered as promising candidates to study supersolidity using ultracold gases trapped in optical lattices. In lattice systems, the spontaneous breaking of translation invariance is defined with reference to the discrete translation symmetry of the Hamiltonian [218]. The SS states are realised by adding interstitials or vacancies to the solid phases at a commensurate filling fraction. The additional particles then form a Bose-Einstein condensate on top of the solid structure.

The mechanism explaining supersolidity in lattices can be understood using the concept of superflow paths [226]. Extra particles or holes added to a solid can hop around freely and create a Bose condensate. However, for the case where $\nu = 1/2$, the solid state is a checkerboard solid and in the hard-core limit, there are no nearest-neighbour free sites where an extra particle can move through. This means that the superflow is inhibited. In particular, it was shown that there is no supersolid state on the square lattice when only NN and NNN repulsive interactions are present [227]. The long-range tail of the dipolar interaction is needed to induce supersolidity [226].

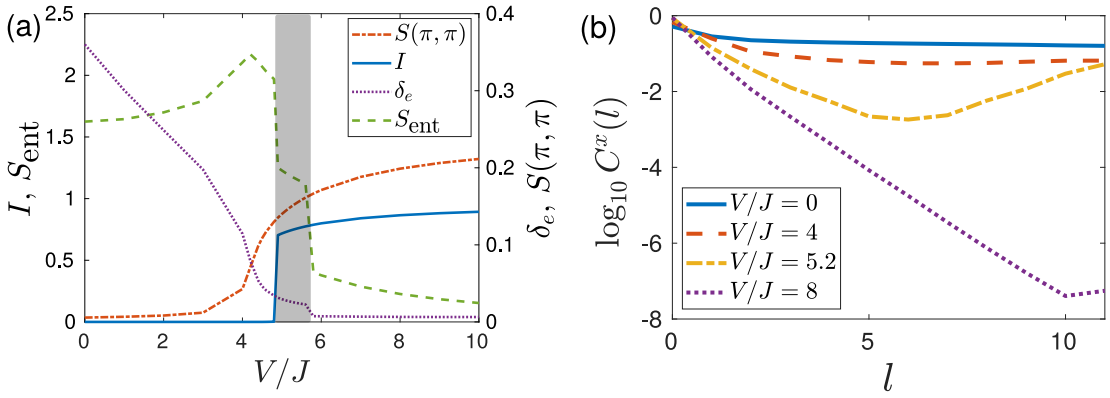


Figure 4.10: (a) Structure factor $S(\pi,\pi)$, occupation imbalance I, natural occupation number difference δ_e, and entanglement entropy S_{ent} as a function of the interaction strength V/J for lattice size $L_x \times L_y = 12 \times 6$ and filling $\nu = 37/72$. (b) Correlation functions along the cylinder $C^x(l)$ for four interaction strengths, starting from $x = 0$.

We explore whether the SS state can be detected in a small lattice system with a fixed number of particles by doping the checkerboard solid. The set of quantities we have defined in the previous sections allow us to detect the properties of the ground state that define the SS. In particular, we expect the SS state to simultaneously show off-diagonal long-range order characteristic of a SF and a density modulation typical of a solid.

We consider the lattice size $L_x \times L_y = 12 \times 6$ at half filling and add one additional boson, changing the filling fraction from $\nu = 1/2$ to $\nu = 37/72$. We study how the increased number of particles affects the ground state. Fig. 4.10 shows the summary of all of the observables we use to characterise solid and SF order. Between the SF and the solid regimes, we highlight a region with $4.9 < V/J < 5.8$ where the occupation imbalance and structure factor indicate solid order and the natural occupation number difference signals the presence of condensation. This region corresponds to a SS state. In the presence of the hard-core constraint, the extra particle added to system delocalises and condenses over the checkerboard solid formed by the remaining bosons. The natural occupation number difference δ_e shows a significant change

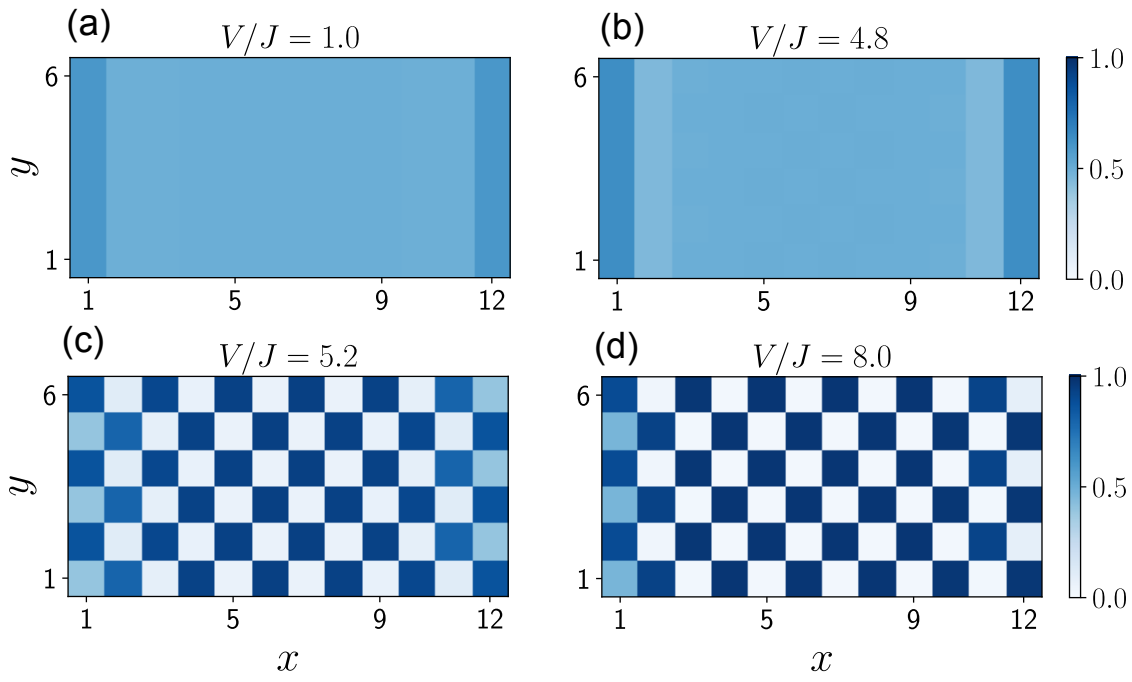


Figure 4.11: Local density $\tilde{n}_{x,y}$ for $V/J = 1$ (a), $V/J = 4.8$ (b), $V/J = 5.2$ (c) and $V/J = 8$ (d) for lattice size $L_x \times L_y = 12 \times 6$ and filling $\nu = 37/72$.

in behaviour compared to the half-filled case. Instead of abruptly falling to zero at the transition, it plateaus to $\delta_e \approx 0.025 \approx 1/37$ and then falls. This indicates that the extra particle condensates on top of the checkerboard pattern. In fact, because of the hard-core constraint, the extra particle cannot occupy any of the checkerboard sites occupied by the other particles. The density profiles of the system give further evidence of this mechanism. Fig. 4.11 shows the density profile $\tilde{n}_{x,y}$ for four values of V/J representative of the different ground states. In particular, in the SS regime, for $V/J = 5.2$, the density profile shows a combination of the checkerboard pattern and the SF behaviour where particles localise at both edges. In the large interaction limit, the one extra particle localises to one single edge of the system on top of the checkerboard solid.

The entanglement entropy is further able to capture the three distinct ground states of the system. Two discontinuous changes at $V/J \approx 4.9$ and $V/J \approx 5.8$ signal the presence of two transitions. This further suggests that S_{ent} is a good quantity

to determine the presence and location of the transitions between SF and SS and between SS and solid.

As an additional measure of long-range order, we observe the behaviour of the correlation functions in the three regimes. Fig. 4.10 (b) shows the decay of the correlation function $C^x(l)$, starting from the left edge of the cylinder at $x = 0$ and reaching the right edge. In the SF and solid regimes, the correlations functions decay algebraically and exponentially respectively, as they did for the undoped system at half filling. In the SS state, however, $C^x(l)$ shows a peculiar behaviour as its decay is non-monotonic. It starts decaying in a fashion close to exponential but then has a resurgence when reaching the opposite edge of the cylinder, showing a final value reminiscent of the SF regime. This behaviour indicates the existence of long-range correlations between the bosons at both edges.

To further explore this behaviour, we simultaneously look at the density profiles and correlation functions along the y direction. Fig. 4.12 (a-c) shows the local density $\tilde{n}_{x,y}$ for three representative values of the interaction strength V/J where the system is in the SF, SS and solid regime respectively. As previously mentioned, the one extra particle in the system occupies the lattice in a different way in each regime. In the SS regime, for $4.9 \lesssim V/J \lesssim 5.8$, it equally occupies the two edges of the cylinder. In the solid regime, for $V/J \gtrsim 5.8$, it occupies only one. This preferential occupation of the edges suggests that phase separation is occurring in the system, meaning that the ground state is solid in the bulk of the system and it is in a SS state at the edges. The phase separation is induced by the open boundary conditions in the x directions which encourage the extra particle to inhabit the edge sites of the lattice because of the lack of interaction energy from one of the sides. This energetic effect is expected to play a role also in experiments on finite lattices, although it could be reduced with the addition of an external harmonic trapping potential, which we do not consider in our system.

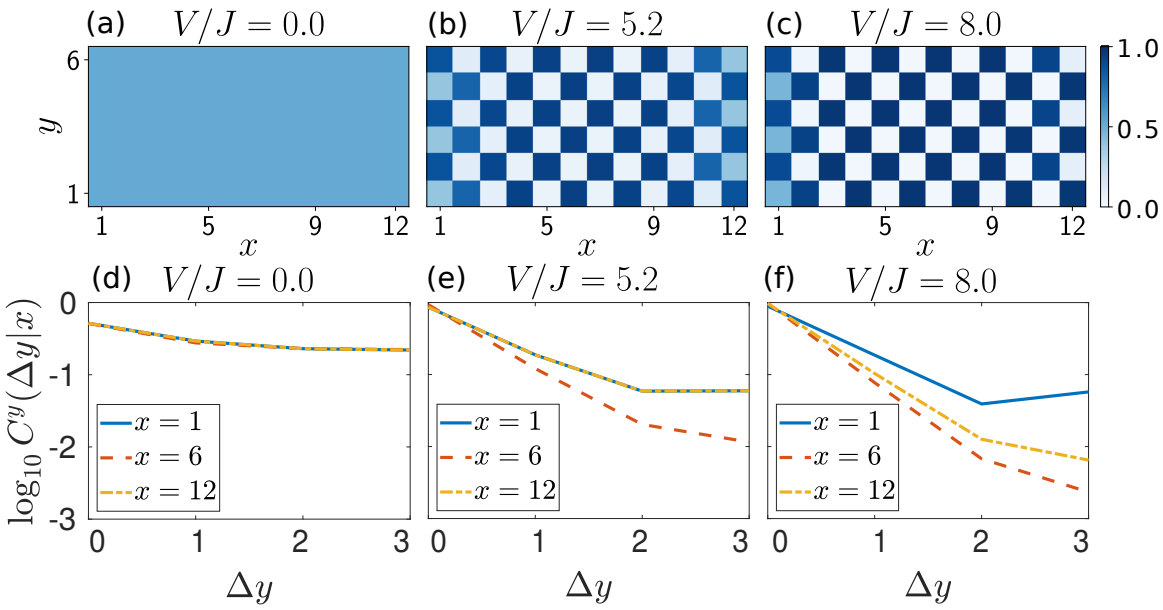


Figure 4.12: (a-c) Local density $\tilde{n}_{x,y}$ for three representative values of the interaction strength V/J for lattice size $L_x \times L_y = 12 \times 6$ at filling $\nu = 37/72$. (d-f) Correlation functions along the circumference of the cylinder $C^y(\Delta y|x)$ for the same system size and interaction strengths. Each line represents a separate x coordinate.

Throughout the lattice, both in the SS and solid regions, the local density indicates the presence of a periodic modulation characteristic of solid order. To establish that the state located at the edge is SS, we calculate the correlation functions in the y direction as a measure of long-range order. We define the correlation around the cylinder at a fixed value of x as

$$C^y(\Delta y|x) = \langle b^\dagger_{x,y_0} b_{x,y_0+\Delta y} \rangle, \tag{4.8}$$

where, because of the PBC in y, Δy goes from 0 to $L_y/2$ and y_0 is chosen such that site (x, y_0) belongs to the occupied checkerboard sub-lattice.

Since the phase separation occurs at a fixed x, $C^y(\Delta y|x)$ is be able to discriminate between the different states. Fig. 4.12 (d-f) shows $C^y(\Delta y|x)$ for $x = 1$ and 12, representing the left and right edge respectively, and for $x = 6$, representing the bulk of the system, for three values of V/J in the SF, SS and solid regime. In the SF

regime, shown in Fig. 4.12 (d), the correlation decays similarly in the bulk and at the edges, showing a decay of around an order of magnitude and indicating the presence of long-range order. In the solid regime, shown in Fig. 4.12 (f), a slower decay is observed only at the value of x, which is occupied by the extra particle. For the other values of x, both in the bulk and at the remaining edge, the decay is faster and the correlation drops almost two orders of magnitude more as compared to the first edge. Finally, in the SS regime, shown in Fig. 4.12 (e), there is a distinction in the decay of the correlations between the edges and the bulk. The correlation in the bulk decays almost an order of magnitude more than at the edges, which decay by around one order of magnitude.

The change in behaviour of the correlation functions in correspondence to the edges populated by the extra particle denotes the simultaneous presence of ODLRO and density modulation. This indicates that the state close to the edge is a SS. The resurgence of the correlation function in the x direction also suggests that the two SS states at the edges are correlated. The existence of the long-range correlation explains why, for $4.9 \lesssim V/J \lesssim 5.8$, the δ_e has a non-zero value.

To investigate whether the occurrence of this SS state is a finite-size effect, we have considered a system at the same filling fraction $\nu = 37/72$ and size $L_x \times L_y = 24 \times 6$. The behaviour of the local density and of the correlation functions along the y direction are similar to those shown in Fig. 4.12. The two extra particles localise on opposite edges for values of V/J where the SF disappears, and the correlation functions in the y direction indicate the presence of SS order localised at the edges. However, there is a lack of simultaneous presence of solid order indicated by a non-zero value of the structure factor $S(\pi, \pi)$ and superfluidity indicated by a non-zero δ_e. Additionally, for no value of V/J does the correlation function along x between the two edges show a resurgence indicating ODLRO. The two edges for the 24×6 system are not correlated and there is ODLRO only in the y direction, which is not captured

by the δ_e or the entanglement entropy which is obtained by cutting the system along the circumference. This statement is confirmed by all of the other observables we have computed, and indicates a transition from a SF to a solid, analogue to the one present in the $L_x \times L_y = 12 \times 6$ system at filling $\nu = 1/2$.

To further study the stability of the SS state, we have considered the $L_x \times L_y = 12 \times 6$ system at half filling after removing one particle. The system did not show evidence of a SS state. Neither did the same system size with the addition of two particles. The results in Ref. [58] predicted SS for both hole and particle doping and our calculations are not compatible with such a statement. However, our system has two different features. On the one hand, the system we have studied has a small size and the presence of finite edges, which induce significant finite-size and boundary effects. On the other hand, the range of the dipole interaction we consider is cut off at five nearest neighbours. Our choices for the properties of the system have the goal of describing an experimental implementation of the system, where only few particles are present and the long-range tail of the interaction are washed out by temperature effects. Calculations using quantum Monte Carlo methods where the range of the interaction has been cut after few sites have also found the SS phase to be mechanically unstable [228, 229]. From this analysis, we conclude that the long-range correlation we have found between the two edges in the 12×6 system with one-particle doping is a finite-size effect, which may render its observation challenging in experimental setups, even at nK temperatures.

4.4 Star solid

Lower filling fractions are associated with different density modulation patterns in the strong interaction limit, where the phase is solid. Quantum Monte Carlo simulations have shown the existence of a Mott lobe with filling fraction $\nu = 1/4$ and a

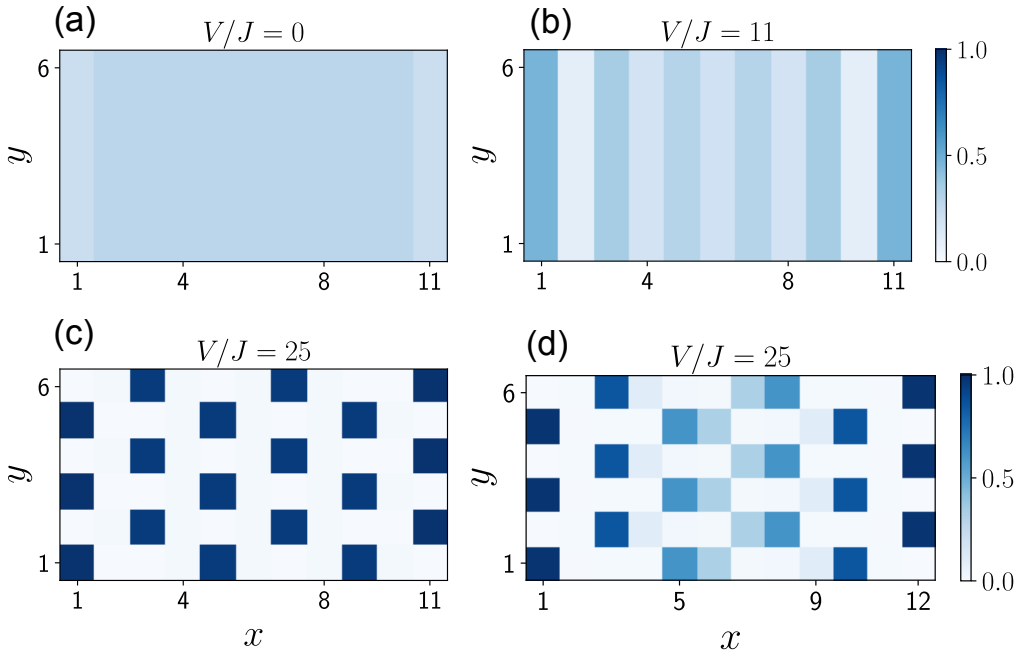


Figure 4.13: Local density $\tilde{n}_{x,y}$ for $V/J = 0$ (a), $V/J = 11$ (b), $V/J = 25$ (c) for lattice size $L_x \times L_y = 11 \times 6$ and filling $\nu = 3/11$. (d) $\tilde{n}_{x,y}$ at $V/J = 25$ for lattice size $L_x \times L_y = 12 \times 6$ and filling $\nu = 1/4$.

corresponding solid phase named star solid [58]. We explore how this phase is affected by the finite system size. On the finite cylinder geometry, the effect of the boundaries severely modifies the ground state. Let us consider a system size where both L_x and L_y are even. The cylinder circumference L_y needs to be even in the presence of cylindrical boundary conditions, in order to avoid frustration effects. Unlike in the checkerboard solid, choosing an even value for L_x introduces strong boundary effects for the star solid. Fig. 4.13 (d) shows what happens in the large interaction strength limit. The bosons preferentially populate the sites at the edge sites of the lattice. Therefore, the star solid order gets pinned at both edges of the system and propagates towards the centre from both directions. When L_x is even, the two solid order patterns do not match in the centre and the lattice does not support a star solid pattern across the whole lattice.

To combine the effect of the boundaries with the solid density pattern, it is nec-

essary to tune L_x in such a way that the occupied lattice sites in the star solid fall exactly at the edges of the system. To observe the star solid in our finite system, we need to consider an odd value of L_x and an adjusted filling fraction. We choose a system with size $L_x \times L_y = 11 \times 6$ and filling fraction $\nu = 3/11$. Fig. 4.13 (a-c) shows the density $\tilde{n}_{x,y}$ of the ground state for three representative values of the interaction strength in the SF, immediately before the transition and in the solid limit.

To characterise the transition from SF to star solid, we use the set of observables we have previously defined for the checkerboard solid. Fig. 4.14 shows the structure factor $S(\pi, 0)$, the occupation imbalance I, the natural occupation number difference δ_e and the entanglement entropy S_{ent}. All of the observables indicate a transition from SF to star solid at $V/J \approx 12$. Since the solid pattern is different from the checkerboard one, the structure factor is computed at $(k_x, k_y) = (\pi, 0)$ and the occupation imbalance is defined as

$$I = \left| \frac{1}{N} \left(\sum_{i \in star} n_i - (1 - \nu) \sum_{i \notin star} n_i \right) \right| . \tag{4.9}$$

It has value 0 when the density is uniform and has value 1 when the star solid pattern is present. The structure factor has value $S(\pi, 0) = \nu^2 \approx 0.075$ in the thermodynamic limit and we observe this value for a large interaction strength even in our finite system. The occupation imbalance shows a sharp transition at $V/J \approx 12$. However, before the transition it increases steadily instead of staying at zero value: this happens because the density of the system does not remain uniform while increasing the interaction strength, but has a density wave pattern along the x direction while remaining uniform along y. Once again, the entanglement entropy S_{ent} proves to be a good indicator of the position of the transition.

We conclude that the ground state of the system for the filling $\nu = 1/4$ is highly sensitive to the boundary conditions and system size parameters, and that the size and filling fraction of the system need to be properly tuned to observe a star solid.

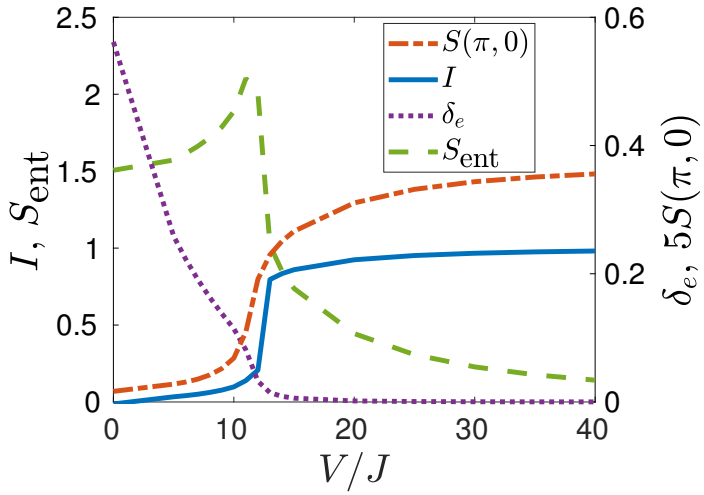


Figure 4.14: Structure factor $S(\pi, 0)$, occupation imbalance I, natural occupation number difference δ_e, and entanglement entropy $S_{\rm ent}$ as a function of the interaction strength V/J for lattice size $L_x \times L_y = 11 \times 6$ and filling $\nu = 3/11$.

4.5 Machine learning approach

In the previous sections we have demonstrated how the structure factor $S(k_x, k_y)$, the occupation imbalance I, the correlation functions $C^x(l)$, the natural occupation numbers difference δ_e and the entanglement entropy $S_{\rm ent}$ allow us to identify the SF, SS and solid states. The advent of quantum gas microscopes gives access to detection methods with single-site resolution [99, 100, 230]. We, therefore, explore the question of whether an experiment that only measures the local density at each lattice site can discriminate between the states, and if further information can be extracted from the density measurements.

We tackle this problem by employing unsupervised machine learning techniques. Both unsupervised and supervised learning methods have proven to be effective in recognising phases of matter and identifying phase transition points in several physical systems [231, 232, 233, 234, 235, 236, 237]. Supervised learning methods are trained on previously labelled data sets in order to draw conclusions regarding new data. Unsupervised methods, on the other hand, are used to derive insights into the fea-

tures of the systems without any prior knowledge of the underlying system properties. Principal component analysis (PCA) has proven to be a powerful unsupervised learning method with the ability to recognise different types of order, symmetry breaking and also identify transition points [232, 238]. This is the method we use in the next section.

4.5.1 Principal component analysis

Let us briefly describe how PCA works [239]. Let us consider a matrix A where each row represents a data sample and each column represents a feature associated with the sample. The values of the features have been centred, meaning that the mean of the feature over the samples has been subtracted from their original value. PCA performs an orthogonal transformation on the matrix A. It transforms the set of initial features, which are potentially correlated, to a new set of uncorrelated features. These new features are called principal components (PC). The PC are labelled in decreasing order, according to the amount of variance they represent between the data. The first PC of a set of features is the linear combination of such features with the largest variance throughout all of the samples. Each following PC has the largest variance with the condition that it is orthogonal to all of the previous PC. The resulting set of PC vectors forms an uncorrelated orthogonal basis.

The linear transformation that PCA implements reads $B = AW$. By considering the orthogonal transformation as made of column vectors $W = (w_1, w_2, \ldots, w_n)$, then w_i is the weight of the PC in the configuration space. The set of w_i are obtained by solving the eigenvalue problem:

$$A^T A w_i = \Lambda_i w_i \,, \tag{4.10}$$

where the eigenvalues Λ_i are real numbers sorted in decreasing order, such that $\Lambda_1 \geq$

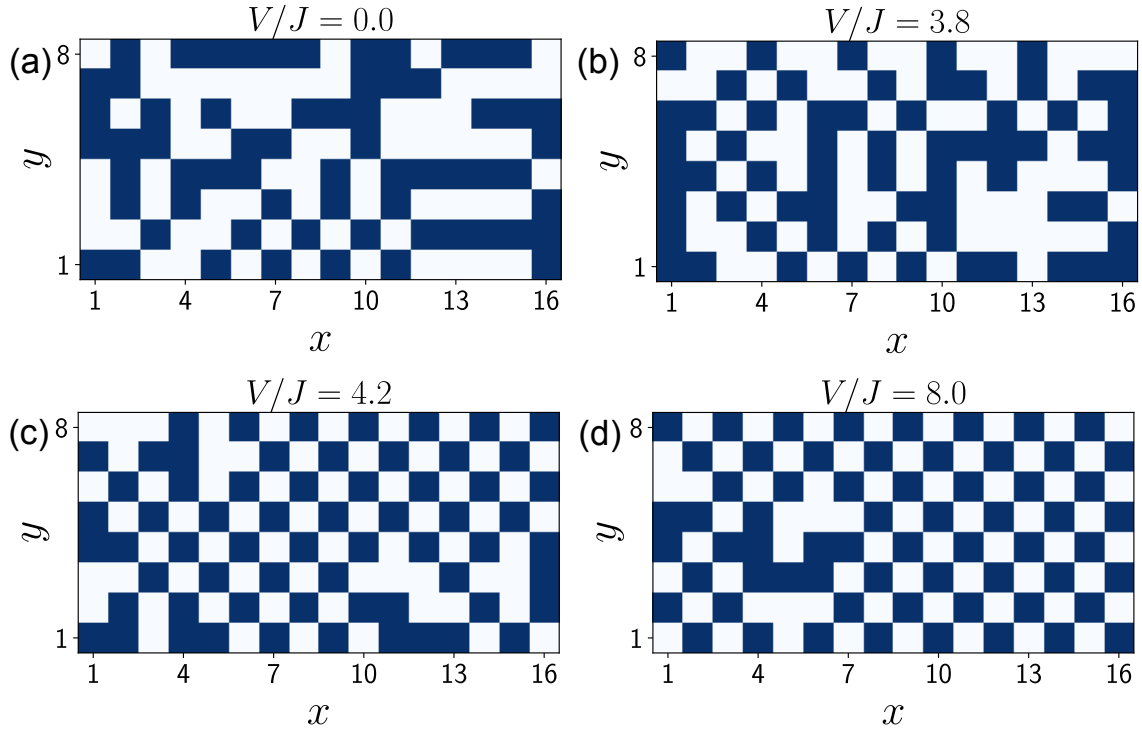


Figure 4.15: Four instances of the simulated sampling obtained for lattice size $L_x \times L_y = 16 \times 8$ at filling $\nu = 1/2$. A blue square represents a measurement of the lattice site resulting in finding a particle. A white square represents a measurement of the lattice site resulting in finding no particle. The four plots represent instances in the SF (a) and solid regime (d), and immediately before (b) and after (c) the transition.

$\Lambda_2 \geq \ldots \Lambda_n \geq 0$. The magnitude of the eigenvalues represents the amount of variance of the original data in the direction of each of the PC.

4.5.2 Simulated measurement results of density configurations

The development of quantum gas microscopes has allowed experiments to detect particles in a lattice with single-site resolution. We want to replicate the results of the measurement of the occupation number in each site to get a set of density configurations. In-situ detection is experimentally achieved by increasing the lattice depth, thereby freezing the density distribution of the gas. Then fluorescence imaging is used to obtain the parity of the occupation of each site [240]. This procedure is

destructive for the many-body state, however, in addition to the particle density, the measurement is able to capture fluctuations and correlations in the system. For the case of hard-core bosons, the measurement of the parity is equivalent to observing the presence or absence of a boson in each site.

We replicate the outcomes of this type of measurement by considering the ground-state wavefunctions obtained from our DMRG calculations and numerically simulating a sequence of projective measurement at each site. The numerical procedure we implement works as follows. We calculate the expectation value of the number operator in the first site: n_1. We simulate the outcome of a measurement resulting in finding a boson at this site with probability n_1. Depending on the outcome of the measurement, we project the ground-state wavefunction onto the subset of the Hilbert space compatible with the measurement outcome. This sequence of measurement and projection is repeated for each site until all of the lattice sites have been measured. This simulated measurement protocol leads to obtaining an occupation pattern for the lattice which takes the correlations between particles into account, as achieved in [240].

We start with a lattice size of $L_x \times L_y = 16 \times 8$ at half filling. Four sample configurations representative of the system in the SF and solid regime and immediately before and after the transition are shown in Fig. 4.15. A cursory look at the configurations shows how the checkerboard pattern becomes apparent after the transition and how, in the SF state, where the density is uniform, the configuration appears random. We generate 2000 such particle configurations for the whole range of interaction strengths.

We perform a PCA on the set of sample configurations we have generated. For each particle configuration, we turn the set of $L_x \times L_y = 16 \times 8$ local-density values into a 128-feature vector, which becomes the set of features which describe each data sample. The set of all feature vectors for all configurations is fed to the PCA algorithm. Each

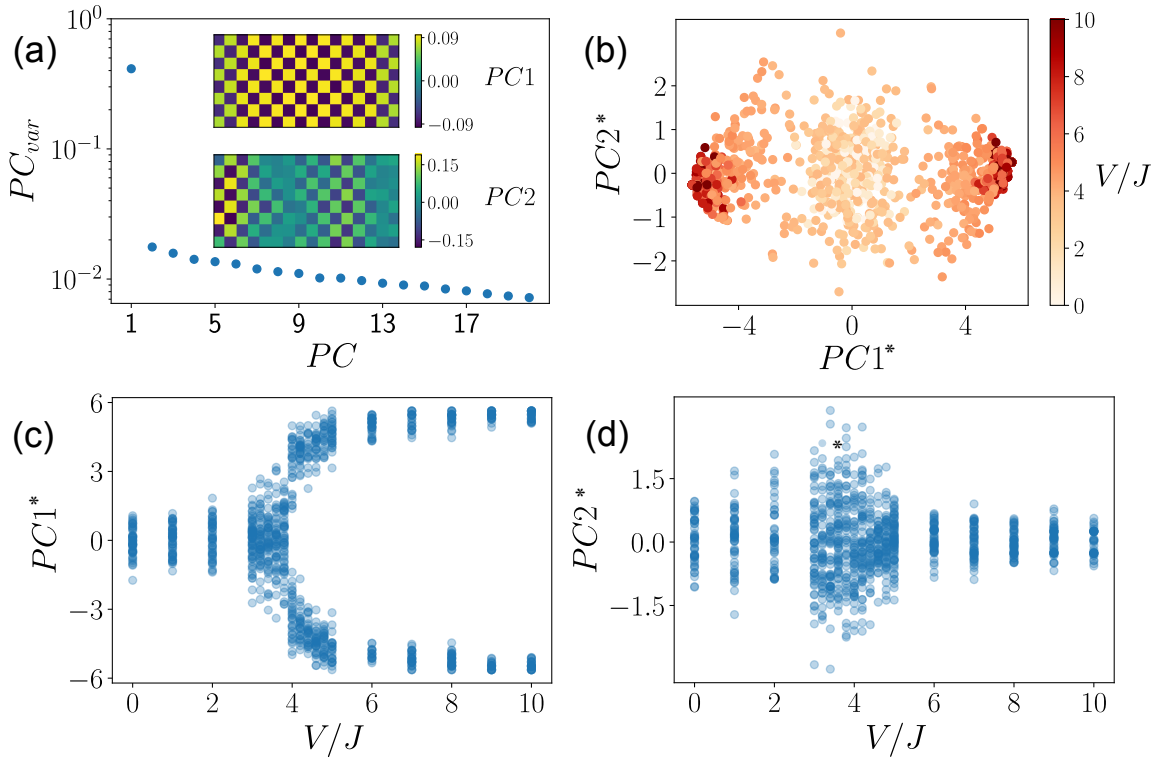


Figure 4.16: Summary of the PCA of the simulated samples for lattice size $L_x \times L_y = 16 \times 8$ at filling $\nu = 1/2$. (a) Fraction of the variance PC_{var} of the first 20 PC. The inset shows the representation of the first two PC. (b) Distribution of the samples when projected on the first and second PC. Each data point is colour-coded according to the interaction strength. (c) Projection on the first PC as a function of the interaction strength V/J. (d) Projection on the second PC as a function of the interaction strength V/J.

data sample is also characterised by a control parameter, the interaction strength V/J in this case, which is not used in PCA but is just kept as a label for the samples.

First, we want to determine whether PCA is able to separate the sample configurations according to their state. Secondly, we want to obtain the equivalent of an order parameter to locate the transition and give it a physical interpretation.

A summary of the results of the PCA is shown in Fig. 4.16. Fig. 4.16 (a) shows the fraction of the variance PC_{var} in the configuration samples captured by the first 20 PC. The values of PC_{var} are normalised so that they sum to one. A single principal component, $PC1$, is dominant and resolves 41% of the variance. The next PC are

at least one order of magnitude less significant. This implies that the samples vary significantly over a single PC. We can understand this by looking at the spatial representation of the first two PC which are shown in the inset of Fig. 4.16 (a). The first PC reproduces the occupation imbalance in the lattice. The second PC does not capture any evident property of the density pattern although it picks up parts of the checkerboard pattern. The principal components are orthogonal and have unit norm.

Projecting the configurations in the subspace generated by the first two PC shows the formation of three clusters, shown in Fig. 4.16 (b), where PC1* and PC2* indicate the coefficient of the of the corresponding component in the decomposition. The central cluster is composed of the configurations corresponding to the SF state. This is indicated by the colour coding of the points according to their corresponding interaction strength. The two clusters at the left and right correspond to the checkerboard solid state at a large interaction strength. Each of the two checkerboard solid clusters represents the occupation of one of the two equivalent checkerboard sub-lattices. Fig. 4.16 (c) shows the dependence of the projection of the data points on PC1 as a function of the interaction strength V/J. A single branch at small values of V/J, corresponding to the SF regime, splits off into two sub-branches after crossing the transition point. Each branch indicates the population of one of the two sub-lattices. PC1* precisely pinpoints the value of the interaction where the transition happens. In agreement with the other observables calculated in the previous section, it points to a critical value of the transition at $V/J \approx 3.9$. The same plot for PC2 is much less informative since it shows no evident change in behaviour before and after the transition. From its spatial representation, we know that it is related to the checkerboard pattern in some region of the lattice, but it still does not add relevant information to discriminate between the states. An equivalent plot for PC3, which shows a comparable fractional variance as PC2, gives no additional insights and still captures the checkerboard pattern in a sub-region of the lattice.

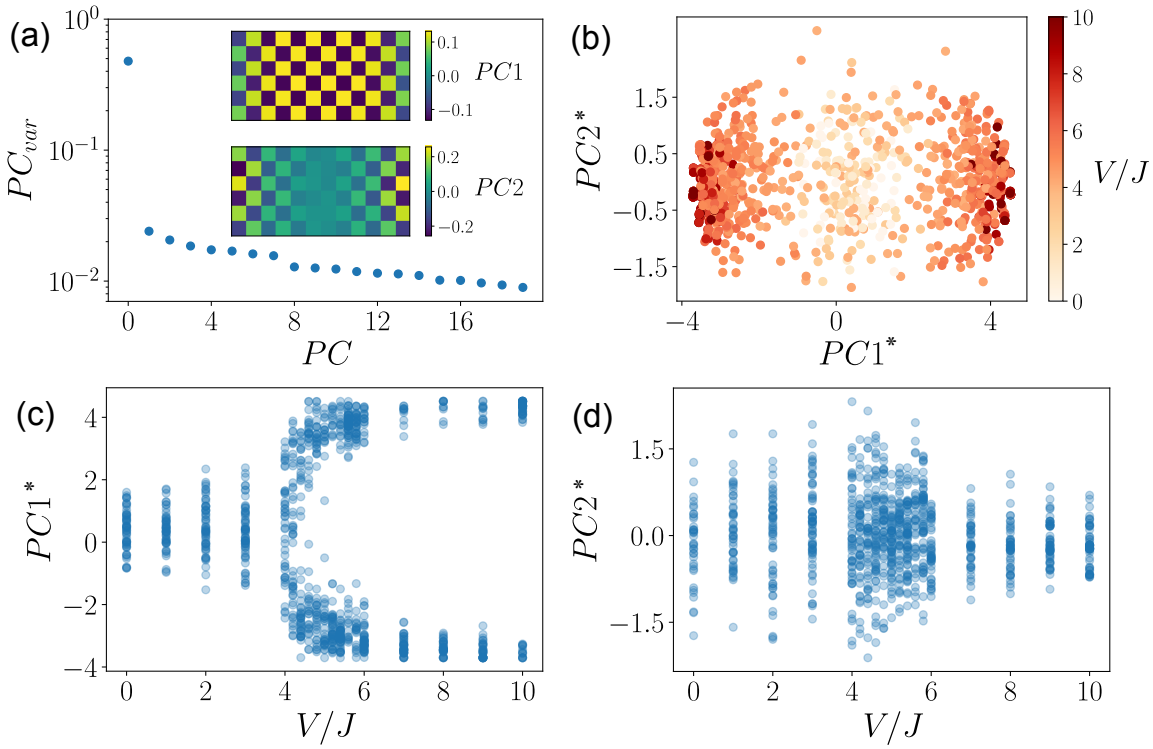


Figure 4.17: Summary of the PCA of the simulated samples for lattice size $L_x \times L_y = 12 \times 6$ at filling $\nu = 37/72$. (a) Fraction of the variance PC_{var} of the first 20 PC. The inset shows the representation of the first two PC. (b) Distribution of the instances when projected on the first and second PC. Each data point is colour-coded according to the interaction strength. (c) Projection on the first PC as a function of the interaction strength V/J. (d) Projection on the second PC as a function of the interaction strength V/J.

We, therefore, conclude that the PCA of the density configurations allow us to separate the samples corresponding to the SF and solid states. Moreover, the first PC is able to capture the relevant order parameter for the system, the occupation imbalance, and can be used to pinpoint the value of V/J for which the transition occurs.

Having successfully applied PCA to the half filling case, we explore whether the density configuration information is sufficient to identify the supersolid state of the system doped with one additional particle. We consider the system with size $L_x \times L_y = 12 \times 6$ and filling fraction $\nu = 37/72$, and perform a PCA on the configuration samples.

A summary of the results of the PCA is shown in Fig. 4.17. The results of the PCA is similar to those for the half-filled system. Fig. 4.17 (a) shows how the dominant PC accounts for most of the variance between samples. The insets show how PC1 captures the occupation imbalance while PC2 represents boundary effects. The three clusters in Fig. 4.17 (b) correspond to the SF state at low interaction V/J and to states with solid order at large V/J. Overall, neither PC1 nor PC2 allow for the separation of the SS state from the solid state. The one extra particle present in the system increases the occupation of the empty sites in the checkerboard pattern; however, this effect is not picked up by the PCA in this finite-size system where the boundaries have a considerable effect. We, therefore, conclude that the use of density information is not sufficient to identify the SS state and separate it from the checkerboard solid. This is in agreement with the notion that long-range coherence information is needed to characterise supersolidity.

4.5.3 PCA of the Schmidt values

In the previous section, we have seen how PCA is able to achieve two different goals. On the one hand, it can separate the data samples into clusters that present similar features, as shown in the $PC1^*$-vs-$PC2^*$ plots. On the other hand, it can also extract the relevant order parameters from the data it is fed, allowing to separate between states.

We focus on this second property of PCA as a way to extract information about the transition using quantities we have computed with our DMRG calculations. In particular, we consider the set of Schmidt values that we have used to compute the entanglement entropy in Section 4.2.3. The set of Schmidt values constitutes the entanglement spectrum that has been shown to contain information about the phase of the system [94]. Although the Schmidt coefficients are not experimentally available, they are typically obtained in numerical simulations and we use PCA on the Schmidt

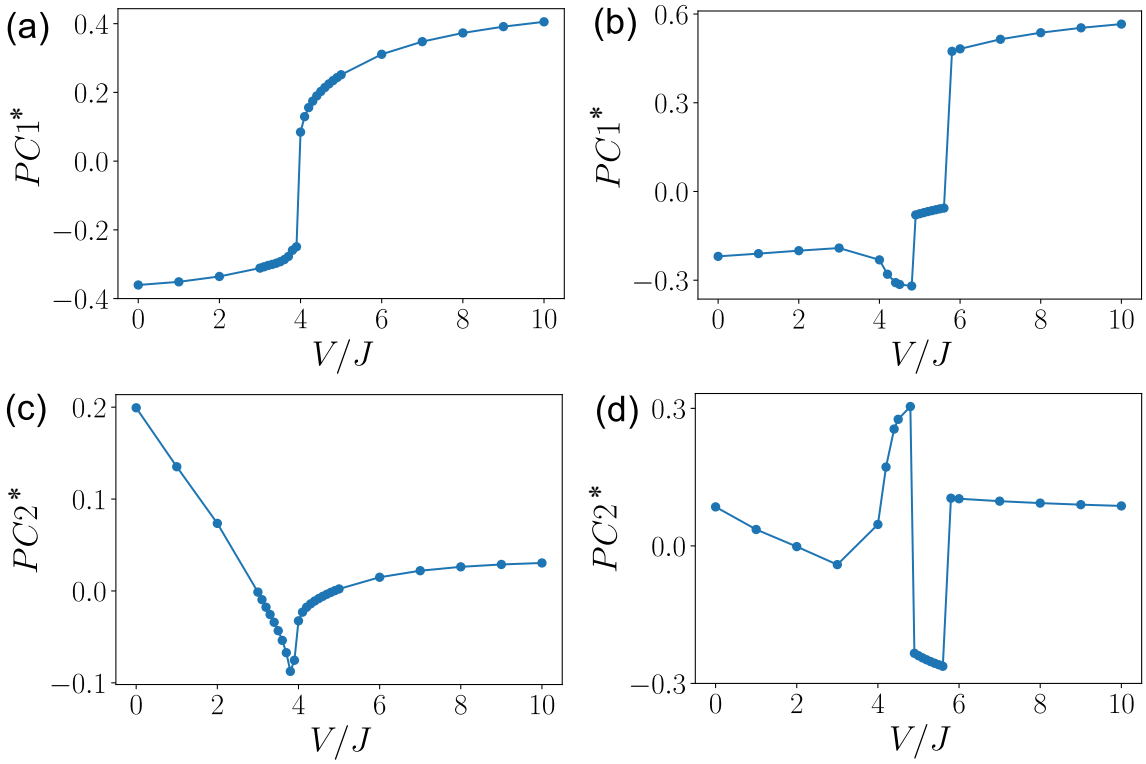


Figure 4.18: (a,c) Projections on the first and second PC from the PCA of the Schmidt values as a function of the interaction strength V/J for lattice size $L_x \times L_y = 16 \times 8$ at filling $\nu = 1/2$. (b,d) Projections on the first and second PC from the PCA of the Schmidt values as a function of the interaction strength V/J for lattice size $L_x \times L_y = 12 \times 6$ at filling $\nu = 37/72$.

coefficients to extract an order parameter that helps to discriminate between states supported by the system.

We consider the Schmidt values obtained by cutting the cylinder in two equal parts for the $L_x \times L_y = 16 \times 8$ at filling fraction $\nu = 1/2$. For each value of the interaction strength V/J, we use the Schmidt coefficients λ_i in decreasing order as the set of features for the PCA. Fig. 4.18 (a,c) shows the first two PC projections as a function of V/J. PC1* shows a sharp change in correspondence to the transition point and its behaviour is reminiscent of the order parameter for a first-order transition. PC2* shows a cusp at the same position; however, we did not find a direct physical interpretation for it. Both quantities are able to pinpoint the value of the

interaction where the transition happens, in complete agreement with all of the other observables we have calculated using DMRG. This suggests that the set of Schmidt values contains information which is sensitive to the state of the system and can be used to discriminate between them. The PCA is able to extract this information as the first and second PC.

Following the same steps, we perform the PCA for the systems of size $L_x \times L_y = 12 \times 6$ doped with an extra particle to see if the additional SS state can be distinguished. Fig. 4.18 (b,d) shows PC1* and PC2* as a function of V/J. Three separate regimes can be distinguished, more directly from PC1*, corresponding to the SF, SS and solid states respectively, in agreement with the analysis performed in the previous sections.

It is worth noticing a similarity between the PC1* and the inverse of the entanglement entropy shown in Fig. 4.10. This similarity is less precise for the half-filled system where PC1* grows monotonically, but $1/S_{\text{ent}}$ does not. This suggests that there is not a 1-to-1 relationship between the PC1* and the entanglement entropy.

We have therefore shown how the PCA of the Schmidt values offers valuable insight into defining the location of the transition. It is also able to extract information which is not directly related to standard quantities derived from it such as the entanglement entropy. We propose the use of PCA analysis of the Schmidt coefficients in numerical simulations as an additional tool to pinpoint where the transition occurs. This can be a starting point for determining what the relevant parameter range is to investigate the transitions of strongly-correlated systems.

4.6 Conclusion and outlook

The implementation of Hamiltonians characteristic of condensed matter physics using ultracold gases in optical lattices has allowed for the exploration of previously unavail-

able physical regimes. The different way in which these systems are experimentally realised raises the question of what the best observables are to characterise the phases supported by the system. Often, numerical studies of such systems use quantities that come from condensed matter physics, and cannot always be experimentally realised in an optical lattice setting.

To draw a connection between numerical calculations and experimentally available quantities, we have calculated a set of observables available in either setting to characterise the solid and SF states present in the dBH model. Our focus on a finite geometry and a fixed number of particles is in line with current experimentally available setups for ultracold dipolar molecules in optical lattices. We compared the structure factor and the occupation imbalance as order parameters for the solid state of the system. They both capture the density modulations typical of solid order and we concluded that the imbalance is less sensitive to finite-size effects and more robust as compared to the structure factor. Additionally, the imbalance is directly measurable in experiments whereas the structure factor is typically used in numerical calculations.

We showed how the transition from SF to solid is additionally characterised by the condensate fraction, which is an order parameter for superfluidity accessible in experiments. The off-diagonal long-range order typical of a SF is further confirmed by the behaviour of the decay of the correlation functions. We conclude that the imbalance and the condensate fraction, which are both observables available in ultracold gas experiments, are well suited to characterising the transition of the dBH model, even for small system sizes. Moreover, when doping the half-filled system with an extra particle, they are able to identify a SS state. The observation of supersolidity is particularly sensitive to finite-size effects and boundary effects in the system. This may cause its detection in finite-size experiments to be challenging. This degree of sensitivity may be connected with the results of quantum Monte Carlo

studies of the stripe phase at filling $\nu = 1/3$ leading to opposing conclusions on its stability in the thermodynamic limit [217, 241]. We attribute our results to a combination of the boundaries and the repulsive interactions which induce the particles to energetically favour the edges of the system. The addition of an external harmonic trapping potential may be able to compensate for this effect. Recent work concerning a highly-magnetic atom gas in the absence of a lattice potential but in the presence of a harmonic trap has indicated that the SS phase is not significantly affected by finite-size effects [242]. It would therefore be an exciting direction for future research to explore the effect of a harmonic trap on the stability of the SS state. We have additionally shown how the calculation of the entanglement entropy helps to pinpoint the location of the transitions, even offering insight into the correlation properties of the ground states.

Drawing inspiration from recent progress in using machine learning methods to identify phase transitions, we used principal component analysis as an unsupervised learning method on simulated experimental measurements of the occupation of single sites in the lattice to find out whether they are sufficient to discriminate between the states of the system. PCA is able to differentiate between the SF and solid state of small systems and captures the occupation imbalance as the natural order parameter for the transition. We observed that PCA of the density configurations could not identify the SS state when used on the system with one-particle doping. This conclusion agrees with the expectation that density measurements do not contain sufficient information to properly characterise the SS state. Long-range coherence information is necessary to identify superfluidity, which is not available solely from density measurements.

Finally, we have shown how performing PCA on the Schmidt coefficients obtained from our DMRG calculations gives additional information on the phase diagram of a strongly-correlated system. We observed that PCA can be used to extract information

which is not directly connected to other well-known physical quantities such as the entanglement entropy and helps to determine the position of the transition.

Exploring in more detail the scaling properties of the entanglement entropy with the system size would be a fruitful avenue to continue this research and to obtain more information on the phases supported by the system.

Chapter 5

Conclusion and outlook

We end this thesis by recalling the main topics we have discussed and the results we have obtained before mentioning some further directions of research.

In this thesis, we have applied the density matrix renormalisation group (DMRG) algorithm, based on matrix product states (MPS), to study strongly-correlated two-dimensional lattice systems on a finite geometry. A necessary part of using DMRG to study 2D systems is representing their Hamiltonian as a matrix product operator (MPO). In Chapter 2 we described in detail how to build the MPO for strongly-correlated 2D long-range interacting lattice Hamiltonians. We used the finite-state automata method and applied it to derive the MPO for an interacting Harper-Hofstadter model and a dipolar Bose-Hubbard model. We analysed in detail how the construction of the MPO is affected by the 2D-to-1D mapping necessary to model a 2D system using MPS, the periodic boundary conditions and the long-range terms in the Hamiltonians. We obtained a general code that can be used to implement a large variety of physical models, both fermionic and bosonic, in the presence of artificial gauge fields and with site and range-dependent interactions.

In Chapter 3, we applied DMRG to calculate the ground states of a bosonic fractional quantum Hall system on a finite cylindrical lattice. The choice of a finite

cylindrical geometry gives access to physical edges. Quantum Hall physics is characterised by a different behaviour of the edges of the system as opposed to the bulk. In particular, we have calculated the currents around the cylinder to find the presence of an insulating bulk and a conducting edge. Additionally, the correlation functions show a power-law decay when close to the edges as opposed to an exponential decay in the bulk. We used currents and correlation functions as a way of comparing the grounds state properties of the system with those described by the Laughlin wavefunction defined in the continuum, and found them to show compatible physical properties. Moreover, we computed the topological entanglement entropy of the ground state and showed how the system supports a topologically ordered phase. Finally, we showed how the fractional quantum Hall ground state is reached by increasing the interaction strength in the system and showed that the density of magnetic flux in the lattice strongly affects the transition.

In Chapter 4, we calculated the ground states of a dipolar Bose-Hubbard model on a finite lattice as a function of the dipolar interaction strength. We systematically calculated a set of observables to explore the transition from a superfluid to checkerboard solid, for finite-size lattice systems at half-filling. We found that, for small lattices, the occupation imbalance is better at identifying solid order as compared to the structure factor, which is more sensitive to finite-size and boundary effects. When doping the half-filled system with an extra particle, we found a region of the interaction strength where the ground state shows both off-diagonal long-range order and solid order, typical of a supersolid phase. However, this phase does not survive when changing the number of particles in the system or for larger system sizes, indicating that the supersolid phase is very sensitive the specific system parameters and thus difficult to observe. Additionally, by making use of unsupervised machine learning techniques, we have shown how simulated density measurements from a quantum gas microscope can be used to discriminate between solid and superfluid states of a

dipolar Bose-Hubbard model at half-filling.

The numerical results of this thesis, for finite-size lattice systems, aim at providing experimentalists with insights into which states can be observed in small lattice systems with few tens of particles.

A possible direction of further investigation for the dipolar Bose-Hubbard system is to study the phase transition when the dipolar interaction becomes attractive, and the case in which the polarisation of the dipoles is no longer orthogonal to the lattice, to make the long-range interaction anisotropic. The effect of a harmonic confining potential could help characterise the stability and the importance of finite-size and boundary effects on the ground-states of the system.

For the fractional quantum Hall system, the use of the cylindrical geometry lends itself to implementing Laughlin's thought experiment to compute the Hall conductivity of the system: this could be an additional way to characterise the ground-state properties of the system.

Bibliography

[1] Girvin, S. and Prange, R. (1987) The quantum Hall effect, Graduate texts in contemporary physics, Springer-Verlag, New York.

[2] Zhang, F. and Rice, T. (1988) Effective Hamiltonian for the superconducting Cu oxides. *Physical Review B,* **37**(7), 3759.

[3] Leggett, A. J. (2006) What DO we know about high Tc?. *Nature Physics,* **2**(3), 134.

[4] Nayak, C., Simon, S. H., Stern, A., Freedman, M., and Sarma, S. D. (2008) Non-Abelian anyons and topological quantum computation. *Reviews of Modern Physics,* **80**(3), 1083.

[5] White, S. R. (1992) Density matrix formulation for quantum renormalization groups. *Physical Review Letters,* **69**(19), 2863–2866.

[6] Noack, R. M. and Manmana, S. R. (2005) Diagonalization and Numerical Renormalization-Group-Based Methods for Interacting Quantum Systems. In *AIP Conference Proceedings* AIP Vol. 789, pp. 93–163.

[7] Ceperley, D. M. and Alder, B. (1980) Ground state of the electron gas by a stochastic method. *Physical Review Letters,* **45**(7), 566.

[8] Foulkes, W., Mitas, L., Needs, R., and Rajagopal, G. (2001) Quantum Monte Carlo simulations of solids. *Reviews of Modern Physics,* **73**(1), 33.

[9] Rommer, S. and Östlund, S. (1997) Class of ansatz wave functions for one-dimensional spin systems and their relation to the density matrix renormalization group. *Physical Review B,* **55**(4), 2164.

[10] McCulloch, I. P. (2007) From density-matrix renormalization group to matrix product states. *Journal of Statistical Mechanics: Theory and Experiment,* **2007**(10), P10014.

[11] Schollwöck, U. (2011) The density-matrix renormalization group in the age of matrix product states. *Annals of Physics,* **326**(1), 96–192.

[12] Bloch, I., Dalibard, J., and Zwerger, W. (2008) Many-body physics with ultracold gases. *Reviews of Modern Physics,* **80**(3), 885.

[13] Lewenstein, M., Sanpera, A., and Ahufinger, V. (2012) Ultracold Atoms in Optical Lattices: Simulating quantum many-body systems, Oxford University Press, .

[14] Jaksch, D. and Zoller, P. (2005) The cold atom Hubbard toolbox. *Annals of physics,* **315**(1), 52–79.

[15] Johnson, T. H., Clark, S. R., and Jaksch, D. (2014) What is a quantum simulator?. *EPJ Quantum Technology,* **1**(1).

[16] Bloch, I., Dalibard, J., and Nascimbene, S. (2012) Quantum simulations with ultracold quantum gases. *Nature Physics,* **8**(4), 267.

[17] Georgescu, I. M., Ashhab, S., and Nori, F. (2014) Quantum simulation. *Reviews of Modern Physics,* **86**(1), 153.

[18] Jaksch, D., Bruder, C., Cirac, J. I., Gardiner, C. W., and Zoller, P. (1998) Cold bosonic atoms in optical lattices. *Physical Review Letters,* **81**(15), 3108.

[19] Landau, L. D. (1937) On the theory of phase transitions. *Ukr. J. Phys.,* **11**, 19–32.

[20] v. Klitzing, K., Dorda, G., and Pepper, M. (1980) New Method for High-Accuracy Determination of the Fine-Structure Constant Based on Quantized Hall Resistance. *Physical Review Letters,* **45**(6), 494–497.

[21] Tsui, D. C., Störmer, H. L., and Gossard, A. C. (1982) Zero-resistance state of two-dimensional electrons in a quantizing magnetic field. *Physical Review B,* **25**, 1405–1407.

[22] Wen, X. G. (1990) Topological Orders In Rigid States. *International Journal of Modern Physics B,* **04**(02), 239–271.

[23] Kitaev, A. (2003) Fault-tolerant quantum computation by anyons. *Annals of Physics,* **303**(1), 2–30.

[24] Thouless, D. J., Kohmoto, M., Nightingale, M. P., and den Nijs, M. (1982) Quantized Hall conductance in a two-dimensional periodic potential. *Physical review letters,* **49**(6), 405.

[25] Wen, X.-G. and Niu, Q. (1990) Ground-state degeneracy of the fractional quantum Hall states in the presence of a random potential and on high-genus Riemann surfaces. *Physical Review B,* **41**(13), 9377.

[26] Laughlin, R. B. (1983) Anomalous Quantum Hall Effect: An Incompressible Quantum Fluid with Fractionally Charged Excitations. *Physical Review Letters,* **50**(18), 1395–1398.

[27] Dennis, E., Kitaev, A., Landahl, A., and Preskill, J. (2002) Topological quantum memory. *Journal of Mathematical Physics,* **43**(9), 4452–4505.

[28] Cooper, N. and Wilkin, N. (1999) Composite fermion description of rotating Bose-Einstein condensates. *Physical Review B,* **60**(24), R16279.

[29] Cooper, N. R., Wilkin, N. K., and Gunn, J. (2001) Quantum phases of vortices in rotating Bose-Einstein condensates. *Physical Review Letters,* **87**(12), 120405.

[30] Jaksch, D. and Zoller, P. (2003) Creation of effective magnetic fields in optical lattices: the Hofstadter butterfly for cold neutral atoms. *New Journal of Physics,* **5**, 56–56.

[31] Cooper, N. (2008) Rapidly rotating atomic gases. *Advances in Physics,* **57**(6), 539–616.

[32] Dalibard, J., Gerbier, F., Juzeliūnas, G., and Öhberg, P. (2011) Colloquium: Artificial gauge potentials for neutral atoms. *Reviews of Modern Physics,* **83**(4), 1523.

[33] Aidelsburger, M., Atala, M., Nascimbène, S., Trotzky, S., Chen, Y.-A., and Bloch, I. (2011) Experimental realization of strong effective magnetic fields in an optical lattice. *Physical review letters,* **107**(25), 255301.

[34] Harper, P. G. (1955) Single band motion of conduction electrons in a uniform magnetic field. *Proceedings of the Physical Society. Section A,* **68**(10), 874.

[35] Azbel, M. Y. (1964) Energy spectrum of a conduction electron in a magnetic field. *Sov. Phys. JETP,* **19**(3), 634–645.

[36] Aidelsburger, M., Atala, M., Lohse, M., Barreiro, J. T., Paredes, B., and Bloch, I. (2013) Realization of the Hofstadter Hamiltonian with Ultracold Atoms in Optical Lattices. *Physical Review Letters,* **111**(18).

[37] Miyake, H., Siviloglou, G. A., Kennedy, C. J., Burton, W. C., and Ketterle, W. (2013) Realizing the Harper Hamiltonian with Laser-Assisted Tunneling in Optical Lattices. *Physical Review Letters,* **111**, 185302.

[38] Aidelsburger, M., Lohse, M., Schweizer, C., Atala, M., Barreiro, J. T., Nascimbène, S., Cooper, N. R., Bloch, I., and Goldman, N. (2014) Measuring the Chern number of Hofstadter bands with ultracold bosonic atoms. *Nature Physics,* **11**(2), 162–166.

[39] Tai, M. E., Lukin, A., Rispoli, M., Schittko, R., Menke, T., Borgnia, D., Preiss, P. M., Grusdt, F., Kaufman, A. M., and Greiner, M. (2017) Microscopy of the interacting Harper–Hofstadter model in the two-body limit. *Nature,* **546**(7659), 519–523.

[40] Cooper, N. R. and Dalibard, J. (2013) Reaching Fractional Quantum Hall States with Optical Flux Lattices. *Physical Review Letters,* **110**, 185301.

[41] Sørensen, A. S., Demler, E., and Lukin, M. D. (2005) Fractional Quantum Hall States of Atoms in Optical Lattices. *Physical Review Letters,* **94**(8), 086803.

[42] Hafezi, M., Sørensen, A. S., Demler, E., and Lukin, M. D. (2007) Fractional quantum Hall effect in optical lattices. *Physical Review A,* **76**(2), 023613.

[43] Möller, G. and Cooper, N. R. (2009) Composite Fermion Theory for Bosonic Quantum Hall States on Lattices. *Physical Review Letters,* **103**, 105303.

[44] Sterdyniak, A., Regnault, N., and Möller, G. (2012) Particle entanglement spectra for quantum Hall states on lattices. *Physical Review B,* **86**(16), 165314.

[45] Britton, J. W., Sawyer, B. C., Keith, A. C., Wang, C.-C. J., Freericks, J. K., Uys, H., Biercuk, M. J., and Bollinger, J. J. (2012) Engineered two-dimensional

Ising interactions in a trapped-ion quantum simulator with hundreds of spins. *Nature,* **484**(7395), 489.

[46] Schneider, C., Porras, D., and Schaetz, T. (2012) Experimental quantum simulations of many-body physics with trapped ions. *Reports on Progress in Physics,* **75**(2), 024401.

[47] Saffman, M., Walker, T. G., and Mølmer, K. (2010) Quantum information with Rydberg atoms. *Reviews of Modern Physics,* **82**(3), 2313.

[48] Löw, R., Weimer, H., Nipper, J., Balewski, J. B., Butscher, B., Büchler, H. P., and Pfau, T. (2012) An experimental and theoretical guide to strongly interacting Rydberg gases. *Journal of Physics B: Atomic, Molecular and Optical Physics,* **45**(11), 113001.

[49] Günter, G., Schempp, H., Robert-de Saint-Vincent, M., Gavryusev, V., Helmrich, S., Hofmann, C., Whitlock, S., and Weidemüller, M. (2013) Observing the dynamics of dipole-mediated energy transport by interaction-enhanced imaging. *Science,* **342**(6161), 954–956.

[50] De Paz, A., Sharma, A., Chotia, A., Marechal, E., Huckans, J., Pedri, P., Santos, L., Gorceix, O., Vernac, L., and Laburthe-Tolra, B. (2013) Nonequilibrium quantum magnetism in a dipolar lattice gas. *Physical Review Letters,* **111**(18), 185305.

[51] Lu, M., Burdick, N. Q., Youn, S. H., and Lev, B. L. (2011) Strongly dipolar Bose-Einstein condensate of dysprosium. *Physical Review Letters,* **107**(19), 190401.

[52] Böttcher, F., Schmidt, J.-N., Wenzel, M., Hertkorn, J., Guo, M., Langen, T., and Pfau, T. (2019) Transient supersolid properties in an array of dipolar quantum droplets. *Physical Review X,* **9**(1), 011051.

[53] Tanzi, L., Lucioni, E., Fama, F., Catani, J., Fioretti, A., Gabbanini, C., Bisset, R., Santos, L., and Modugno, G. (2019) Observation of a dipolar quantum gas with metastable supersolid properties. *Physical Review Letters,* **122**(13), 130405.

[54] Chomaz, L., Petter, D., Ilzhöfer, P., Natale, G., Trautmann, A., Politi, C., Durastante, G., van Bijnen, R. M. W., Patscheider, A., Sohmen, M., Mark, M. J., and Ferlaino, F. (2019) Long-Lived and Transient Supersolid Behaviors in Dipolar Quantum Gases. *Physical Review X,* **9**(2), 021012.

[55] Yan, B., Moses, S. A., Gadway, B., Covey, J. P., Hazzard, K. R., Rey, A. M., Jin, D. S., and Ye, J. (2013) Observation of dipolar spin-exchange interactions with lattice-confined polar molecules. *Nature,* **501**(7468), 521.

[56] Hazzard, K. R., Gadway, B., Foss-Feig, M., Yan, B., Moses, S. A., Covey, J. P., Yao, N. Y., Lukin, M. D., Ye, J., Jin, D. S., et al. (2014) Many-body dynamics of dipolar molecules in an optical lattice. *Physical Review Letters,* **113**(19), 195302.

[57] Blackmore, J. A., Caldwell, L., Gregory, P. D., Bridge, E. M., Sawant, R., Aldegunde, J., Mur-Petit, J., Jaksch, D., Hutson, J. M., Sauer, B. E., Tarbutt, M. R., and Cornish, S. L. (2019) Ultracold molecules for quantum simulation: rotational coherences in CaF and RbCs. *Quantum Science and Technology,* **4**(1), 014010.

[58] Capogrosso-Sansone, B., Trefzger, C., Lewenstein, M., Zoller, P., and Pupillo, G. (2010) Quantum phases of cold polar molecules in 2D optical lattices. *Physical Review Letters,* **104**(12), 125301.

[59] Sanpera, A., Kantian, A., Sanchez-Palencia, L., Zakrzewski, J., and Lewenstein, M. (2004) Atomic Fermi-Bose mixtures in inhomogeneous and random lattices:

From Fermi glass to quantum spin glass and quantum percolation. *Physical Review Letters,* **93**(4), 040401.

[60] Glaetzle, A. W., Dalmonte, M., Nath, R., Rousochatzakis, I., Moessner, R., and Zoller, P. (2014) Quantum Spin-Ice and Dimer Models with Rydberg Atoms. *Physical Review X,* **4**, 041037.

[61] Rosson, P., Lubasch, M., Kiffner, M., and Jaksch, D. (2019) Bosonic fractional quantum Hall states on a finite cylinder. *Physical Review A,* **99**(3), 033603.

[62] Rosson, P., Kiffner, M., Mur-Petit, J., and Jaksch, D. (2020) Characterizing the phase diagram of finite-size dipolar Bose-Hubbard systems. *Physical Review A,* **101**(1), 013616.

[63] Hall, E. (1879) On a New Action of the Magnet on Electric Currents.. *American Journal of Mathematics,* **2**(3), 287–292.

[64] Ashcroft, N. W. and Mermin, N. D. (1976) Solid State Physics, Cornell University, Saunders College Publishing, Harcourt Brace Jovanovich College Publishers, .

[65] Lee, P. A. and Ramakrishnan, T. (1985) Disordered electronic systems. *Reviews of Modern Physics,* **57**(2), 287.

[66] Huckestein, B. (1995) Scaling theory of the integer quantum Hall effect. *Reviews of Modern Physics,* **67**(2), 357.

[67] Nobel Prize in Physics 1998, Press Release. https://www.nobelprize.org/prizes/physics/1998/press-release/.

[68] Contreras, S., Knap, W., Skierbiszewski, C., Alause, H., Robert, J., and Khan, M. A. (1997) Observation of quantum Hall effect in 2D-electron gas confined in

GaN/GaAlN heterostructure. *Materials Science and Engineering: B,* **46**(1-3), 92–95.

[69] Tsukazaki, A., Ohtomo, A., Kita, T., Ohno, Y., Ohno, H., and Kawasaki, M. (2007) Quantum Hall effect in polar oxide heterostructures. *Science,* **315**(5817), 1388–1391.

[70] Ferrari, A. C., Meyer, J., Scardaci, V., Casiraghi, C., Lazzeri, M., Mauri, F., Piscanec, S., Jiang, D., Novoselov, K., Roth, S., et al. (2006) Raman spectrum of graphene and graphene layers. *Physical Review Letters,* **97**(18), 187401.

[71] Xu, Y., Miotkowski, I., Liu, C., Tian, J., Nam, H., Alidoust, N., Hu, J., Shih, C.-K., Hasan, M. Z., and Chen, Y. P. (2014) Observation of topological surface state quantum Hall effect in an intrinsic three-dimensional topological insulator. *Nature Physics,* **10**(12), 956.

[72] Zhang, Y., Tan, Y.-W., Stormer, H. L., and Kim, P. (2005) Experimental observation of the quantum Hall effect and Berry's phase in graphene. *Nature,* **438**(7065), 201.

[73] Yoshioka, D. (2013) The quantum Hall effect, Vol. 133, Springer Science & Business Media, .

[74] Landau, L. D. and Lifshitz, E. M. (2013) Quantum mechanics: non-relativistic theory, Vol. 3, Elsevier, .

[75] Laughlin, R. B. (1981) Quantized Hall conductivity in two dimensions. *Physical Review B,* **23**(10), 5632–5633.

[76] Halperin, B. I. (1982) Quantized Hall conductance, current-carrying edge states, and the existence of extended states in a two-dimensional disordered potential. *Physical Review B,* **25**(4), 2185–2190.

[77] Willett, R., Eisenstein, J., Störmer, H., Tsui, D., Gossard, A., and English, J. (1987) Observation of an even-denominator quantum number in the fractional quantum Hall effect. *Physical Review Letters,* **59**(15), 1776.

[78] Fano, G., Ortolani, F., and Colombo, E. (1986) Configuration-interaction calculations on the fractional quantum Hall effect. *Physical Review B,* **34**(4), 2670.

[79] Haldane, F. and Rezayi, E. (1985) Finite-size studies of the incompressible state of the fractionally quantized Hall effect and its excitations. *Physical Review Letters,* **54**(3), 237.

[80] Lam, P. K. and Girvin, S. (1984) Liquid-solid transition and the fractional quantum-Hall effect. *Physical Review B,* **30**(1), 473.

[81] Haldane, F. D. M. (1983) Fractional quantization of the Hall effect: a hierarchy of incompressible quantum fluid states. *Physical Review Letters,* **51**(7), 605.

[82] Trugman, S. and Kivelson, S. (1985) Exact results for the fractional quantum Hall effect with general interactions. *Physical Review B,* **31**(8), 5280.

[83] de Picciotto, R., Reznikov, M., Heiblum, M., Umansky, V., Bunin, G., and Mahalu, D. (1998) Direct observation of a fractional charge. *Physica B: Condensed Matter,* **249-251**, 395–400.

[84] Arovas, D., Schrieffer, J. R., and Wilczek, F. (2002) Fractional statistics and the quantum Hall effect. In *Selected Papers Of J Robert Schrieffer: In Celebration of His 70th Birthday* pp. 270–271 World Scientific.

[85] Leinaas, J. M. and Myrheim, J. (1977) On the theory of identical particles. *Il Nuovo Cimento B (1971-1996),* **37**(1), 1–23.

[86] Laughlin, R. (1984) Primitive and composite ground states in the fractional quantum Hall effect. *Surface Science,* **142**(1-3), 163–172.

[87] Halperin, B. I. (1984) Statistics of quasiparticles and the hierarchy of fractional quantized Hall states. *Physical Review Letters,* **52**(18), 1583.

[88] Jain, J. K. (1989) Composite-fermion approach for the fractional quantum Hall effect. *Physical Review Letters,* **63**(2), 199–202.

[89] Kitaev, A. and Preskill, J. (2006) Topological Entanglement Entropy. *Physical Review Letters,* **96**, 110404.

[90] Bennett, C. H., Brassard, G., Popescu, S., Schumacher, B., Smolin, J. A., and Wootters, W. K. (1996) Purification of noisy entanglement and faithful teleportation via noisy channels. *Physical Review Letters,* **76**(5), 722.

[91] Srednicki, M. (1993) Entropy and area. *Physical Review Letters,* **71**(5), 666.

[92] Eisert, J., Cramer, M., and Plenio, M. B. (2010) Colloquium: Area laws for the entanglement entropy. *Reviews of Modern Physics,* **82**(1), 277–306.

[93] Regnault, N. (2017) Entanglement spectroscopy and its application to the quantum Hall effects. *Topological Aspects of Condensed Matter Physics: Lecture Notes of the Les Houches Summer School: Volume 103, August 2014,* **103**, 165.

[94] Li, H. and Haldane, F. D. M. (2008) Entanglement spectrum as a generalization of entanglement entropy: Identification of topological order in non-Abelian fractional quantum Hall effect states. *Physical Review Letters,* **101**(1), 010504.

[95] Cirac, J. I. and Zoller, P. (2012) Goals and opportunities in quantum simulation. *Nature Physics,* **8**, 264.

[96] Feynman, R. P. (1982) Simulating physics with computers. *International journal of theoretical physics,* **21**(6), 467–488.

[97] Greiner, M., Mandel, O., Esslinger, T., Hänsch, T. W., and Bloch, I. (2002) Quantum phase transition from a superfluid to a Mott insulator in a gas of ultracold atoms. *Nature,* **415**(6867), 39.

[98] Jördens, R., Strohmaier, N., Günter, K., Moritz, H., and Esslinger, T. (2008) A Mott insulator of fermionic atoms in an optical lattice. *Nature,* **455**(7210), 204.

[99] Bakr, W. S., Gillen, J. I., Peng, A., Fölling, S., and Greiner, M. (2009) A quantum gas microscope for detecting single atoms in a Hubbard-regime optical lattice. *Nature,* **462**(7269), 74.

[100] Cheuk, L. W., Nichols, M. A., Okan, M., Gersdorf, T., Ramasesh, V. V., Bakr, W. S., Lompe, T., and Zwierlein, M. W. (2015) Quantum-Gas Microscope for Fermionic Atoms. *Physical Review Letters,* **114**(19), 193001.

[101] Fisher, M. P., Weichman, P. B., Grinstein, G., and Fisher, D. S. (1989) Boson localization and the superfluid-insulator transition. *Physical Review B,* **40**(1), 546.

[102] Wannier, G. H. (1937) The structure of electronic excitation levels in insulating crystals. *Physical Review,* **52**(3), 191.

[103] Kohn, W. (1959) Analytic properties of Bloch waves and Wannier functions. *Physical Review,* **115**(4), 809.

[104] Dalla Torre, E. G., Berg, E., and Altman, E. (2006) Hidden order in 1D Bose insulators. *Physical Review Letters,* **97**(26), 260401.

[105] Sengupta, P., Pryadko, L. P., Alet, F., Troyer, M., and Schmid, G. (2005) Supersolids versus phase separation in two-dimensional lattice bosons. *Physical Review Letters,* **94**(20), 207202.

[106] Maik, M., Hauke, P., Dutta, O., Lewenstein, M., and Zakrzewski, J. (2013) Density-dependent tunneling in the extended Bose–Hubbard model. *New Journal of Physics,* **15**(11), 113041.

[107] Bruder, C., Fazio, R., and Schön, G. (1993) Superconductor–Mott-insulator transition in Bose systems with finite-range interactions. *Physical Review B,* **47**, 342–347.

[108] van Otterlo, A. and Wagenblast, K.-H. (1994) Coexistence of diagonal and off-diagonal long-range order: A Monte Carlo study. *Physical Review Letters,* **72**, 3598–3601.

[109] Batrouni, G. G., Scalettar, R. T., Zimanyi, G. T., and Kampf, A. P. (1995) Supersolids in the Bose-Hubbard Hamiltonian. *Physical Review Letters,* **74**, 2527–2530.

[110] Hubbard, J. (1978) Generalized Wigner lattices in one dimension and some applications to tetracyanoquinodimethane (TCNQ) salts. *Physical Review B,* **17**, 494–505.

[111] Fisher, M. E. and Selke, W. (1980) Infinitely Many Commensurate Phases in a Simple Ising Model. *Physical Review Letters,* **44**, 1502–1505.

[112] Goldman, N., Juzeliūnas, G., Öhberg, P., and Spielman, I. B. (2014) Light-induced gauge fields for ultracold atoms. *Reports on Progress in Physics,* **77**(12), 126401.

[113] Ruseckas, J., Juzeliūnas, G., Öhberg, P., and Fleischhauer, M. (2005) Non-Abelian gauge potentials for ultracold atoms with degenerate dark states. *Physical Review Letters,* **95**(1), 010404.

[114] Hofstadter, D. R. (1976) Energy levels and wave functions of Bloch electrons in rational and irrational magnetic fields. *Physical Review B,* **14**(6), 2239–2249.

[115] Tsui, D. C., Stormer, H. L., and Gossard, A. C. (1982) Two-Dimensional Magnetotransport in the Extreme Quantum Limit. *Physical Review Letters,* **48**(22), 1559–1562.

[116] Harper, F., Simon, S. H., and Roy, R. (2014) Perturbative approach to flat Chern bands in the Hofstadter model. *Physical Review B,* **90**(7), 075104.

[117] Scaffidi, T. and Simon, S. H. (2014) Exact solutions of fractional Chern insulators: Interacting particles in the Hofstadter model at finite size. *Physical Review B,* **90**, 115132.

[118] Palmer, R. N. and Jaksch, D. (2006) High-Field Fractional Quantum Hall Effect in Optical Lattices. *Physical Review Letters,* **96**(18).

[119] Palmer, R. N., Klein, A., and Jaksch, D. (2008) Optical lattice quantum Hall effect. *Physical Review A,* **78**(1).

[120] Möller, G. and Cooper, N. R. (2015) Fractional Chern insulators in Harper-Hofstadter bands with higher Chern number. *Physical review letters,* **115**(12), 126401.

[121] Bauer, D., Jackson, T., and Roy, R. (2016) Quantum geometry and stability of the fractional quantum Hall effect in the Hofstadter model. *Physical Review B,* **93**(23), 235133.

[122] Andrews, B. and Möller, G. (2018) Stability of fractional Chern insulators in the effective continuum limit of Harper-Hofstadter bands with Chern number$|C|> 1$. *Physical Review B,* **97**(3), 035159.

[123] Gerster, M., Rizzi, M., Silvi, P., Dalmonte, M., and Montangero, S. (2017) Fractional quantum Hall effect in the interacting Hofstadter model via tensor networks. *Physical Review B,* **96**(19), 195123.

[124] He, Y.-C., Grusdt, F., Kaufman, A., Greiner, M., and Vishwanath, A. (2017) Realizing and adiabatically preparing bosonic integer and fractional quantum Hall states in optical lattices. *Physical Review B,* **96**(20), 201103.

[125] Račiūnas, M., Ünal, F. N., Anisimovas, E., and Eckardt, A. (2018) Creating, probing, and manipulating fractionally charged excitations of fractional Chern insulators in optical lattices. *Physical Review A,* **98**(6), 063621.

[126] Budich, J. C., Elben, A., Łacki, M., Sterdyniak, A., Baranov, M. A., and Zoller, P. (2017) Coupled atomic wires in a synthetic magnetic field. *Physical Review A,* **95**, 043632.

[127] Strinati, M. C., Cornfeld, E., Rossini, D., Barbarino, S., Dalmonte, M., Fazio, R., Sela, E., and Mazza, L. (2017) Laughlin-like States in Bosonic and Fermionic Atomic Synthetic Ladders. *Physical Review X,* **7**(2), 021033.

[128] Petrescu, A., Piraud, M., Roux, G., McCulloch, I. P., and Le Hur, K. (2017) Precursor of the Laughlin state of hard-core bosons on a two-leg ladder. *Physical Review B,* **96**, 014524.

[129] Natu, S. S., Mueller, E. J., and Sarma, S. D. (2016) Competing ground states of strongly correlated bosons in the Harper-Hofstadter-Mott model. *Physical Review A,* **93**(6).

[130] Hügel, D., Strand, H. U. R., Werner, P., and Pollet, L. (2017) Anisotropic Harper-Hofstadter-Mott model: Competition between condensation and magnetic fields. *Physical Review B,* **96**(5).

[131] Zaletel, M. P., Mong, R. S., and Pollmann, F. (2013) Topological characterization of fractional quantum hall ground states from microscopic hamiltonians. *Physical review letters,* **110**(23), 236801.

[132] Zaletel, M. P., Mong, R. S., and Pollmann, F. (2014) Flux insertion, entanglement, and quantized responses. *Journal of Statistical Mechanics: Theory and Experiment,* **2014**(10), P10007.

[133] Grushin, A. G., Motruk, J., Zaletel, M. P., and Pollmann, F. (2015) Characterization and stability of a fermionic $\nu = 1/3$ fractional Chern insulator. *Physical Review B,* **91**(3), 035136.

[134] He, Y.-C., Bhattacharjee, S., Moessner, R., and Pollmann, F. (2015) Bosonic integer quantum hall effect in an interacting lattice model. *Physical review letters,* **115**(11), 116803.

[135] Motruk, J., Zaletel, M. P., Mong, R. S., and Pollmann, F. (2016) Density matrix renormalization group on a cylinder in mixed real and momentum space. *Physical Review B,* **93**(15), 155139.

[136] Motruk, J. and Pollmann, F. (2017) Phase transitions and adiabatic preparation of a fractional Chern insulator in a boson cold-atom model. *Physical Review B,* **96**(16), 165107.

[137] Dong, X.-Y., Grushin, A. G., Motruk, J., and Pollmann, F. (2018) Charge excitation dynamics in bosonic fractional Chern insulators. *Physical review letters,* **121**(8), 086401.

[138] Schoonderwoerd, L., Pollmann, F., and Möller, G. (2019) Interaction-driven plateau transition between integer and fractional Chern Insulators. *arXiv preprint arXiv:1908.00988,*.

[139] Hastings, M. B. (2007) An area law for one-dimensional quantum systems. *Journal of Statistical Mechanics: Theory and Experiment,* **2007**(08), P08024–P08024.

[140] Verstraete, F., Cirac, J. I., Latorre, J. I., Rico, E., and Wolf, M. M. (2005) Renormalization-group transformations on quantum states. *Physical Review Letters,* **94**(14), 140601.

[141] Vidal, G. (2003) Efficient classical simulation of slightly entangled quantum computations. *Physical Review Letters,* **91**(14), 147902.

[142] Perez-Garcia, D., Verstraete, F., Wolf, M. M., and Cirac, J. I. (2006) Matrix product state representations. *arXiv preprint quant-ph/0608197,*.

[143] Ekert, A. and Knight, P. L. (1995) Entangled quantum systems and the Schmidt decomposition. *American Journal of Physics,* **63**(5), 415–423.

[144] Verstraete, F. and Cirac, J. I. (2006) Matrix product states represent ground states faithfully. *Physical Review B,* **73**(9), 094423.

[145] Al-Assam, S., Clark, S. R., and Jaksch, D. (2017) The tensor network theory library. *Journal of Statistical Mechanics: Theory and Experiment,* **2017**(9), 093102.

[146] Nishino, T., Hieida, Y., Okunishi, K., Maeshima, N., Akutsu, Y., and Gendiar, A. (2001) Two-dimensional tensor product variational formulation. *Progress of theoretical physics,* **105**(3), 409–417.

[147] Verstraete, F., Porras, D., and Cirac, J. I. (2004) Density matrix renormalization group and periodic boundary conditions: A quantum information perspective. *Physical Review Letters,* **93**(22), 227205.

[148] Sandvik, A. W. (2007) Evidence for Deconfined Quantum Criticality in a Two-Dimensional Heisenberg Model with Four-Spin Interactions. *Physical Review Letters,* **98**, 227202.

[149] Isakov, S. V., Hastings, M. B., and Melko, R. G. (2011) Topological entanglement entropy of a Bose–Hubbard spin liquid. *Nature Physics,* **7**(10), 772.

[150] White, S. R., Scalapino, D. J., Sugar, R. L., Loh, E., Gubernatis, J. E., and Scalettar, R. T. (1989) Numerical study of the two-dimensional Hubbard model. *Physical Review B,* **40**(1), 506.

[151] Troyer, M. and Wiese, U.-J. (2005) Computational complexity and fundamental limitations to fermionic quantum Monte Carlo simulations. *Physical Review Letters,* **94**(17), 170201.

[152] Liang, S. and Pang, H. (1994) Approximate diagonalization using the density matrix renormalization-group method: A two-dimensional-systems perspective. *Physical Review B,* **49**, 9214–9217.

[153] Cirac, J. I. and Verstraete, F. (2009) Renormalization and tensor product states in spin chains and lattices. *Journal of Physics A: Mathematical and Theoretical,* **42**(50), 504004.

[154] Evenbly, G. and Vidal, G. (2013) Quantum criticality with the multi-scale entanglement renormalization ansatz. In *Strongly correlated systems* pp. 99–130 Springer.

[155] Evenbly, G. and Vidal, G. (2011) Tensor network states and geometry. *Journal of Statistical Physics,* **145**(4), 891–918.

[156] Pfeifer, R. N., Evenbly, G., and Vidal, G. (2009) Entanglement renormalization, scale invariance, and quantum criticality. *Physical Review A,* **79**(4), 040301.

[157] Evenbly, G. and Vidal, G. (2009) Entanglement renormalization in two spatial dimensions. *Physical Review Letters,* **102**(18), 180406.

[158] Orús, R. (2019) Tensor networks for complex quantum systems. *Nature Reviews Physics,* **1**(9), 538–550.

[159] Verstraete, F., Murg, V., and Cirac, J. I. (2008) Matrix product states, projected entangled pair states, and variational renormalization group methods for quantum spin systems. *Advances in Physics,* **57**(2), 143–224.

[160] Jordan, J., Orús, R., Vidal, G., Verstraete, F., and Cirac, J. I. (2008) Classical simulation of infinite-size quantum lattice systems in two spatial dimensions. *Physical Review Letters,* **101**(25), 250602.

[161] Vidal, G. (2007) Entanglement renormalization. *Physical Review Letters,* **99**(22), 220405.

[162] Evenbly, G. and Vidal, G. (2009) Algorithms for entanglement renormalization. *Physical Review B,* **79**(14), 144108.

[163] Stoudenmire, E. and White, S. R. (2012) Studying Two-Dimensional Systems with the Density Matrix Renormalization Group. *Annual Review of Condensed Matter Physics,* **3**(1), 111–128.

[164] Crosswhite, G. M. and Bacon, D. (2008) Finite automata for caching in matrix product algorithms. *Physical Review A,* **78**, 012356.

[165] Jordan, P. and Wigner, E. P. (1993) Über das paulische äquivalenzverbot. In *The Collected Works of Eugene Paul Wigner* pp. 109–129 Springer.

[166] Łacki, M., Pichler, H., Sterdyniak, A., Lyras, A., Lembessis, V. E., Al-Dossary, O., Budich, J. C., and Zoller, P. (2016) Quantum Hall physics with cold atoms in cylindrical optical lattices. *Physical Review A,* **93**, 013604.

[167] Ciftja, O., Ockleberry, N., and Okolo, C. (2011) One-particle Density Of Laughlin States At Finite N. *Modern Physics Letters B,* **25**(25), 1983–1992.

[168] Rezayi, E. H. and Haldane, F. D. M. (1994) Laughlin state on stretched and squeezed cylinders and edge excitations in the quantum Hall effect. *Physical Review B,* **50**(23), 17199–17207.

[169] Wen, X.-G. (1992) Theory Of The Edge States In Fractional Quantum Hall Effects. *International Journal of Modern Physics B,* **06**(10), 1711–1762.

[170] Fendley, P., Fisher, M. P. A., and Nayak, C. (2007) Topological Entanglement Entropy from the Holographic Partition Function. *Journal of Statistical Physics,* **126**(6), 1111–1144.

[171] Dong, S., Fradkin, E., Leigh, R. G., and Nowling, S. (2008) Topological entanglement entropy in Chern-Simons theories and quantum Hall fluids. *Journal of High Energy Physics,* **2008**(05), 016–016.

[172] Vidal, G., Latorre, J. I., Rico, E., and Kitaev, A. (2003) Entanglement in Quantum Critical Phenomena. *Physical Review Letters,* **90**, 227902.

[173] Zhang, Y., Grover, T., Turner, A., Oshikawa, M., and Vishwanath, A. (2012) Quasiparticle statistics and braiding from ground-state entanglement. *Physical Review B,* **85**(23), 235151.

[174] Jiang, H.-C., Wang, Z., and Balents, L. (2012) Identifying topological order by entanglement entropy. *Nature Physics,* **8**(12), 902.

[175] Kol, A. and Read, N. (1993) Fractional quantum Hall effect in a periodic potential. *Physical Review B,* **48**(12), 8890–8898.

[176] Ospelkaus, S., Pe'Er, A., Ni, K.-K., Zirbel, J., Neyenhuis, B., Kotochigova, S., Julienne, P., Ye, J., and Jin, D. (2008) Efficient state transfer in an ultracold dense gas of heteronuclear molecules. *Nature Physics,* **4**(8), 622.

[177] Zirbel, J., Ni, K.-K., Ospelkaus, S., Nicholson, T., Olsen, M., Julienne, P., Wieman, C., Ye, J., and Jin, D. (2008) Heteronuclear molecules in an optical dipole trap. *Physical Review A,* **78**(1), 013416.

[178] Chotia, A., Neyenhuis, B., Moses, S. A., Yan, B., Covey, J. P., Foss-Feig, M., Rey, A. M., Jin, D. S., and Ye, J. (2012) Long-lived dipolar molecules and Feshbach molecules in a 3D optical lattice. *Physical Review Letters,* **108**(8), 080405.

[179] Moses, S. A., Covey, J. P., Miecnikowski, M. T., Yan, B., Gadway, B., Ye, J., and Jin, D. S. (2015) Creation of a low-entropy quantum gas of polar molecules in an optical lattice. *Science,* **350**(6261), 659–662.

[180] Potter, A. C., Berg, E., Wang, D.-W., Halperin, B. I., and Demler, E. (2010) Superfluidity and dimerization in a multilayered system of fermionic polar molecules. *Physical Review Letters,* **105**(22), 220406.

[181] Gorshkov, A. V., Manmana, S. R., Chen, G., Ye, J., Demler, E., Lukin, M. D., and Rey, A. M. (2011) Tunable superfluidity and quantum magnetism with ultracold polar molecules. *Physical Review Letters,* **107**(11), 115301.

[182] Zhang, C., Safavi-Naini, A., Rey, A. M., and Capogrosso-Sansone, B. (2015) Equilibrium phases of tilted dipolar lattice bosons. *New Journal of Physics,* **17**(12), 123014.

[183] Micheli, A., Brennen, G., and Zoller, P. (2006) A toolbox for lattice-spin models with polar molecules. *Nature Physics,* **2**(5), 341.

[184] Gong, Z.-X., Maghrebi, M. F., Hu, A., Wall, M. L., Foss-Feig, M., and Gorshkov, A. V. (2016) Topological phases with long-range interactions. *Physical Review B,* **93**(4), 041102.

[185] Yao, N. Y., Gorshkov, A. V., Laumann, C. R., Läuchli, A. M., Ye, J., and Lukin, M. D. (2013) Realizing fractional Chern insulators in dipolar spin systems. *Physical Review Letters,* **110**(18), 185302.

[186] Yao, N. Y., Laumann, C. R., Gorshkov, A. V., Bennett, S. D., Demler, E., Zoller, P., and Lukin, M. D. (2012) Topological flat bands from dipolar spin systems. *Physical Review Letters,* **109**(26), 266804.

[187] Sanner, C., Su, E. J., Keshet, A., Gommers, R., Shin, Y.-i., Huang, W., and Ketterle, W. (2010) Suppression of density fluctuations in a quantum degenerate Fermi gas. *Physical Review Letters,* **105**(4), 040402.

[188] Drewes, J., Cocchi, E., Miller, L., Chan, C., Pertot, D., Brennecke, F., and Köhl, M. (2016) Thermodynamics versus local density fluctuations in the metal–Mott-insulator crossover. *Physical Review Letters,* **117**(13), 135301.

[189] Büchler, H. P., Demler, E., Lukin, M., Micheli, A., Prokof'Ev, N., Pupillo, G., and Zoller, P. (2007) Strongly correlated 2D quantum phases with cold polar molecules: controlling the shape of the interaction potential. *Physical Review Letters,* **98**(6), 060404.

[190] Micheli, A., Pupillo, G., Büchler, H., and Zoller, P. (2007) Cold polar molecules in two-dimensional traps: Tailoring interactions with external fields for novel quantum phases. *Physical Review A,* **76**(4), 043604.

[191] Büchler, H., Micheli, A., and Zoller, P. (2007) Three-body interactions with cold polar molecules. *Nature Physics,* **3**(10), 726.

[192] Ni, K.-K., Ospelkaus, S., Wang, D., Quéméner, G., Neyenhuis, B., De Miranda, M., Bohn, J., Ye, J., and Jin, D. (2010) Dipolar collisions of polar molecules in the quantum regime. *Nature,* **464**(7293), 1324.

[193] Moses, S. A., Covey, J. P., Miecnikowski, M. T., Jin, D. S., and Ye, J. (2017) New frontiers for quantum gases of polar molecules. *Nature Physics,* **13**(1), 13.

[194] Mayle, M., Quéméner, G., Ruzic, B. P., and Bohn, J. L. (2013) Scattering of ultracold molecules in the highly resonant regime. *Physical Review A,* **87**(1), 012709.

[195] Gregory, P. D., Frye, M. D., Blackmore, J. A., Bridge, E. M., Sawant, R., Hutson, J. M., and Cornish, S. L. (2019) Sticky collisions of ultracold RbCs molecules. *Nature Communications,* **10**(1), 3104.

[196] Dutta, O., Gajda, M., Hauke, P., Lewenstein, M., Lühmann, D.-S., Malomed, B. A., Sowiński, T., and Zakrzewski, J. (2015) Non-standard Hubbard models in optical lattices: a review. *Reports on Progress in Physics,* **78**(6), 066001.

[197] Ohgoe, T., Suzuki, T., and Kawashima, N. (2012) Quantum phases of hard-core bosons on two-dimensional lattices with anisotropic dipole-dipole interaction. *Physical Review A,* **86**(6), 063635.

[198] Landig, R., Hruby, L., Dogra, N., Landini, M., Mottl, R., Donner, T., and Esslinger, T. (2016) Quantum phases from competing short-and long-range interactions in an optical lattice. *Nature,* **532**(7600), 476.

[199] Schreiber, M., Hodgman, S. S., Bordia, P., Lüschen, H. P., Fischer, M. H., Vosk, R., Altman, E., Schneider, U., and Bloch, I. (2015) Observation of many-body localization of interacting fermions in a quasirandom optical lattice. *Science,* **349**(6250), 842–845.

[200] Ohgoe, T., Suzuki, T., and Kawashima, N. (2012) Ground-state phase diagram of the two-dimensional extended Bose-Hubbard model. *Physical Review B,* **86**(5), 054520.

[201] Pethick, C. J. and Smith, H. (2008) Bose-Einstein condensation in dilute gases, Cambridge University Press, Cambridge, UK.

[202] Pitaevskii, L. P. and Stringari, S. (2016) Bose-Einstein condensation and superfluidity, Oxford University Press, Oxford, UK.

[203] Penrose, O. and Onsager, L. (1956) Bose-Einstein condensation and liquid Helium. *Physical Review,* **104**(3), 576–584.

[204] Yang, C. N. (1962) Concept of Off-Diagonal Long-Range Order and the Quantum Phases of Liquid He and of Superconductors. *Reviews of Modern Physics,* **34**(4), 694–704.

[205] Mahan, G. D. (2000) Many-particle physics, Physics of solids and liquidsKluwer Academic, New York 3rd edition.

[206] Holzmann, M. and Baym, G. (2007) Condensate superfluidity and infrared structure of the single-particle Green's function: the Josephson relation. *Physical Review B,* **76**(9), 092502.

[207] Holzmann, M., Baym, G., Blaizot, J.-P., and Laloe, F. (2007) Superfluid transition of homogeneous and trapped two-dimensional Bose gases. *Proceedings of the National Academy of Sciences,* **104**(5), 1476–1481.

[208] Desbuquois, R., Chomaz, L., Yefsah, T., Léonard, J., Beugnon, J., Weitenberg, C., and Dalibard, J. (2012) Superfluid behaviour of a two-dimensional Bose gas. *Nature Physics,* **8**(9), 645–648.

[209] Löwdin, P.-O. (1955) Quantum theory of many-particle systems. Physical interpretations by means of density matrices, natural spin-orbitals, and convergence problems in the method of configurational interaction. *Physical Review,* **97**(6), 1474.

[210] Jiménez-García, K., Compton, R., Lin, Y.-J., Phillips, W., Porto, J., and Spielman, I. (2010) Phases of a two-dimensional Bose gas in an optical lattice. *Physical Review Letters,* **105**(11), 110401.

[211] Amico, L., Fazio, R., Osterloh, A., and Vedral, V. (2008) Entanglement in many-body systems. *Reviews of Modern Physics,* **80**(2), 517.

[212] Walsh, C., Sémon, P., Poulin, D., Sordi, G., and Tremblay, A.-M. (2019) Local entanglement entropy and mutual information across the Mott transition in the two-dimensional Hubbard model. *Physical Review Letters,* **122**(6), 067203.

[213] Frérot, I. and Roscilde, T. (2016) Entanglement entropy across the superfluid-insulator transition: A signature of bosonic criticality. *Physical Review Letters,* **116**(19), 190401.

[214] Islam, R., Ma, R., Preiss, P. M., Tai, M. E., Lukin, A., Rispoli, M., and Greiner, M. (2015) Measuring entanglement entropy in a quantum many-body system. *Nature,* **528**(7580), 77.

[215] Kaufman, A. M., Tai, M. E., Lukin, A., Rispoli, M., Schittko, R., Preiss, P. M., and Greiner, M. (2016) Quantum thermalization through entanglement in an isolated many-body system. *Science,* **353**(6301), 794–800.

[216] Zhang, C., Safavi-Naini, A., and Capogrosso-Sansone, B. (2018) Equilibrium phases of dipolar lattice bosons in the presence of random diagonal disorder. *Physical Review A,* **97**, 013615.

[217] Bombin, R., Boronat, J., and Mazzanti, F. (2017) Dipolar Bose supersolid stripes. *Physical Review Letters,* **119**(25), 250402.

[218] Boninsegni, M. and Prokof'ev, N. V. (2012) Colloquium: supersolids: what and where are they?. *Reviews of Modern Physics,* **84**(2), 759–776.

[219] Andreev, A. and Lifshits, I. (1969) Quantum theory of defects in crystals. *Zhur Eksper Teoret Fiziki,* **56**(6), 2057–2068.

[220] Chester, G. (1970) Speculations on Bose-Einstein condensation and quantum crystals. *Physical Review A,* **2**(1), 256.

[221] Kim, E. and Chan, M. (2004) Observation of superflow in solid Helium. *Science,* **305**(5692), 1941–1944.

[222] Kim, E. and Chan, M. (2004) Probable observation of a supersolid Helium phase. *Nature,* **427**(6971), 225.

[223] Prokof'ev, N. and Svistunov, B. (2005) Supersolid state of matter. *Physical Review Letters,* **94**(15), 155302.

[224] Boninsegni, M., Kuklov, A., Pollet, L., Prokof'ev, N., Svistunov, B., and Troyer, M. (2006) Fate of Vacancy-Induced Supersolidity in He 4. *Physical Review Letters,* **97**(8), 080401.

[225] Rittner, A. S. C. and Reppy, J. D. (2006) Observation of Classical Rotational Inertia and Nonclassical Supersolid Signals in Solid He 4 below 250 mK. *Physical Review Letters,* **97**(16), 165301.

[226] Ohgoe, T., Suzuki, T., and Kawashima, N. (2011) Novel mechanism of supersolid of ultracold polar molecules in optical lattices. *Journal of the Physical Society of Japan,* **80**(11), 113001.

[227] Dang, L., Boninsegni, M., and Pollet, L. (2008) Vacancy supersolid of hard-core bosons on the square lattice. *Physical Review B,* **78**(13), 132512.

[228] Batrouni, G., Hébert, F., and Scalettar, R. (2006) Supersolid phases in the one-dimensional extended soft-core bosonic Hubbard model. *Physical Review Letters,* **97**(8), 087209.

[229] Yamamoto, D., Masaki, A., and Danshita, I. (2012) Quantum phases of hard-core bosons with long-range interactions on a square lattice. *Physical Review B,* **86**(5), 054516.

[230] Sherson, J. F., Weitenberg, C., Endres, M., Cheneau, M., Bloch, I., and Kuhr, S. (2010) Single-atom-resolved fluorescence imaging of an atomic Mott insulator. *Nature,* **467**(7311), 68.

[231] Dunjko, V. and Briegel, H. J. (2018) Machine learning & artificial intelligence in the quantum domain: a review of recent progress. *Reports on Progress in Physics,* **81**(7), 074001.

[232] Wang, L. (2016) Discovering phase transitions with unsupervised learning. *Physical Review B,* **94**(19), 195105.

[233] Hu, W., Singh, R. R., and Scalettar, R. T. (2017) Discovering phases, phase transitions, and crossovers through unsupervised machine learning: A critical examination. *Physical Review E,* **95**(6), 062122.

[234] Liu, J., Qi, Y., Meng, Z. Y., and Fu, L. (2017) Self-learning Monte Carlo method. *Physical Review B,* **95**(4), 041101.

[235] Broecker, P., Carrasquilla, J., Melko, R. G., and Trebst, S. (2017) Machine learning quantum phases of matter beyond the fermion sign problem. *Scientific reports,* **7**(1), 8823.

[236] Van Nieuwenburg, E. P., Liu, Y.-H., and Huber, S. D. (2017) Learning phase transitions by confusion. *Nature Physics,* **13**(5), 435.

[237] Ch'Ng, K., Carrasquilla, J., Melko, R. G., and Khatami, E. (2017) Machine learning phases of strongly correlated fermions. *Physical Review X,* **7**(3), 031038.

[238] Wetzel, S. J. (2017) Unsupervised learning of phase transitions: From principal component analysis to variational autoencoders. *Physical Review E,* **96**(2), 022140.

[239] Jolliffe, I. T. (2002) Principal Component Analysis, Springer Series in StatisticsSpringer, 2nd edition.

[240] Endres, M., Cheneau, M., Fukuhara, T., Weitenberg, C., Schauß, P., Gross, C., Mazza, L., Bañuls, M. C., Pollet, L., Bloch, I., et al. (2013) Single-site-and single-atom-resolved measurement of correlation functions. *Applied Physics B,* **113**(1), 27–39.

[241] Cinti, F. and Boninsegni, M. (2019) Absence of superfluidity in 2D Dipolar Bose Striped Crystals. *Journal of Low Temperature Physics,* **196**(5-6), 413–422.

[242] Natale, G., van Bijnen, R., Patscheider, A., Petter, D., Mark, M., Chomaz, L., and Ferlaino, F. (2019) Excitation spectrum of a trapped dipolar supersolid and its experimental evidence. *Physical Review Letters,* **123**(5), 050402.